Computational Study of Actin Morphology and Rheology

by

Taeyoon Kim

Master of Science in Mechanical Engineering
Massachusetts Institute of Technology, 2007

Submitted to the Department of Mechanical Engineering
in partial fulfillment of the requirements for the degree of

Doctor of Philosophy in Mechanical Engineering

at the

Massachusetts Institute of Technology

February 2011

Signature of Author _____

Department of Mechanical Engineering
Oct 31, 2010

Certified by _____

Roger, D. Kamm
Professor of Mechanical and Biological Engineering
Thesis Supervisor

Accepted by _____

David E. Hardt
Professor of Mechanical Engineering
Chairman, Department Committee on Graduate Students

Computational Study of Actin Morphology and Rheology

by

Taeyoon Kim

Submitted to the Department of Mechanical Engineering on Oct 31, 2010,
in partial fulfillment of the requirements for the degree of
Doctor of Philosophy in Mechanical Engineering

Abstract

The cytoskeletal network consisting mainly of actin and actin binding proteins is highly dynamic, provides structural integrity to cells, and plays a central role in a wide range of mechanical and biological functions such as migration and the sensation of external forces. Thus, knowledge of actin cytoskeleton is indispensable for understanding the mechanics and many biological processes of cells. Although various theoretical, computational, and experimental investigations have been conducted, the underlying bases for these critical mechanical properties are still poorly understood. This thesis examines the morphology and rheology of actin networks through the development of a 3-D computational model.

First, the viscoelastic properties of actin networks irreversibly bound by actin crosslinking proteins (ACPs) were investigated. Relative contributions of the concentration and type of ACPs, the stiffnesses of actin filaments and ACPs, and thermal fluctuations were evaluated at various prestrain levels. These studies demonstrated for the first time that under typical biological conditions, extensional stiffnesses of both actin filaments and ACPs were surprisingly significant, but thermal fluctuations were relatively unimportant. At high tensions, only a small portion of networks supported a majority of the load.

Second, the relative importance of two mechanisms of ACPs which control dynamic properties of actin networks, unbinding and subdomain unfolding, was evaluated. By analyzing the strain-stiffening, stress relaxation, and plastic deformation of the networks

with unbinding and/or unfolding, it was found that despite the possibility of unfolding, ACP unbinding is the dominant mechanism governing actin rheology under typical experimental and physiological conditions. In addition, detailed processes by which unbinding plays such a role were investigated.

Lastly, roles that molecular motors play in the morphology and rheology of actin networks were studied. Motors enhanced elasticity of actin networks and led to heterogeneous networks to a degree that was highly dependent on how easily the motors unbind from actin filaments. ACPs helped the motors to make networks elastic and prevented the networks from being heterogeneous. Also, morphology of actin-motor networks was significantly affected by boundary conditions.

Thesis Supervisor: Roger D. Kamm
Title: Professor of Mechanical and Biological Engineering

Acknowledgments

This work would not have been possible without contributions of numerous people. First, I would like to thank my advisor, Prof. Roger D. Kamm, who has been a great mentor as well as a friend. For the past 5 years, he has supported my research and inspired me with his excellent intuition. I also thank my thesis committee members, Prof. Mary C. Boyce and Prof. Gareth H. McKinley, who gave me valuable advices on my thesis research.

I would like to acknowledge Prof. Wonmuk Hwang for countless advices and helps for developing my computational model and pursuing my research. I would also like to express my gratitude to Dr. Hyungsuk Lee who was my colleague in Prof. Kamm's lab. I could learn a wide variety of knowledge about my research topic from him, and he helped to validate my computational model by performing an experiment. In addition, I am very grateful to Dr. Jeenu Kim and Dr. Seung Eun Lee who were also my former colleagues. I learned diverse computational techniques required for my research. I would also like to thank Dr. Nathan Hammond and Philip Bransford. They were always open for discussion about my research.

I thank all the past and current lab members for their friendship and supports through 5 years: Cherry Wan, Tharathorn Rimchala, Vernella Vickerman, Ted Feldman, Anusuya Das, Ioannis Zervantonakis, William Polacheck, Kwang-Ho Lee, Aida Rahim, Peter Mack, Peyman Honarmandi, Ryo Sudo, Sid Chung, Young Kum Park, Helene Karcher, Aida Rahim, Jeff Hsu, Ho Seok Park, Chandrasekhar Kothapalli, and all of the

Kamm Lab members.

Most of my happiest time at MIT was spent with friends I met there. I thank Jooeun Ahn, Hyun Jin In, Chung Jong Yu, Jaewon Cha, Yanghyo Kim, Yongkeun Park, Sung Joo Bae, Minseung Ahn, Yongjin Sung, Yongdae Shin, Won-Yong Lee, Jongho Lee, Kimin Jun, and all members in Korean Graduate Student Association Basketball Club and Korean Graduate Student Association of Mechanical Engineering for the friendship.

I would never have completed this Ph.D. course if there had not been love and support of my family. My parents, Bo Chin Kim and Jung Ja Kim, have never stopped supporting me and have always believed in my potential and ability. I could be what I am now via their endless love. Also, I would like to deeply thank my wife, Sunyoung Park, for her unconditional love.

Contents

List of Figures

List of Tables

Chapter 1

Introduction

Components of living organisms can be classified into organs, tissues, cells, and intra-cellular constituents in order of large to small length scale. Cells are fundamental functional constituents and play a significant role in multi-cellular organisms; they facilitate reproduction, growth, and various chemical reactions [1]. Cells also exhibit a number of interesting dynamic behaviors in response to external stimuli. Subjected to rapid deformation, cells tend to develop high levels of stress, whereas they easily deform under low strain rates with relatively little stress [2]. At fixed shear strain or stretch, marked stress relaxation has been observed both *in vivo* [2,3] and *in vitro* [4]. For most eukaryotic cells, these behaviors are attributable to the cytoskeleton, a highly dynamic structure mainly composed of three major constituents with distinct mechanical characteristics [5]:

Figure 1.1 Three primary constituent filaments of the cytoskeleton: intermediate filaments, microtubules, and microfilaments (F-actin). They are distinctly distributed and play various roles in cells. (Adapted from [1].)

intermediate filaments, microtubules, and microfilaments (F-actin) (Figure 1.1). Actin is the most abundant intra-cellular protein in eukaryotic cells; typical concentrations of actin in the cytosol of nonmuscle cells range from 0.1 to 0.5 mM, but in some cellular structures, local concentrations can attain values as high as 5 mM [1]. It is widely believed that actin plays an important role in a wide range of biological and mechanical phenomena including structural stability, migration, and intra-cellular processes [1].

1.1. G-actin, F-actin, and Polymerization

G-actin (monomeric actin) is a protein with molecular weight of 42 kDa whose dimension is about 5.5×5.5×3.5 nm [6] (Figure 1.2a). In various cells, G-actin is encoded by a relatively well-conserved gene family [1]. G-actin self-assembles into F-actin,

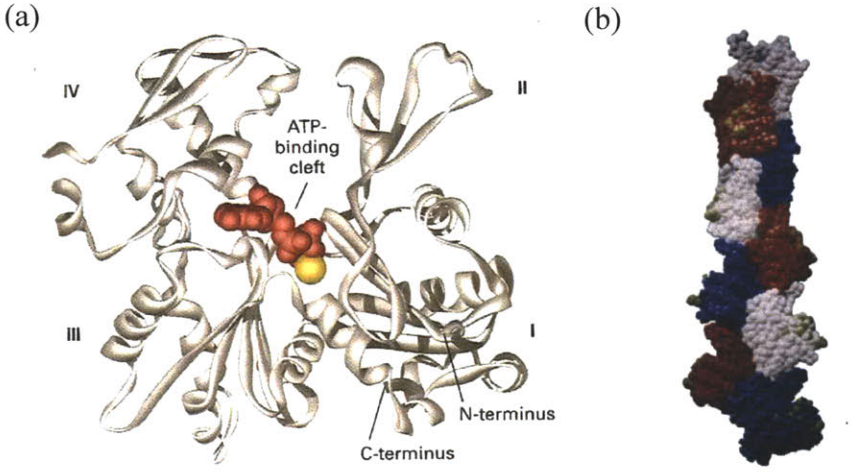

Figure 1.2 Atomic structures of G-actin and F-actin. (a) β-actin monomer contains a plate-like molecule divided by a central cleft. (Adapted from [1,6].) Each G-actin has molecular weight of 42 kDa. (b) F-actin consists of a tight double-stranded helix whose pitch is approximately 74 nm. (Adapted from [7].)

a double helical filament with 7-9 nm in diameter and up to several microns in length [1] (Figure 1.2b). F-actin is considered a semi-flexible polymer due to relatively large persistence length, ~10 μm [8,9]. Actin polymerization is governed mainly by a nucleation-elongation process [10]. Three G-actins form a stable nucleus at low probability [10,11], followed by quick elongation at both ends at significantly distinct rates: fast at barbed (plus) ends and slow at pointed (minus) ends. G-actin also depolymerizes at both ends at analogous rates. Thus, the dynamic behavior of F-actin occurs by elongation via assembly primarily at the barbed end and by shrinkage via disassembly primarily at the pointed end, in a polarized manner [12]. At a specific G-actin concentration, the elongation rate at the barbed end is balanced by shortening rate at the pointed end, resulting in the net unidirectional movement of actin filaments called "treadmilling" [13].

1.2. Organization of Filaments via Actin Crosslinking Proteins (ACP)

Actin filaments are organized into orthogonal networks or bundles that are coupled to membrane proteins [5]. The organization of filaments is mediated by actin crosslinking proteins (ACPs) such as α-actinin, fimbrin, fascin, and filamin [1,14]. Wide variations in their function and structure in different organisms [15] indicate that ACPs, together with actin, evolved to satisfy various mechanical needs of cells (Table 1.1). Structural arrangement of actin binding sites in ACPs is a main factor determining the organization of actin filaments [1]. If the binding sites are aligned in tandem, as is true for fimbrin and fascin, ACPs tend to pack actin filaments into stress fibers as are prevalent in the extension and adhesion of cells. On the contrary, ACPs, such as filamin, have relatively long,

Name	Molecular weight	Organization of binding sites	Locations
Fimbrin	68,000		Microvilli, stereocilia, adhesion plaques, yeast actin cables
α-actinin	102,000	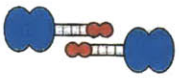	Filopodia, lamellipodia, stress fibers, adhesion plaques
Spectrin	**α: 280,000** **β: 246,000-275,000**	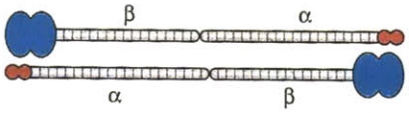	Cortical networks
Dystrophin	427,000		Muscle cortical networks
Filamin	280,000		Filopodia, pseudopodia, stress fibers
Fascin	55,000		Filopodia, lamellipodia, stress fibers, microvilli, acrosomal process
Villin	92,000	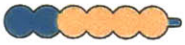	Microvilli in intestinal and kidney brush border

Table 1.1 Examples of ACPs. Blue indicates actin binding sites. Structural arrangement of the binding sites in ACPs determines whether they organize actin filaments into parallel bundles or orthogonal networks. Largely, large, long ACPs (e.g. filamin) tend to crosslink filaments at right angle, whereas short, small ACPs (e.g. fimbrin and fascin) are inclined to bundle filaments. (Adapted from [1].)

flexible arms and have tendency to organize the filaments into an orthogonal network found in cortical regions near a plasma membrane.

1.3. Molecular Motors

Unlike conventional materials, the cytoskeleton is not at thermal equilibrium; myosin, an active molecular motor walking on actin filaments in a polarized fashion via the consumption of ATP, generates internal stress, inducing high stiffness. This gives rise to a dynamic situation in which motors are under constant stress, stochastically unbind, reattach, and continue their motion along a new filament. Several types of myosin exist such as myosin I through XVIII. For instance, myosin V carries vesicles for transport and is a processive motor, meaning that a single myosin V alone is able to walk along filaments since it remains in a bound state for multiple steps [16]. By contrast, myosin II is a non-processive motor that binds to filaments for only a small fraction of lifetime, but self-assembles into a myosin minifilaments to increase processivity. These minifilaments are capable of producing contractile forces by pulling two actin filaments in opposite directions [17,18].

1.4. Previous Models for Cellular Mechanics

(Most of this section is adapted from [19].)

Over the past several decades, three major models have emerged, each of which has been applied to the cytoskeleton (Figure 1.3). Each differs fundamentally, however, in terms of the primary mechanism(s) that determine the elastic or viscoelastic properties of the network. In the cellular solids model [20,21], the material is depicted as an athermal network of beams with rigid connections, and stiffness is determined primarily by the

bending of these individual members. The second model, based on the concepts of tensegrity [22], proposes that the network consists of a balance between elements in tension and other elements in compression. In this model, the properties of the individual elements are relatively unimportant; network stiffness is determined instead by the level of tension in the system. The tensegrity model also neglects thermal effects. Finally, based on the assumption that crosslinks or entanglements occur over a length scale comparable to or smaller than the persistence length of thermally active filaments in the network, the cytoskeleton has been modeled as a semi-flexible polymer network [23]. The fourth model, based on the concepts of "soft glassy rheology" [24], will not be discussed here, in part because the fundamental physics giving rise to this behavior continues to be a source of some debate and uncertainty.

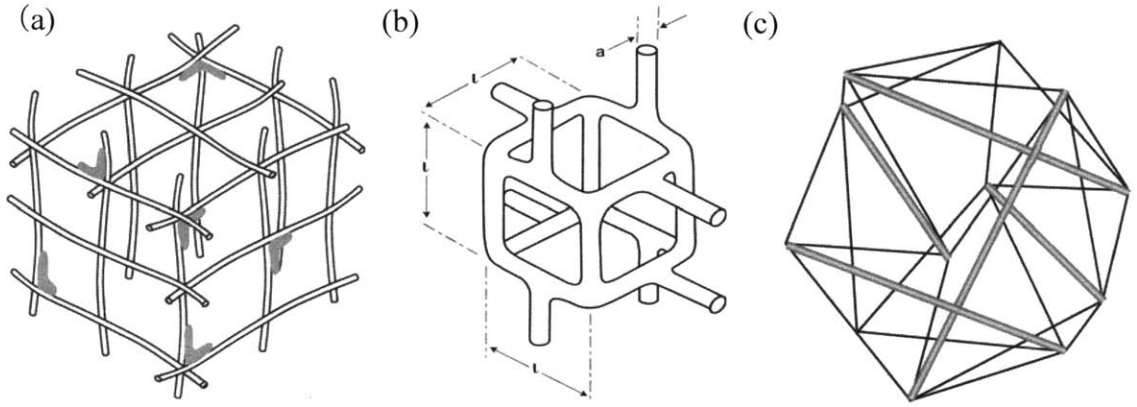

Figure 1.3 Schematic representations of three models for cellular mechanics. (a) Biopolymer model. The network is comprised of thermally active filaments with varying degrees of crosslinks (light gray). (b) Cellular solids. The cytoskeleton is assumed to consist of unit cells constructed from elastic beams with rigid connections. (c) Tensegrity. The network is presumed to be composed of elements that are maintained in a state of tension either by interactions with other compressive members (as shown) or by tethering to an external matrix (Adapted from [19]).

1.5. Previous Studies Investigating Actin Networks

Investigating the morphological and rheological properties of actin networks is indispensable for elucidating the mechanics of cells as well as for understanding a wide variety of cellular processes. Thus, various experiments have been conducted to probe viscoelastic properties of cells and reconstituted actin gels using a variety of techniques such as microbead rheology, magnetic bead cytometry, and bulk rheology [25-44]. In experiments, discrepancies have been observed among measurements using dissimilar methodologies, and many of the observed features are not well understood. For example, viscoelastic moduli measured by single-bead passive microbead rheology are much smaller than those determined by 2-point microrheology or bulk rheology [25,33,43]. Also, although distinct power law responses of the storage modulus have often been observed *in vivo* and *in vitro* [29-32,44], their origin is not yet clearly understood.

In addition, recent experiments [45,46] demonstrated that the unbinding and unfolding behaviors of a single ACP are rate-dependent, and can be described by several models for bond rupture or domain unfolding including Bell's equation [47]. However, the link between such dynamic behaviors of single ACPs and the integrated properties of an actin network remains poorly understood due to difficulties in relating macroscopic rheological measurements to underlying molecular events. Also, *in vitro* studies incorporating myosin II showed a dramatic increase in elasticity of actin gels due to the contractile activities of molecular motors [18,48]. Nevertheless, the full understanding about rheology of such actin-myosin networks is still lacking.

Concurrently, many theoretical and computational studies have been performed to

investigate characteristics of semi-flexible polymer networks including actin [49-59]. 2-D [49,50] and 3-D computational models [51] studying affine and nonaffine deformations of semi-flexible networks responding to large shear strain revealed two regimes dominated by bending or stretching of filaments, respectively. Recently, using a microstructure-based continuum mechanics approach, Palmer and Boyce reproduced many of the rheological properties of actin networks observed in experiments [52]. The viscoelastic behavior of semi-flexible networks was also investigated using dissipative particle dynamics and the concept of microbead rheology [53,54]. Effects of unbinding or unfolding event of ACPs on viscoelastic properties were investigated in several computational studies [60-62]. Recently, the rheology and morphology of actin-motor solutions have been studied in 2-D and 3-D computational models [63,64].

To date, however, most of these computational models are too simplistic, or did not either explicitly take into account ACP and motor mechanics or systematically account for thermal fluctuations, all of which are potentially important factors governing matrix viscoelasticity.

1.6. Thesis Overview

This thesis consists of three studies. In the first study, effects of prestrain, the concentration and type of ACPs, the mechanical stiffnesses of actin filaments and ACPs, and the thermal fluctuation of actin filaments on viscoelastic properties of networks were evaluated. The most important finding is that under conditions similar to cells, stretching of actin filaments and ACPs plays a significant role while the thermal fluctuation is

negligible. In the second study, we estimated the relative significance of two mechanisms of ACPs governing dynamic behaviors of actin networks – unbinding and unfolding – by probing the strain-stiffening, stress relaxation, and plastic deformation of the networks. We found that under typical experimental and physiological conditions, the unbinding event of ACPs is predominant, not unfolding. In the third study, we studied the roles of molecular motors in the morphology and rheology of actin networks. The motors highly enhance the elasticity of networks, leading to heterogeneous morphology.

Chapter 2

Investigating Rheology of Passive Actin Networks Crosslinked via Static Crosslinkers

(Most of this section is adapted from [19,65].)

2.1. Introduction

With the objective of extending previous computational works and providing new insights into underlying mechanisms, we develop a Brownian dynamics model of the actin network that includes features such as steric interaction among filaments, the usage of explicit crosslinkers, a more realistic morphology, and the consideration of crosslinker stiffness. By measuring stress in response to applied oscillatory shear strain ("bulk rheology") and thermal fluctuations of individual segments in the polymeric chain ("segment-tracking rheology"), we investigate viscoelastic properties of actin-like networks crosslinked by static crosslinkers showing neither unbinding nor unfolding event. It should be noted, however, that some of the properties employed in our model, especially for ACPs, were estimated since they are not well-known experimentally. Due to simplifications in the model and parameter uncertainty, the results should therefore be viewed as representative of a generic crosslinked network, but lack a quantitatively precise correspondence to actin networks.

Nevertheless, we found features that semi-quantitatively capture experimentally observed behaviors of actin networks. The storage and loss moduli, G' and G'', followed

power laws as functions of the oscillation frequency. As the prestrain increased, the network became increasingly elastic. Bending and extensional stiffnesses of actin filaments and ACPs played an important role depending on the degree of prestrain. We found that the mechanical response of the network is dominated by a percolating 'supportive framework,' while other actin filaments contribute little to the viscoelastic moduli. Surprisingly, in typical physiological conditions where the distance between crosslinking points along F-actin is much shorter than the actin persistence length, we found that thermal fluctuation plays little role in viscoelasticity, so that the network consisting of crosslinked F-actins can be viewed essentially as a deterministic overdamped system in a viscous medium. In sum, our computational model elucidates how various mechanical responses (thermal forces and the bending and stretching of actin filaments and ACPs) govern viscoelastic properties of the network under different conditions.

2.2. Methods

2.2.1. Dynamics and Mechanics

In this simulation, actin monomers, filaments, and ACPs experience thermal motion and interact with each other with defined potentials and binding probabilities. Individual displacements are governed by the Langevin equation:

$$m_i \frac{\mathrm{d}^2 \mathbf{r}_i}{\mathrm{d}t^2} = \mathbf{F}_i - \zeta_i \left(\frac{\mathrm{d}\mathbf{r}_i}{\mathrm{d}t} - \mathbf{v}_\infty \right) + \mathbf{F}_i^{\mathrm{B}} \tag{2.1}$$

where m_i is the mass of ith element (actin or ACP), $\mathbf{r}_i$ is the element's location, ζ_i is the friction coefficient, t is time, and $\mathbf{v}_\infty$ is the velocity of the surrounding medium. $\mathbf{F}_i$ is a net

deterministic force, and $\mathbf{F}_i^{\mathrm{B}}$ is a stochastic force satisfying the fluctuation-dissipation theorem. Considering that inertia of all elements is negligible on the length and time scales of interest, the Langevin equation is simplified by setting the acceleration term to zero and cast in nondimensional form using $k_{\mathrm{B}}T$, $\zeta_{\mathrm{C,A}}$, and $L_{\mathrm{C,A}}$ as primary variables, where $\zeta_{\mathrm{C,A}}$ and $L_{\mathrm{C,A}}$ are the friction coefficient and length of a segment of F-actin (as explained later). Positions of all elements are updated using the Euler integration scheme:

$$\tilde{\mathbf{r}}_i(\tilde{t}+\Delta\tilde{t}) = \tilde{\mathbf{r}}_i(\tilde{t}) + \frac{1}{\tilde{\zeta}_i}\left(\frac{\mathrm{d}\tilde{\mathbf{r}}_i}{\mathrm{d}\tilde{t}}\right)\Delta\tilde{t} = \tilde{\mathbf{r}}_i(\tilde{t}) + \frac{1}{\tilde{\zeta}_i}\left(\tilde{\mathbf{F}}_i^{\mathrm{B}} + \tilde{\mathbf{F}}_i\right)\Delta\tilde{t} + \tilde{\mathbf{v}}_\infty\Delta\tilde{t} \tag{2.2}$$

where dimensionless variables are indicated by the tilde "~". Two interaction potentials describe bond stretch and bending with stiffness $\tilde{\kappa}$, denoted by subscripts "s" and "b", respectively [66]:

$$\tilde{U}_{\mathrm{s}} = \frac{1}{2}\tilde{\kappa}_{\mathrm{s}}(\tilde{r}_{12}-\tilde{r}_0)^2, \quad \tilde{U}_{\mathrm{b}} = \frac{1}{2}\tilde{\kappa}_{\mathrm{b}}\left(\theta-\theta_0\right)^2 \tag{2.3}$$

where $\tilde{r}_{12}$ is the distance between two points constituting a chain, θ is the bending angle, and the subscript 0 denotes the equilibrium value.

2.2.2. Coarse-graining Scheme Using Cylindrical Segments

In our previous model [66], we treated a segment of F-actin as a spherical particle representing two G-actins. To simulate larger length and time scales, we introduced coarse-graining in which a cylindrical segment represents several monomers. We kept thermal forces on ACPs and actin segments in a form similar to our previous model, but incorporated a cylindrical geometry for calculating repulsive forces.

As seen in Figure 2.1, the points of two adjacent elements on a filament correspond to the ends of one cylindrical segment representing N_{C} actin monomers of the previous

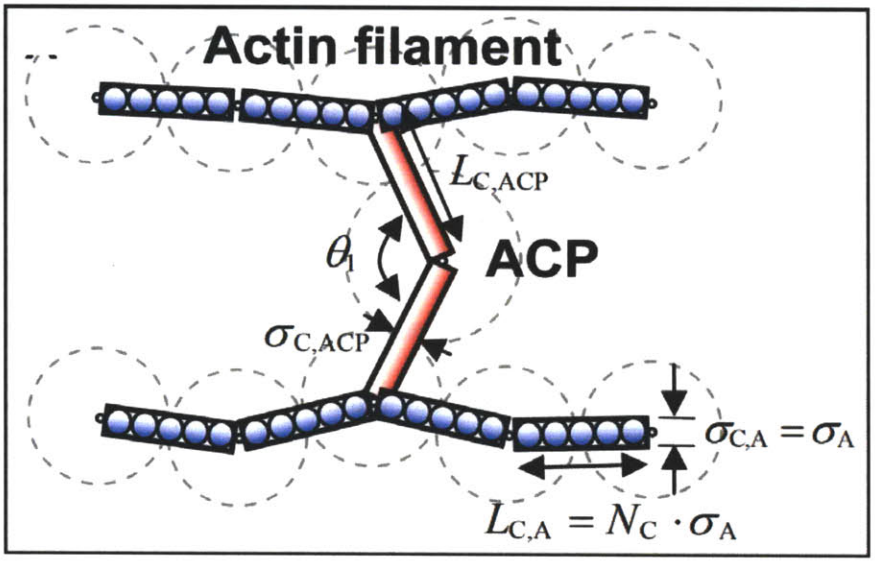

Figure 2.1 A coarse-graining scheme using cylindrical segments with N_C = 5. Dashed lines show monomers and ACPs used to generate the network using the polymerization model [66]. Once the network is formed, it is coarse-grained by replacing the original spheres by cylinders as shown.

model. Accordingly, the diameter of the cylindrical segment, $\sigma_{C,A}$, is the same as the diameter of actin monomer of the previous model, σ_A = 7 nm, and its length, $L_{C,A}$, is $N_C \cdot \sigma_A$. By letting each monomer of the polymerized network evolve into a cylindrical segment, a larger network is created, albeit with a lower concentration of ~1-100 μM. In addition, one point on a filament axis and the other point representing the center of an ACP determine the two end points of each arm of the ACP, indicating that ACPs have a structure with two cylindrical arms whose length and diameter are $L_{C,ACP}$ and $\sigma_{C,ACP}$ respectively. In this study, N_C was set to 10; this degree of coarse-graining is appropriate since the length of one rigid cylindrical segment, $L_{C,A}$ = 70 nm, is still much shorter than the persistence length of an actin filament, l_p ~10 μm.

One consequence of this coarse-graining technique is that it increases the arm

length of ACPs. That is, since the redundant volume of the original monomers is neglected, the arm length of ACPs is extended by $(L_{C,A} - \sigma_{C,A}) / 2$. This produces a network for which the shortest distance between two bundled filaments is $(L_{C,A} - \sigma_{C,A}) / 2$ (63 nm in this case) that exceeds the typical spacing formed by many of the bundling ACPs (e.g. fascin, fimbrin, and α-actinin). However, it is not expected that this will significantly alter the qualitative behavior of bundled networks since the change in the ACP arm length is much shorter than the length of F-actin. Previous experiments where different bundling ACPs led to distinct macroscopic behaviors [40,41] are more likely due to the different stiffness and dissimilar binding affinities of the ACPs rather than their physical size.

2.2.3. Calculation of Steric Effects between Cylindrical Segments

Repulsive forces are computed according to the following harmonic potential depending on the minimum distance, $\tilde{r}_{12}$, between two cylindrical segments, 1 and 2:

$$\tilde{U}_r = \begin{cases} \frac{1}{2}\tilde{\kappa}_r \left(\tilde{r}_{12} - \frac{\tilde{\sigma}_{C,i,1} + \tilde{\sigma}_{C,i,2}}{2} \right)^2 & \text{if } \tilde{r}_{12} < \frac{\tilde{\sigma}_{C,i,1} + \tilde{\sigma}_{C,i,2}}{2} \\ 0 & \text{if } \tilde{r}_{12} \geq \frac{\tilde{\sigma}_{C,i,1} + \tilde{\sigma}_{C,i,2}}{2} \end{cases} \tag{2.4}$$

where $\tilde{\sigma}_{C,i,1}$ and $\tilde{\sigma}_{C,i,2}$ are diameters of the cylindrical segments (i = A or ACP), and $\tilde{\kappa}_r$ is the strength of repulsive effects. Forces calculated from the potential (Equation 2.4), $\tilde{\mathbf{F}}_r$, are distributed onto the two end points constituting the cylindrical segment, α and β, via the following equations:

$$\tilde{\mathbf{F}}_{r,\alpha} = \tilde{\mathbf{F}}_r \frac{L_{C,i} - y}{L_{C,i}}, \quad \tilde{\mathbf{F}}_{r,\beta} = \tilde{\mathbf{F}}_r \frac{y}{L_{C,i}} \tag{2.5}$$

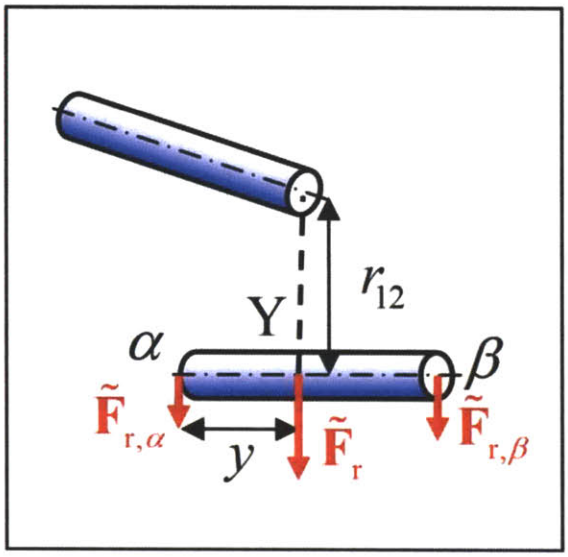

Figure 2.2 A schematic diagram showing the distribution of the repulsive force acting on point Y, $\tilde{\mathbf{F}}_r$ onto two end points, α and β. The proportion of each force is determined by y, the distance between point α and point Y.

where y is the distance between point α and point Y on the same segment ($0 \leq y \leq L_{C,i}$) in Figure 2.2.

2.2.4. Polymerization, Depolymerization, and Crosslinking

Monomer assembly and disassembly are important determinants of the morphology of actin networks. Given the rate constants obtained in recent *in vitro* experiments [67], it would take ~100 s for an actin filament 1.5 μm in length to completely depolymerize, or ~1-10 s to polymerize the same filament with C_A=12.1 μM. Though *in vitro* depolymerization of F-actin is very slow, various ACPs can accelerate it *in vivo*. However, we assume here for simplicity that neither polymerization nor depolymerization of actin filaments occurs within the time scale of interest in this study, ~1 s. Unlike our previous model [66], an ACP can bind to any point along an actin filament in any circumferential

direction. Neither unbinding nor unfolding of ACPs is permitted in this study.

2.2.5. Preparation of a Network to Estimate Viscoelastic Properties

The measurement of viscoelastic moduli can be influenced by the detailed geometry and the extent of percolation, especially if the network is small. Therefore, the use of a geometrically identical network for all simulations enables us to systematically control and isolate the effect of a given parameter. In other studies, actin networks have been generated by the random placement of equal-length filaments [49-51,54,57]. However, we generated more realistic networks using the previous model that incorporates both polymerization and crosslinking. A somewhat heterogeneous network bundled by ACP^B (Figure 2.3a) and a well-percolated, homogeneous network crosslinked by ACP^C (Figure 2.3b) were prepared. In Figure 2.3a, ladder-like structures consisting of two actin filaments and multiple ACP^B are evident, in contrast to thick bundles that are often observed in experiments. The relative absence of thicker bundles in these simulations is attributable to the small domain size compared to an average filament length. With N_C = 10, the filament length (L_f) is 1.5 μm ± 0.65 μm (average ± standard deviation), and the actin concentration (C_A) is 12.1 μM. We randomly removed ACPs to change R_{ACP} (Table 2.1), while maintaining the overall network geometry. In addition, actin filaments longer than the width of the simulation domain (2.8 μm) were severed to minimize finite size effects.

(a) (b)

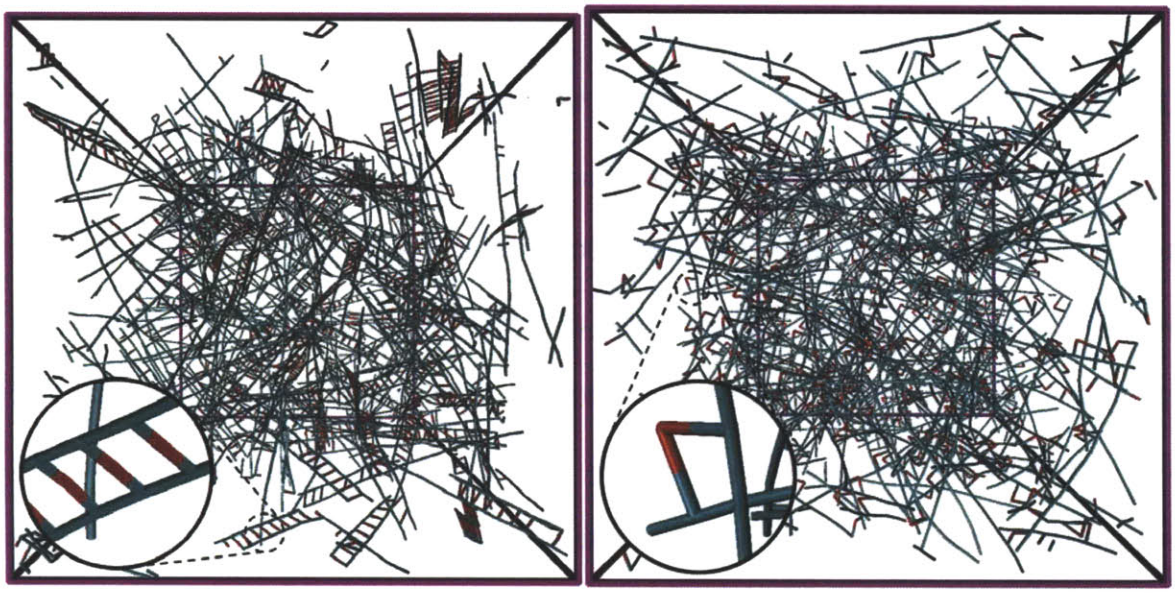

Figure 2.3 Two representative networks used in this study. (a) A network bundled via ACP^B and (b) crosslinked via ACP^C, both of which consist of actin filaments of various lengths (cyan) and ACPs (red). For visualization, VMD was used [68]. Two arms of each ACP drawn with partial red and cyan are connected to filaments, forming crosslinks. In (a), due to the small computational domain, ladder-like structures are predominant rather than long, thick bundles. The linear dimension of the simulation box is 2.8 μm. These two networks form the basis for all simulations; networks with low R_{ACP} were obtained from these by eliminating a portion of active ACPs. The inset of each plot shows the detailed geometry of bundled or crosslinked structures consisting of actin filaments and ACPs.

2.2.6. Adjusting Parameter Values for Coarse-graining

Upon coarse-graining, several parameters need to be adjusted. For the cylindrical geometry of the segments, approximate forms for friction coefficients are [69]:

$$\zeta_{C,i,\perp} = 3\pi\eta\sigma_{C,i} \cdot \frac{3 + 2L_{C,i}/\sigma_{C,i}}{5} \tag{2.6}$$

$$\zeta_{C,i,\parallel} = 3\pi\eta\sigma_{C,i} \cdot \frac{4 + L_{C,i}/\sigma_{C,i}}{5}$$

where η is the viscosity of the surrounding medium. However, since the mostly crosslinked cylindrical segments move predominantly in the transverse direction, and considering that $\zeta_{C,A,\perp}$ is only 1.64 times higher than $\zeta_{C,A,\parallel}$ ($L_{C,A}/\sigma_{C,A}$ = 10), $\zeta_{C,A,\perp}$ was used in all directions for simplicity. To test this assumption, we compared simulations with and without the anisotropic friction coefficient at zero prestrain. At f_s = 10 Hz, we obtained G' = 5.07 Pa (isotropic) and 5.00 Pa (anisotropic), and G'' = 2.02 Pa (isotropic) and 2.39 Pa (anisotropic). Since motion along the filament axis is more suppressed with prestrain, the effect of anisotropic friction coefficient will be even less. We also assumed a constant friction coefficient regardless of the filament length to which the segment belongs. Hydrodynamic interactions between filaments are expected to play little role and were ignored since the volume fraction of actin is low (~0.1 %), and because the filaments have high aspect ratio (long thin rod) [70].

Since the geometry of ACPs changes after coarse-graining, the following equilibrium values for additional harmonic potentials were used for ACP^B:

$$\tilde{L}_{C,ACP} = 0.7,\ \tilde{\sigma}_{C,ACP} = 0.143,\ \theta_{1,eq} = \pi,\ \theta_{2,eq} = \frac{\pi}{2} \tag{2.7}$$

$$\tilde{\kappa}_{s,ACP} = 5,000,\ \tilde{\kappa}_{b,ACP,1} = 250,\ \tilde{\kappa}_{b,ACP,2} = 1,000$$

and for ACP^C:

$$\tilde{L}_{C,ACP} = 1.45,\ \tilde{\sigma}_{C,ACP} = 0.143,\ \theta_{1,eq} = 0.417\pi,\ \theta_{2,eq} = \frac{\pi}{2} \tag{2.8}$$

$$\tilde{\kappa}_{s,ACP} = 5,000,\ \tilde{\kappa}_{b,ACP,1} = 250,\ \tilde{\kappa}_{b,ACP,2} = 1,000$$

where $\tilde{L}_{C,ACP}$ and $\tilde{\sigma}_{C,ACP}$ are the length and diameter of a cylindrical arm of ACP, $\theta_{1,eq}$ is the equilibrium angle between two arms of ACP, and $\theta_{2,eq}$ is the angle formed by an arm of ACP and the axis of the actin filament to which the ACP is bound. $\tilde{\kappa}_{s,ACP}$, $\tilde{\kappa}_{b,ACP,1}$, and $\tilde{\kappa}_{b,ACP,2}$ are stiffness constants related to $\tilde{L}_{C,ACP}$, $\theta_{1,eq}$, and $\theta_{2,eq}$, respectively (Figure 2.1).

Variable	Symbol	Value
Diameter of cylindrical actin segments	$\sigma_{C,A}$	7.0×10^{-9} [m] (0.1)
Length of cylindrical actin segments	$L_{C,A}$	7.0×10^{-8} [m] (1.0)
Time step	Δt	6.17×10^{-9} [s] (2.0×10^{-5})
Strength of repulsive force	κ_r	1.69×10^{-3} [N / m] (2,000)
Extensional stiffness of actin filament	$\kappa_{s,A}$	1.69×10^{-2} [N / m] (20,000)
Bending stiffness of actin filament	$\kappa_{b,A}$	1.06×10^{-18} [N m] (255.0)
Concentration of actin	C_A	1.21×10^{-5} [M]
Ratio of C_{ACP} to C_A	R_{ACP}	0, 0.01, and 0.021 (ACP^C)
		0, 0.01, 0.02, and 0.04 (ACP^B)
*Extensional stiffness of ACP	$\kappa_{s,ACP}$	4.23×10^{-3} [N / m] (5,000)
*Bending stiffness 1 of ACP	$\kappa_{b,ACP,1}$	1.04×10^{-18} [N m] (250.0)
*Bending stiffness 2 of ACP	$\kappa_{b,ACP,2}$	4.14×10^{-18} [N m] (1,000)
Viscosity of medium (water, 300 K)	η	0.8599×10^{-3} [kg / m s]
Boltzmann energy (300 K)	k_BT	4.142×10^{-21} [J] (1.0)

Table 2.1 List of adjusted parameters. Numbers in parentheses are corresponding dimensionless values as defined in the text. The value and notation of other parameters are the same as in [66].

* The same values are used for both ACP^B and ACP^C.

The value of $\theta_{2,eq}$ is the same as in the previous model, and $\theta_{1,eq}$ of ACP^C was adjusted to maintain an equilibrium minimal distance of 70 nm between two crosslinked filaments. $\tilde{\kappa}_{s,ACP}$ was set to be one fortieth that of an actin filament due to computational efficiency. $\tilde{\kappa}_{b,ACP,1}$ and $\tilde{\kappa}_{b,ACP,2}$ of ACP were estimated to be similar to the bending stiffness of an actin filament. Other parameters were also modulated according to the altered scale, as listed in Table 2.1. In our previous model by which the network was generated [66], a crosslink was allowed only if the torsional angle between two filaments was close to the equilibrium value (0 for ACP^B and $\pi/2$ for ACP^C), and a finite stiffness was assigned to the torsional angle between crosslinked filaments. However, because the other two bending forces can preclude free torsional rotation, the torsional force is neglected here for simplicity.

2.2.7. Bulk Rheology – Simulation

The concept of a strain-controlled bulk rheometer used in experiments was adopted in order to measure the viscoelastic moduli of the generated networks. First, all actin filaments were severed at the upper and lower boundaries, and the periodic boundary condition on those surfaces was deactivated. Cylindrical actin segments within 70 nm from the bottom surface were fixed, whereas those within the top 70 nm were forced to move following an imposed strain. For the application of prestrain, the top boundary was translated at a constant strain rate, $\dot{\gamma}_x$, up to the desired strain. To measure differential viscoelastic moduli as in [27], a small sinusoidal strain (5%) was superposed on top of the finite prestrain. The sum of forces on the ends of filaments attached to the top boundary was calculated, and divided by the area of the top surface to determine stress. Only the

force component parallel to the surface was considered. In addition, due to the small dimension of the system, the time scale for water diffusion through the computational domain is of order 10 μs. Since this is smaller than the smallest period of oscillatory strain, we assumed that the imposed shear strain immediately induces a linear velocity profile within the fluid. Consequently, after calculating the stress due to filament forces, we added a shear stress expressed as:

$$\tau_{zx} = \eta \frac{\mathrm{d}\gamma_x}{\mathrm{d}t} \tag{2.9}$$

where τ_{zx} is the shear stress exerted in the x-direction on a plane perpendicular to the z-direction (pointing from the bottom to the top face), and γ_x is the shear strain applied in the x-direction. The induced velocity of medium affects the movement of elements via the $\mathbf{v}_\infty$ term of Equation 2.2.

Finally, dividing the measured stress (τ_{zx}) by the differential strain (γ_x), viscoelastic moduli, G' and G'', can be evaluated:

$$\begin{aligned} \left|G^*(f_s)\right| &= \frac{\left|\tau_{zx}\right|}{\left|\gamma_x\right|} \\ G'(f_s) &= \left|G^*(f_s)\right|\cos\phi \\ G''(f_s) &= \left|G^*(f_s)\right|\sin\phi \end{aligned} \tag{2.10}$$

where ϕ is phase delay between strain and stress, and $\left|\tau_{zx}\right|$ and $\left|\gamma_x\right|$ are the amplitude of the differential stress and differential strain, respectively. Note that ϕ is zero for a perfectly elastic material and equals $\pi/2$ for a perfectly viscous one.

2.2.8. Bulk Rheology – Experiment *(performed with the help of Dr. Hyungsuk Lee)*

We also measured the mechanical properties of *in vitro* F-actin networks with a rheometer (AR-G2, TA Instruments) using a 40 mm parallel plate geometry. Lyophilized actin monomer from rabbit skeletal muscle was purchased from Cytoskeleton, Inc (Denver, CO). To minimize artifacts caused by sample preparations [71], the actin was stored at high concentration (10 mg/ml) at -80°C and thawed rapidly at 37°C before each experiment. Recombinant filamin A was purified from Sf9 cell lysates, and recombinant human gelsolin was produced in *Escherichia coli*. Solutions of gelsolin, filamin, actin polymerization buffer, and actin were gently mixed. The solutions were then loaded within 10 s into a rheometer to form a crosslinked F-actin network. After 2 hr of polymerization at room temperature, frequency-dependent shear moduli, G' and G'', were measured in the range of 0.1-10 Hz. To obtain mechanical properties in the linear elastic regime, strain was maintained below 2%.

2.2.9. Segment-tracking Rheology

Many experiments have used microbead rheology to probe viscoelastic moduli of actin gels based on the concept that the thermal motion of the bead is reflective of the gel's viscoelastic properties. Here, we used a variation of this approach, and tracked the mean square displacement (MSD) of individual actin segments. First, the domain was divided into a cubic lattice comprised of N_{MSD} cells (N_{MSD} = 512) of equal volume. Then, one cylindrical element was randomly selected per cell, and MSDs of the center of these elements were recorded over time. Using a well-known approximate method [72], G' and G'' were calculated from the MSDs. Considering that this method was initially designed

for a spherical bead, it was appropriately modified for cylindrical elements:

$$\begin{aligned} \left|G^*(\omega)\right| &\approx \frac{k_B T}{\pi r_b \left\langle \Delta r^2(1/\omega)\right\rangle \Gamma\left[1+\chi(\omega)\right]} \\ G'(\omega) &= \left|G^*(\omega)\right| \cos(\pi\chi(\omega)/2) \\ G''(\omega) &= \left|G^*(\omega)\right| \sin(\pi\chi(\omega)/2) \end{aligned} \tag{2.11}$$

where r_b is the effective radius of an actin segment, which satisfies $\zeta_{C,A,\perp} = 6\pi\eta r_b$. $\Gamma\left[1+\chi(\omega)\right]$ is the gamma function, where $\chi(\omega)$ is the power law exponent describing the logarithmic slope of $\left\langle \Delta r^2(t)\right\rangle$ at $\omega = 1/t$, $\chi(\omega) \equiv \left.\frac{\mathrm{d}\ln\left\langle \Delta r^2(t)\right\rangle}{\mathrm{d}\ln t}\right|_{t=1/\omega}$.

2.2.10. Computational Domain Size and Attainable Time Range

In spite of the coarse-graining using cylindrical segments, the length and time scales that our model can attain are still much smaller than those of usual experiments. For example, L_f in this computational model is a few microns at most, and the width of the 3-D domain is less than 5 μm. In such a small domain, it is difficult to investigate the effects of a wide range of L_f or C_A on viscoelastic moduli since L_f cannot be longer than the width of the domain to avoid artifacts associated with self-repulsion, and because an increase in C_A was achieved by a decrease in domain size with a constant number of molecules. If we increase the number of molecules, simulation time significantly increases. On the other hand, many *in vitro* studies have used quite long actin filaments (~20 μm) with relatively large systems of size ~O(1 mm). It takes about 16 days to reach 1 s in typical conditions using an Intel® Xeon® 2.66GHz CPU, but experimental results span up to 100-1000 s. Thus, an exhaustive comparison between computational and

experimental results was not possible.

2.3. Results

2.3.1. Comparison to Experiments *(with the help of Dr. Hyungsuk Lee)*

While recognizing the limitations of any direct quantitative comparisons between our model predictions and experiments, we conducted one set of experimental measurements under conditions similar to those of the simulation (mean filament length $<L_f>$ = 1.5 μm., R_{ACP} = 0.01, and C_A = 12.1 μM) and compared viscoelastic moduli. In

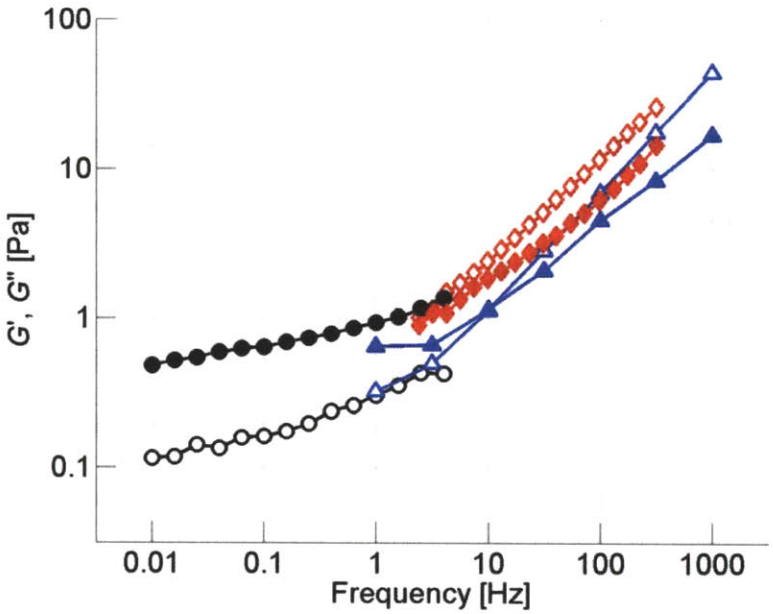

Figure 2.4 Comparison between computational and experimental results at $\langle L_f \rangle$ = 1.5 μm, R_{ACP} = 0.01, and C_A = 12.1 μM. Solid symbols: G', open symbols: G''. For simulation, bulk rheology (blue triangles) and segment-tracking rheology (red diamonds) were employed, while the experiment was conducted only using a bulk rheometer (black circles). Overlap occurs in the frequency range of 1-10 Hz.

order to match $<L_f>$, gelsolin was added to the sample; the length distribution was determined by fluorescence imaging. One difficulty in matching simulation and experimental conditions originates from the fact that R_{ACP} in the experiment corresponds to the total amount of ACPs in the sample, including both those in active and inactive (partially bound or free) states, whereas in our simulation, it indicates the net amount of active ACPs that crosslink or bundle two filaments. In addition, due to computational constraints, the oscillation frequency tested in the simulation overlaps that of the bulk rheology experiment only in a narrow range. Despite these difficulties, as seen in Figure 2.4, the values of G' and G'' computed using the model are in reasonable agreement with the experiment, both qualitatively and quantitatively, perhaps better than one might have expected given the range of uncertainty of some of the parameters.

2.3.2. Effects of the Concentration and Type of ACPs on G' and G''

We computed G' and G'' of structures crosslinked via ACP^C (R_{ACP} = 0, 0.01, and 0.021) and those bundled via ACP^B (R_{ACP} = 0, 0.01, 0.02, and 0.04) using both bulk rheology and segment-tracking rheology. Networks without ACPs exhibit a slope of G' close to 0.75, as indicated by the black solid line in Figures 2.5a and 2.6a. This value has been observed in various experiments [30,73-75], and it is known to originate from transverse thermal undulations of actin filaments [55]. Interestingly, when repulsive forces between the filaments are eliminated, the slope of G' estimated via segment-tracking rheology approaches unity (data not shown), implying that the volume exclusion effect of neighboring filaments creates a tube-shaped space that hampers free translation and rotation of the filament [56]. Although the filament confined in this way can perform reptation, it

is operative on long time scales that are beyond those attainable in these simulations, so the MSD observed here primarily reflects transverse thermal motions, resulting in the 0.75 slope. On the other hand, the plateau in G' often exhibited by experiments [28,33,76] was not observed within the frequency range of these simulations. Note that the plateau modulus is induced by entanglement effects that become more pronounced at longer time scales. The combination in these simulations of relatively short filaments leading to longer entanglement time [28] and computational constraints precluding simulations for longer times limited our ability to observe a plateau. Values of viscoelastic moduli attained using bulk rheology and segment-tracking rheology exhibit surprisingly good agreement (Figure 2.5) even though segment-tracking rheology (Equation 2.11) was originally developed for a test particle much larger than the meshwork of filaments [72]. ACP^C elevates the magnitude of G' and reduces its slope (Figure 2.5a), implying that the frequency dependence of G' is reduced as networks incorporate more ACP^C. G' follows a power law, $G' \sim f_s^{0.3}$ (dashed line), for $f_s < 100$ Hz at the highest crosslink density, $R_{ACP} = 0.021$, which is within the range of powers observed in cells, 0.15-0.3 [29,32,44]. However, the magnitude of G' from these simulations was much lower than *in vivo* values. This is likely due to many factors, notably the absence of prestrain. G'' increases slightly as the amount of ACP^C is increased, but the slope remains similar (Figure 2.5b). In addition, a decrease in the phase delay, $\tan^{-1}(G''/G')$ (Equation 2.10), accompanies the increase in R_{ACP}, indicating that ACP^C elevates the elasticity of the network. At $f_s \sim 10^3$ Hz, the phase delay depends only weakly on R_{ACP}, but as frequency decreases, it decreases more quickly with higher R_{ACP}, implying a greater effect by crosslinking at lower frequencies.

Networks bundled by ACP^B exhibit a behavior distinctly different from that of ACP^C (Figure 2.6). Large differences in G' and G'' were observed between segment-tracking rheology and bulk rheology. This originates from the heterogeneity of the bundled network attributable to the small computational domain, for which viscoelastic moduli measured by bulk rheology depend strongly on whether or not there are bundles that percolate between the top and bottom boundaries. We thus discuss results of only segment-tracking rheology for networks formed by ACP^B.

ACP^B increases G' but has little effect on its slope in contrast to ACP^C (Figure 2.6a), whereas the phase delay is only slightly influenced by R_{ACP}. ACP^C is able to form a well-percolated network even at relatively low R_{ACP}, so that the network gels more efficiently [27] and acts like a single-body elastic object in response to shear stress or strain. By contrast, ACP^B bundles filaments together, resulting in the relatively low level of

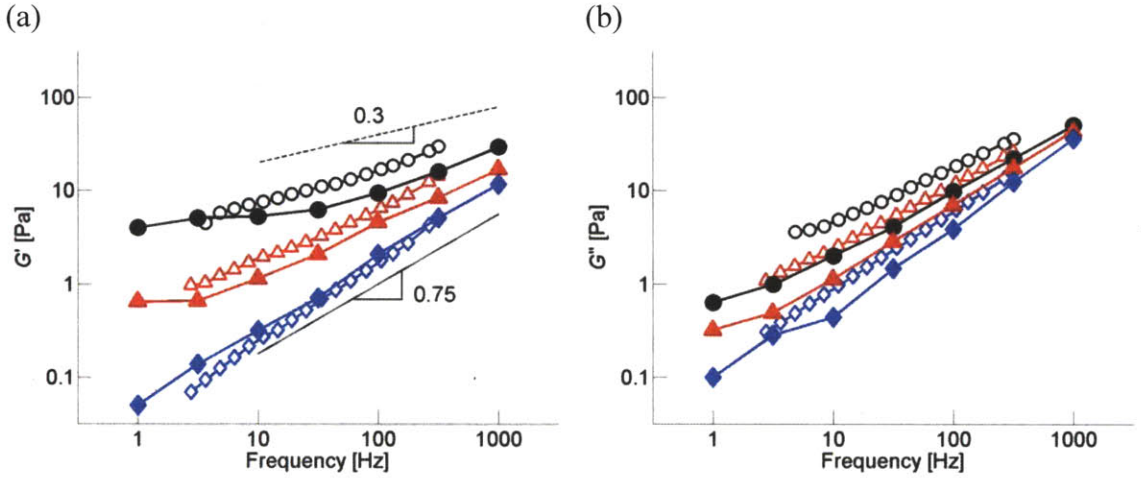

Figure 2.5 Viscoelastic moduli of networks crosslinked by ACP^C. (a) G' and (b) G''. Open symbols: segment-tracking rheology, solid symbols: bulk rheology. R_{ACP} = 0.021 (black circles), 0.01 (red triangles), and 0 (blue diamonds). With more ACP^C, the magnitude of G' increases, and its slope decreases. G'' is slightly larger for networks with higher R_{ACP}.

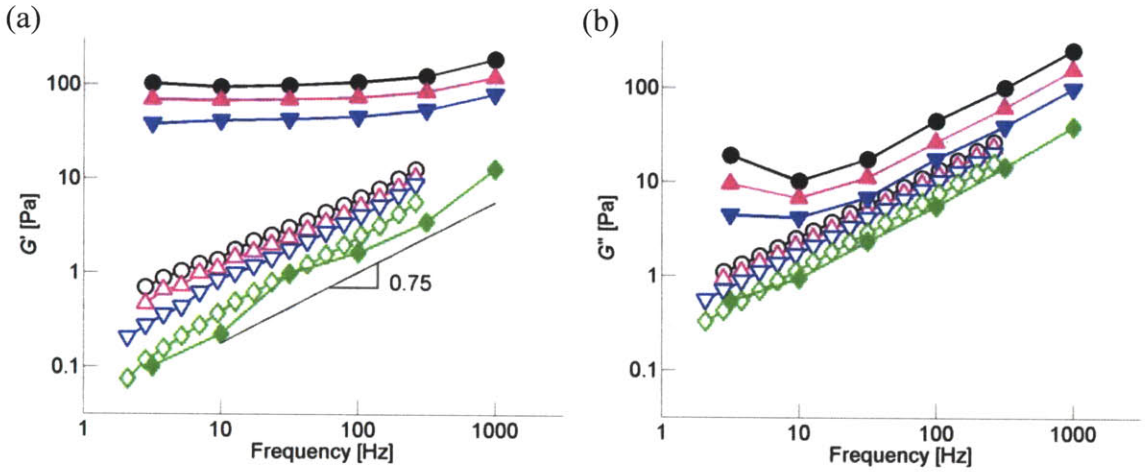

Figure 2.6 Viscoelastic moduli of networks bundled by ACP^{B}. (a) G' and (b) G". Open symbols: segment-tracking rheology, solid symbols: bulk rheology. R_{ACP} = 0.04 (black circles), 0.02 (magenta triangles), 0.01 (blue inverted triangles), and 0 (green diamonds). Large discrepancies exist between results obtained by segment-tracking rheology and by bulk rheology with nonzero R_{ACP} due to heterogeneity of the bundled network.

percolation for the same value of R_{ACP} as reflected by its low connectivity [66]. Although the diffusivity of bundled filaments is lower, the lack of connectivity leads to the absence of elastic behavior at long time scales. In order for ACP^{B} to increase network elasticity to a similar extent by ACP^{C}, its concentration may have to be much higher.

2.3.3. Effects of Prestrain on *G*' and *G*"

Only bulk rheology is employed here since the application of prestrain leads to a highly nonuniform distribution of the load, with a small fraction of highly tensed filaments and a larger number of filaments under little or no stress. Due to such heterogeneity, segment tracking rheology underestimates G' and G" as it randomly traces N_{MSD} segments from the entire network. The effect of prestrain on G' is analogous to that of ACP^{C}. As

seen in Figure 2.7a, G' increases and produces a weaker dependence on frequency at higher prestrain (γ); at γ = 0.55, G' is virtually independent of frequency and is nearly 100-fold larger than that at γ = 0 for f_s < 10 Hz. This means that large prestrain transforms the network into a highly elastic one that exhibits a phase delay close to 0 at all frequencies and results in G' comparable to *in vivo* values [29,32,44], wherein it has been postulated that prestress or prestrain plays a significant role [27]. G" also exhibits interesting behavior; at high prestrain, it increases slightly at low frequency, similar to *in vitro* observations using heavy meromyosin (HMM) [38,77], and a similar increase in G" was also observed *in vivo* [39,74]. This suggests that at low frequencies, viscous effects play an important role. Tharmann and coworkers argued that this trend of G" may be due to the unbinding of HMM. However, since unbinding was not permitted in these simulations, the increase in

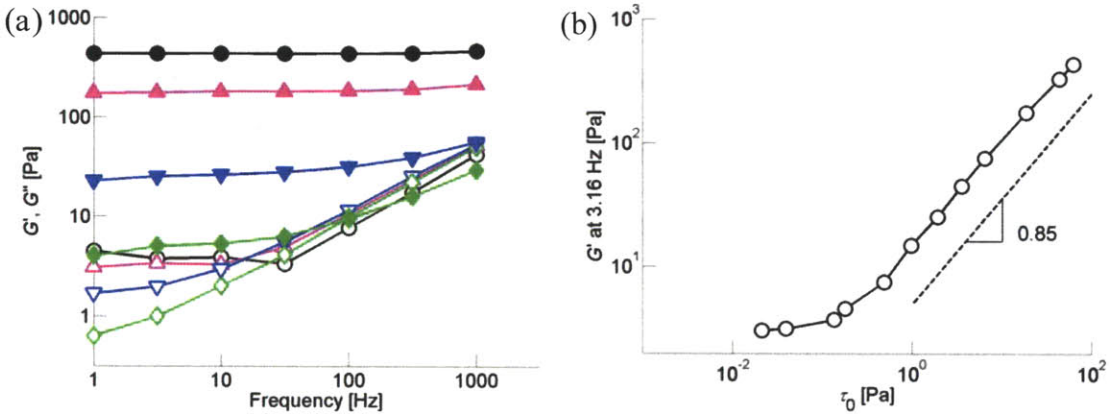

Figure 2.7 Behaviors of prestrained networks. (a) G' (solid symbols) and G" (open symbols) of networks with R_{ACP} = 0.021 at various prestrain: γ = 0.55 (black circles), 0.4 (magenta triangles), 0.2 (blue inverted triangles), and 0 (green diamonds). At high prestrain, G' becomes nearly independent of frequency. G" with high prestrain slightly increases at low frequency. (b) G' at f_s = 3.16 Hz versus prestress, τ_0. G' begins to increase at about 0.1 Pa and follows a power law, $G' \sim \tau_0^{0.85}$.

the low-frequency G" with prestrain must originate from a different mechanism. Note that such a tendency may have been more evident if the simulations were capable of reaching even lower frequencies.

Also, the relation between G' at f_s = 3.16 Hz and prestress (τ_0) was investigated. It remains relatively constant until a threshold prestress ($\tau_0 \sim 0.1$ Pa, Figure 2.7b) beyond which it increases following a power law, $G' \sim \tau_0^{0.85}$. The exponent of 0.85 is close to the value of ~1 found in *in vitro* experiments under similar conditions [27].

2.3.4. Effects of Extensional Stiffness of Actin Filaments, $\kappa_{s,A}$

To illustrate how prestrain transforms a network into a more elastic one, we display the network using a color scale depending on bond length averaged for duration of 0.1 ms. Only a small number of actin filaments aligned in the x-z direction are highly stretched (Figure 2.8a,b). As mentioned above, this heterogeneity precludes using segment-tracking rheology which measures thermal motions of randomly selected segments, many of which are not a part of the highly stretched filaments in prestrained networks. The mean filament length of the entire network increased by only 0.5% with $\gamma = 0.55$. However, due to the large value of $\kappa_{s,A}$ (Table 2.1), this results in large spring forces that contribute significantly to the high magnitude of G'.

We also performed simulations with different extensional stiffness ($\kappa_{s,A}$ = 0.0338 and 0.0068 N/m) for networks with γ = 0.55 (Figure 2.8c). G' and G" decreases with lower $\kappa_{s,A}$, but its phase delay is virtually unchanged (data not shown). When γ = 0, however, variation in $\kappa_{s,A}$ has little or no effect since most actin filaments are not highly stretched (Figure 2.8d). Therefore, $\kappa_{s,A}$ affects viscoelasticity only under high prestrain.

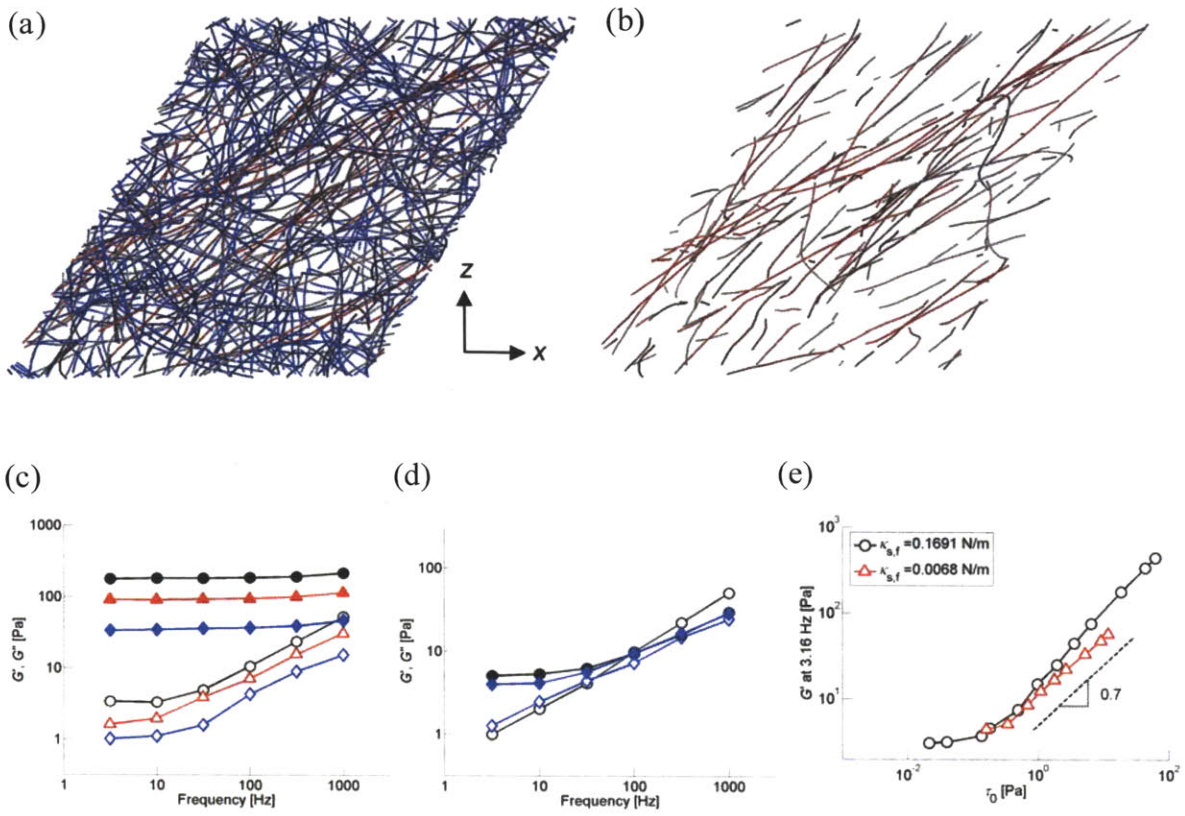

Figure 2.8 Importance and effects of extensional stiffness of actin filaments in prestrained networks. (a) Color-map of the prestrained network with $\gamma = 0.55$ (red: highly stretched bonds, gray: intermediately stretched bonds, blue: least stretched bonds. (b) Similar plot showing only actin filaments with bonds stretched by more than 0.5%. (c,d) Influence of the extensional stiffness of actin filaments, $\kappa_{s,A}$, on G' and G'' for a network crosslinked by ACP^C ($R_{ACP} = 0.021$) at (c) $\gamma = 0.55$ and (d) $\gamma = 0$. Solid symbols: G', and open symbols: G'' with $\kappa_{s,A} = 1.69\times10^{-2}$ (black circles), 3.38×10^{-3} (red triangles), and 6.76×10^{-4} N/m (blue diamonds) (e) G' at f_s=3.16 Hz as a function of prestress, τ_0, for $\kappa_{s,A} = 6.764\times10^{-4}$ (red triangles) and 0.01691 N/m (black circles). G' of both cases remains nearly constant at low prestress, but starts to increase above ~0.1 Pa. The behavior is similar for the two values of $\kappa_{s,A}$ except that lower $\kappa_{s,A}$ leads to a slight reduction in both the level and slope (~0.7, dashed line) of G' above the threshold stress level.

We also studied the influence of $\kappa_{s,A}$ on G' (f_s = 3.16 Hz) at different levels of prestress, τ_0 (Figure 2.8e). Interestingly, when $\kappa_{s,A}$ is reduced to 0.0068 N/m, the previous slope of 0.85 decreases to about 0.7, suggesting that the slope of the curve in the nonlinear regime increases with $\kappa_{s,A}$. Note that we used a value of $\kappa_{s,A}$ that is 1/40 of the experimentally measured value due to computational efficiency. Our result is thus consistent with a larger slope observed in experiments, ~1 [27].

2.3.5. Effects of Bending Stiffness and Thermal Fluctuation of Actin Filaments

To address factors affecting viscoelasticity at low prestrain, we probed the influence of actin filament bending stiffness, $\kappa_{b,A}$, by using three different values ($\kappa_{b,A}$ = 1.056×10^{-18}, 1.056×10^{-19}, and 1.056×10^{-20} Nm) at $\gamma = 0$ (Figure 2.9a) and 0.4 (Figure 2.9b). At high prestrain, $\gamma = 0.4$, variations in $\kappa_{b,A}$ have little effect on G' and only minor effects on G'', suggesting that in the high prestrain regime, actin bending stiffness does not play a major role in viscoelastic properties (Figure 2.9b). By contrast, at $\gamma = 0$, $\kappa_{b,A}$ influences G' (Figure 2.9a), although perhaps not to the extent that one might expect for reductions in $\kappa_{b,A}$ by factors of 10 and 100.

We also studied the effect of thermal fluctuation of actin filaments using separate simulations with or without the Langevin force term, $\mathbf{F}_i^B$ (Equation 2.1), at various γ and l_p ($\sim \kappa_{b,A}/k_BT$, with T = 300 K) (Figure 2.9c). Without $\mathbf{F}_i^B$, the temperature of the system drops to ~10 K, as measured by applying the equipartition theorem, where the nonzero temperature is due to the externally imposed oscillation. Figure 2.9c shows the ratio of G' without thermal fluctuation (TF) to that with TF at f_s = 10 Hz under each condition. At high prestrain ($\gamma \geq 0.4$), the elimination of TF does not affect G' regardless of l_p.

Surprisingly, for filaments with bending stiffness comparable to that of actin (l_p = ~10 μm), elimination of thermal effects had no significant effect on G' at any value of γ. Only when $\kappa_{b,A}$ was decreased ($l_p \leq 3$ μm) did thermal fluctuations have a noticeable influence on G'. Under these conditions, l_p became comparable to the average distance between crosslinks, l_c, (0.393 μm at R_{ACP} = 0.021), in which entropic effects would be expected to play a role [35], especially with a low prestrain. However, it is not clear whether this range of conditions can be attained *in vivo*. This finding that the relation between l_p and l_c determines the importance of thermal fluctuations is consistent with previous qualitative predictions [49]. Yet, our result is at odds with a previous view that entropic effects due to thermal undulations of individual filaments are responsible for the elasticity of scruin-crosslinked [35,36] and HMM-crosslinked [38] networks even in the case when $l_c << l_p$. In previous numerical studies [50,51], thermal fluctuations were applied only before applying shear strain, not during the measurement of stress, and thus they cannot be used as a clear demonstration that thermal fluctuations are important. Further experimental, numerical, and theoretical investigations are necessary to clarify the role of thermal fluctuation and entropic elasticity. For instance, if network elasticity is mainly governed by enthalpy, and if thermal fluctuation plays little role, we expect that G' will be minimally affected upon adding crowding agents to increase solvent viscosity and to provide steric barrier to conformational motion. However, crowding agents may affect organization of filaments, such as enhanced bundling [78]. Thus, such experiments will need to be carefully interpreted. Also, the vibrational motion of actin filaments depending on l_c measured in a computational study can be compared to theoretical predictions in [49].

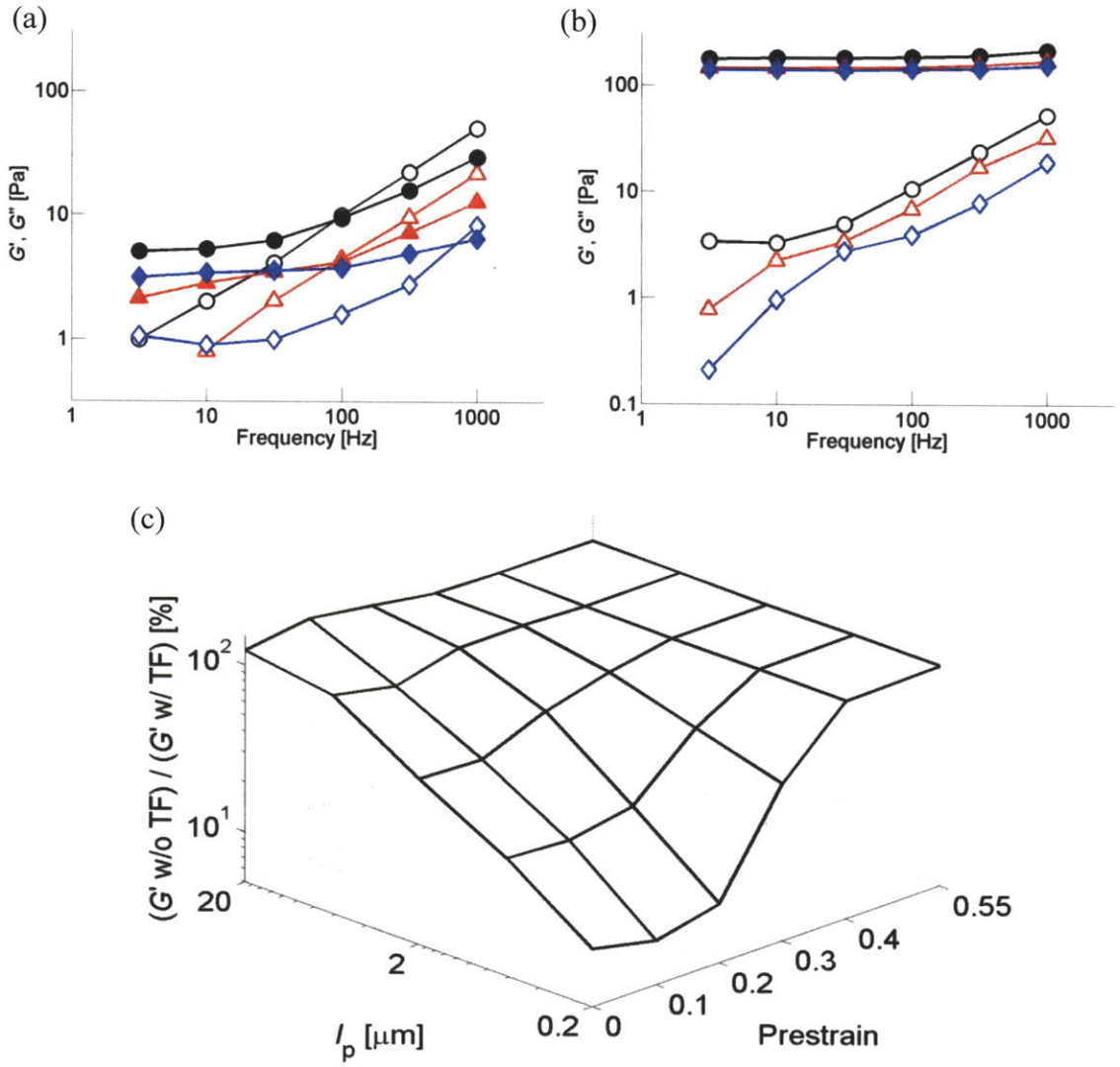

Figure 2.9 Effects of bending stiffness and thermal fluctuation on G' and G''. (a,b) Effects of bending stiffness of actin filaments, $\kappa_{b,A}$, on G' (solid symbols) and G'' (open symbols) for a network crosslinked by ACP^C (R_{ACP} = 0.021) at (a) γ = 0 and (b) γ = 0.4. $\kappa_{b,A}$ = 1.056×10^{-18} (black circles), 1.056×10^{-19} (red triangles), and 1.056×10^{-20} Nm (blue diamonds). The changes in $\kappa_{b,A}$ have large effects on G' and G'' in (a) but not in (b). (c) Effects of thermal fluctuation (TF) of actin filaments on G' at f_s = 10 Hz as a function of γ and l_p (calculated at 300 K). At high γ ($\geq$ 0.4) or large l_p (~10 μm), TF plays no significant role in G'. On the contrary, at low γ and l_p, G' decreases without TF.

2.3.6. Effects of Bending and Extensional Stiffnesses of ACPs

Previous studies showed that the detailed structure of ACPs strongly influences viscoelastic moduli of actin networks. In [26], each synthetically constructed crosslinking molecule of a different length produced distinctive macroscopic mechanical behaviors. In addition, Gardel et al. observed significantly different stress-strain relationships between a reconstituted actin network with intact filamin A (FLNa) and one with mutated hingeless FLNa [27].

Since these previous results led us to anticipate substantial effects of ACPs in our actin networks, we investigated the influence of bending stiffness of ACP^C, $\kappa_{b,ACP,1}$ and $\kappa_{b,ACP,2}$. As described in Methods, $\kappa_{b,ACP,1}$ acts between two arms of the ACP, whereas $\kappa_{b,ACP,2}$ limits bending between one arm of the ACP and the axis of actin filament to which it is attached, with an equilibrium value of $\pi/2$. To study their effects, we decreased both $\kappa_{b,ACP,1}$ and $\kappa_{b,ACP,2}$ 10 fold, 100 fold, and to zero. This had a significant effect on G' and G'' at all prestrains (Figure 2.10), but especially so for the magnitude of G' in the highly prestrained case with $\gamma = 0.4$. At small prestrain ($\gamma = 0$), deformation is mostly associated with the bending of actin filaments, and the ACP angles remain close to their equilibrium values. As prestrain increases (to 0.4), the actin filaments are progressively straightened, especially those that support the bulk of the load. Since this is accompanied by changes in the angle between crosslinked actin filaments, bending stiffness of ACPs becomes an important determinant of G'. As prestrain further increases (to 0.55), ACPs are maximally bent, and stretching of actin filaments is the dominant mechanism for resisting deformation since changing the extensional modulus has the greatest influence on G'. It should be noted, however, that though the geometry of ACP^C mimics that of FLNa, the large values of

$\kappa_{b,ACP}$ are closer to that of stiff scruin. Studies involving mutant ACP^C (e.g. FLNa) that differs in bending stiffness would further clarify our observation.

A change in extensional stiffness of ACP^C, $\kappa_{s,ACP}$, results in little change in G' and G'' (data not shown) at low γ, but plays a significant role at high γ. This tendency is not surprising as unbending of the V-shaped ACP^C should precede stretch of ACP^C arms responding to the load.

2.3.7. Significance of Each Parameter at Various Prestrains

Based on the effects of bending and extensional stiffnesses of actin filaments and ACPs as well as thermal fluctuations discussed above, we can estimate the relative importance of each factor over a wide range of prestrain and identify regimes where different phenomena dominate the viscoelastic behavior. For this purpose, each stiffness was decreased by 25-fold from the standard case, and the ratio of G' with the decreased

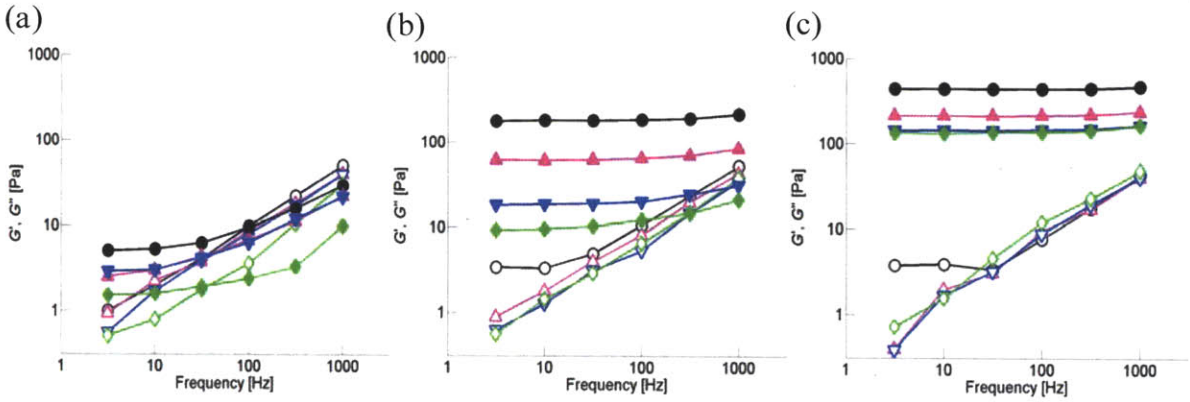

Figure 2.10 Effects of bending stiffnesses of ACP^C, $\kappa_{b,ACP,1}$ and $\kappa_{b,ACP,2}$, on G' and G''. The network is crosslinked by ACP^C with and without prestrain (R_{ACP} = 0.021). Solid symbols: G', open symbols: G''. $\kappa_{b,ACP}$ = control (black circles), 10-fold decrease (magenta triangles), 100-fold decrease (blue inverted triangles), and 0 (green diamonds) (a) γ = 0, (b) γ = 0.4, (c) γ = 0.55. The effects of changes in $\kappa_{b,ACP}$ on G' are the greatest in the network with γ = 0.4.

stiffness to that with the normal stiffness was computed at f_s = 10 Hz (Figure 2.11). A fall in extensional stiffness of both actin filaments ($\kappa_{s,A}$) and ACPs ($\kappa_{s,ACP}$) decreases G' more as γ increases, implying that the stretch of filaments and ACPs plays an important role in strain-stiffening behavior at high γ, at least at the exaggerated levels of extensional compliance used in the simulations. Bending stiffness of ACPs, $\kappa_{b,ACP}$, is significant at all tested γ, but has the largest effect on G' for $\gamma \sim 0.3$-0.4. The influence of bending stiffness of actin filaments, $\kappa_{b,A}$, on G' is interesting, passing through a minimum at γ = 0.2. We measured G' under the same conditions but without thermal fluctuation, and the minimum at γ = 0.2 disappeared; the ratios at γ = 0-0.2 are similar to each other. Therefore, thermal fluctuation of actin filaments contributes to an increase in G' at low γ when l_p is comparable to l_c.

Based on these observations, we propose three distinct regimes: i) A low γ regime where $\kappa_{b,A}$ is dominant, with thermal fluctuations playing a substantial role for $l_p \leq l_c$. ii) An intermediate γ regime in which the effect of $\kappa_{b,ACP}$ becomes dominant. iii) A high γ regime where $\kappa_{s,A}$ and $\kappa_{s,ACP}$ are the predominant factors. Transition from one regime to another, however, is not sharply defined. Others [50,51] have also argued that bending stiffness of filaments would dominate in the low γ regime, and extensional stiffness of filaments in the high γ regime, but they did not consider stiffness of ACPs as a parameter. Also, since these previous simulations lacked thermal fluctuations, their relative effects could not be assessed.

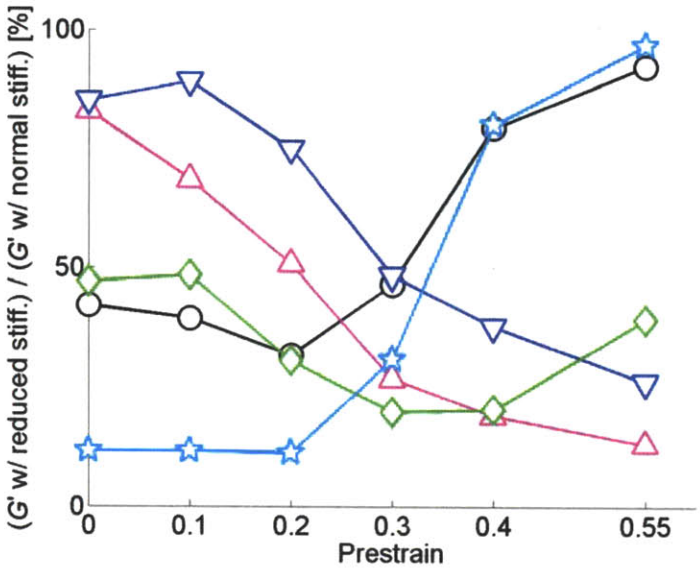

Figure 2.11 Relative decrease in G' at f_s = 10 Hz due to 25-fold decrease of various stiffnesses at different prestrains. Magenta triangles: $\kappa_{s,A}$ /25, blue inverted triangles: $\kappa_{s,ACP}$/25, green diamonds: $\kappa_{b,ACP}$/25, black circles: $\kappa_{b,A}$ /25 with thermal fluctuation, and cyan stars: $\kappa_{b,A}$ /25 without thermal fluctuation. R_{ACP} = 0.021 was used. The influence of $\kappa_{s,A}$ and $\kappa_{s,ACP}$ increases at higher γ, and $\kappa_{b,ACP}$ is significant at all prestrains. The effect of $\kappa_{b,A}$ on G' increases as γ decreases, and by comparing stars and circles, it can be inferred that thermal fluctuation plays an important role at very low γ when l_p is comparable to or less than l_c.

2.3.8. The Supportive Framework Governing Viscoelastic Moduli

Figure 2.8b shows that only a subset of the entire network supports the dominant portion of the stress in prestrained networks. While there could be many different criteria for identifying such a 'supportive framework,' we considered two, based either on the stretch of actin filaments or on the bending of ACPs. In the first case, we deleted filaments that were not highly stretched. The remaining network, however, when oscillated at the same strain amplitude, produced very low stress levels, suggesting that a significant fraction of the stress-supporting elements had been removed by this process.

In the second case, we use bending force on ACPs as a selection criterion since the change in $\kappa_{b,ACP}$ had a strong effect on viscoelastic moduli (Figure 2.10). First, the sum of magnitudes of all bending forces applied on each ACP in a prestrained state was calculated during 0.1 ms, the portion of ACPs with the highest bending forces were selected, and the remaining ACPs were deleted. All actin filaments not connecting between a pair of these highly strained and bent ACPs were removed. We compared stresses exerted on networks in which 25%, 50%, and 75% of ACPs remain under the same imposed prestrain. The network containing only 25% of initial ACPs (Figure 2.12a) consists of filaments oriented mostly in the diagonal direction on the x-z plane (*cf.*, Figure 2.8b). Moreover, as the orientational distribution shows (Figure 2.12b, inset), there are (less stretched) filaments oriented in other directions that also help to transmit the applied load, by bending of connecting ACPs, which are not selected when a criterion based on stretch of actin filaments is used. The mean stress and oscillation amplitude of the reduced network remain nearly at original levels (Figure 2.12b). For example, the network containing only ~28% of the original actin filaments and ~25% of ACPs produced ~70% of the original mean and amplitude of oscillating stress at the same levels of strain. Thus, bending force on ACPs is a major determinant of the elasticity of prestrained networks. We also confirmed that at high prestrain, ACPs experiencing large bending forces tend to displace in a manner consistent with the deformations being affine, as measured by the S parameter used in [79] (data not shown). This means that parts of the supportive framework that bear greater levels of force experience more affine deformation. It is well known that most cells are in a prestressed state largely due to the actomyosin contractile apparatus [22,32,80]. By analogy, we hypothesize that the large G' (~10^3 Pa) measured in cells is

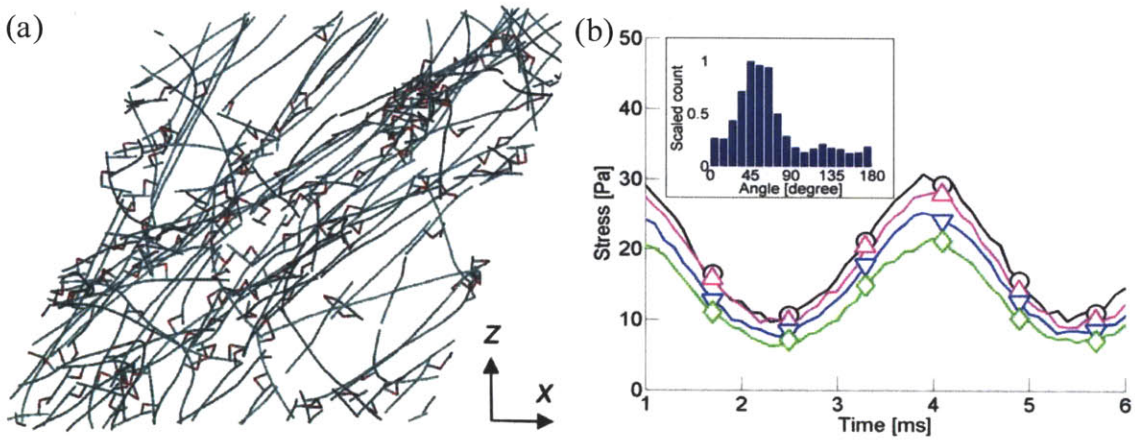

Figure 2.12 The supportive framework bearing most of stress. (a) Network composed of filamentous actin connected via ACPs that support the highest 25% of ACP bending forces. In contrast to Figure 2.8b, there are filaments that are almost perpendicular to the diagonal direction on the x-z plane, which are not highly stretched yet transmit load by bending of ACPs connected to them. (b) Stress exerted by prestrained networks ($\gamma = 0.4$) consisting of a fraction of actin filaments and ACPs. The extent of ACP bending forces is employed as a criterion to retain elements. Each symbol corresponds to a different percentage ratio of the number of ACPs remaining in a rebuilt network to that in the original network: 100% (black circles), 75% (magenta triangles), 50% (blue inverted triangles), and 25% (green diamonds). The fraction of remaining actin segments is, respectively: 100%, 79%, 52%, and 28%. (*inset*) Orientation angles of actin segments projected onto the x-z plane for the network in Figure 2.12a. Segments oriented in the z-direction have a value of 0°. Most actin segments in the reduced structure are oriented in the (+x)-(+z) direction (45°), but segments with other orientations are also important, presumably because they transmit stress through bending of the ACPs attached to them.

mostly due to the supportive framework composed of the contractile apparatus while the rest of cytoskeletal structures play comparatively little role in the macroscopic viscoelasticity of cells.

2.4. Discussion

In this study, with a computational simulation using Brownian dynamics and rheological techniques, systematic investigations of viscoelastic moduli of actin-like networks were performed. First, we validated our model by comparing viscoelastic moduli of a network with an outcome from an experiment conducted using bulk rheometer under similar conditions. Then, the effects of the kind and concentration of ACPs on G' and G'' were investigated. With no ACP, a slope of 0.75 reflecting the transverse thermal motion of actin filamets appears. ACP^C has a more powerful ability to transform a network into very elastic one correponding to a lower G' slope and small phase delay than ACP^B. The influence of prestrain on G' and G'' was also studied. High prestrain makes networks quite elastic with G' independent of frequency mainly via the stretch of a small fraction of actin filaments aligned in a specific direction. Then, the effects of extensional and bending stiffness of actin filaments and ACPs on viscoelasticity were tested individually. We found that for viscoelsatic moduli, there are three regimes governed by different mechanisms depending on the amount of prestrain. At a very low prestrain close to 0, bending stiffness of ACPs and actin filaments play an important role to determine viscoelasticity. At an intermediate prestrain, bending stiffness of ACPs has the greatest effect, and the other stiffnesses also contribute to viscoelastic moduli. At a quite high prestrain, the extensional stiffnesses of actin filaments and ACPs become dominant factors. In addition, we studied and discussed thermal fluctuation of actin filaments. When the average distance between active ACPs is comparable to persistence length, entropic spring effects related to the thermal fluctuation are quite important at relatively low prestrains.

More systematically, we also probed a drop in G' at 10 Hz responding to a 25-fold reduction in the extensional and bending stiffnesses of actin filaments and ACPs at six prestrains. Lastly, we searched the supportive framework that determines most of viscoelastic characteristics in prestrained networks using the bending forces of ACPs as the criterion for finding it. Even after 75% of network components are deleted, mean stress and oscillaion amplitude remain at 70% of original values.

When these results are interpreted in the context of the different models for cellular mechanics mentioned in Section 1.4, each is found to have certain advantages and disadvantages depending on the level of prestrain in the cytoskeletal network. In the case of tensegrity, it is only fair to draw comparisons at elevated prestrains, since without them, and lacking any compressive elements such as the microtubules, tensegrity would predict a zero modulus. To the extent that tensegrity is a useful model, one would expect two salient features [81]: that the modulus would be a linear function of prestress, and that it would be nearly independent of the elastic properties of the network constituents, in this case, the actin filaments and crosslinking proteins. Indeed, both of these features of the tensegrity structure were exhibited by the model, as can be seen by plotting the same data as Figure 2.11 but in terms of prestress vs. G' on a log-log scale (Figure 2.13). While there is some dependence on constituent properties when reduced by a factor of 25 with a slight deviation from a linear slope, the degree of consistency in the results is really quite remarkable. However, when tensegrity is used to predict the magnitude of the modulus, at least in its most simple form:

$$G' \approx \tfrac{1}{3}\tau_0 \tag{2.12}$$

the values are significantly lower, by at least an order of magnitude, than those observed in the simulation.

At prestrains close to zero, the cellular solids model would be the most appropriate, given the lack of thermal effects noted above and the inability of the tensegrity model to capture the modulus of a crosslinked actin network at zero strain. Despite these seeming advantages, however, the moduli predicted by cellular solids are somewhat higher than those calculated in the model. The following equation provides estimates of ~316 Pa [20], about 80-fold higher than that observed in simulation at 1 Hz:

$$G' \approx \tfrac{3}{8} E\Phi^2 \tag{2.13}$$

where $E = 2$ GPa is the Young's modulus of the filaments, and $\Phi = 6.49\times10^{-4}$ is the volume fraction of the filaments. This is likely due to the fact that G' shows a strong dependence on the degree of crosslinking; the cellular solids model, as currently formulated, assumes a maximal degree of crosslinking, and that these crosslinks are rigid. Our model shows that both of these effects can cause a significant increase in modulus. Consequently, while cellular solids would appear to be based on a reasonable physical representation of the system, its lack of these two critical features makes it difficult to use for direct quantitative predictions.

Biopolymer models, as stated earlier, have the advantage that they alone account for thermal fluctuations. However, the results presented here suggest that for conditions corresponding to the cytoskeleton, and for many of the studies of crosslinked actin gels, thermal effects seem to be of relatively little importance. Nonetheless, the shear modulus predicted by this theory [23]:

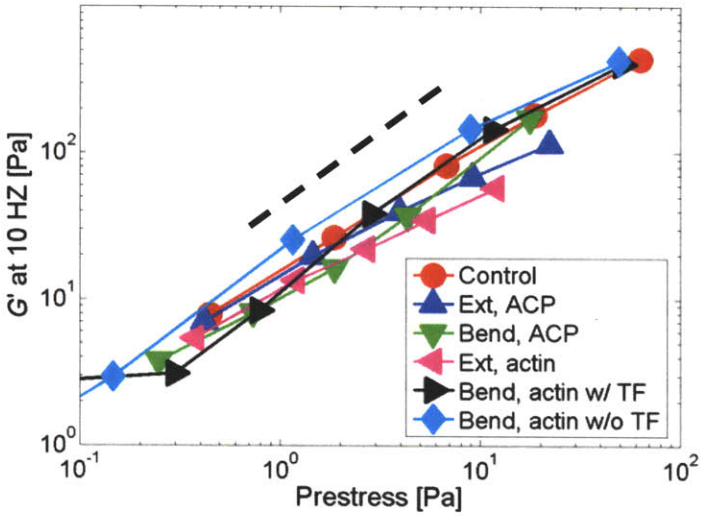

Figure 2.13 Values of shear storage modulus (G') at 10 Hz plotted against prestress (black dashed line has a slope of 1). Red circles: normal stiffnesses, blue triangles: $\kappa_{s,A\,CP}/25$, green inverted triangles: $\kappa_{b,ACP}/25$, magenta left-pointed triangles: $\kappa_{s,A}/25$, black right-pointed triangles: $\kappa_{b,A}/25$ with thermal fluctuation, and cyan diamonds: $\kappa_{b,A}/25$ without thermal fluctuation.

$$G' \approx \frac{\kappa_{b,A} L_{C,A} l_p}{\xi^2 l_c^3} \tag{2.14}$$

where $\kappa_{b,A} = 1.056\times10^{-18}$ Nm, $l_p = 10$ μm, $l_c = 0.393$ μm, $\xi = 0.393$ μm is the mesh length, yields numerical values somewhat closer to observation, ≈ 79 Pa. Moreover, only the biopolymer models have the capability of predicting the frequency scaling of the moduli, and the experimentally observed 0.75 power law behavior at high frequency is accurately captured by these models.

It has been proven that our discrete computational model is very powerful for investigating the rheological behaviors of actin-like networks. The model incorporates most of the minimally essential features: the use of realistic morphology, the explicit existence of ACPs, the consideration of repulsive forces and cross-linker stiffness.

However, one important feature observed in cells and not captured by the current model is the effect of unfolding or unbinding event of crosslinks under high stress. Most ACPs have finite binding lifetimes, leading to dissociation and reformation of crosslinks, which is known to play an important role in the viscoelastic moduli and rheology of actin networks [41,82,83]. However, ACPs in this model do not undergo dynamic rearrangement. This artifact renders the level of stress responding to prestrain unreasonably high. While stress does not diverge beyond 50 Pa in *in vitro* experiments [26,27,36,84], it can increase over 100 Pa in our simulation. The absence of crosslink dynamics causes G' in Figure 2.7a to be much higher and to exhibit a lower power compared to experiments. Nevertheless, our present results provide valuable insights as well as benchmarks whereby stress relaxation or dynamic reorganization of networks can be compared as an extension of this work.

Chapter 3

Studying Effects of Dynamic Behaviors of Actin Crosslinking Proteins on Rheology of Passive Actin Networks

3.1. Introduction

Although the results in Chapter 2 revealed many significant insights into the effects of prestrain and enthalpic/entropic factors on viscoelastic properties of actin networks, it lacked realism in that it failed to reproduce the dynamic behaviors of ACPs: unbinding and unfolding. The two behaviors have been highlighted in numerous recent experiments as potential factors significantly contributing to the rheology of the actin cytoskeleton [45]. Other previous computational approaches [60-62], while instructive, do not incorporate ACP unbinding and unfolding simultaneously. In this chapter, we extend our previous model by including these two events in order to study the roles of unbinding and unfolding events in actin rheology. It was found that in the strain-stiffening regime where a linear shear strain was applied, unbinding of ACPs significantly decreases the magnitude of stress to a reasonable level at high shear strain, whereas unfolding merely delays the increase of stress to higher values of strain. Frequencies of unbinding and unfolding events at a given strain depend strongly on the rate at which the strain was generated. ACPs unbound by greater forces experience larger displacement and tend to rebind to a different filament. In addition, at constant strain, stress relaxes to physiological levels only by unbinding,

consistent with experiments, not by unfolding of ACPs. While only unbinding appears to be important at initial stress relaxation, rebinding also plays a significant role in a low-stress regime. Finally, when the network is allowed to return to an equilibrium position after shearing, plastic deformation, the irreversible reorganization of the network, is observed with unbinding, but not when only unfolding is allowed. All of these observations demonstrate that despite the possibility of unfolding, unbinding should be a dominant mechanism governing the rheology of actin cytoskeleton.

3.2. Methods

3.2.1. Preparation and Rheological Measurement of an Actin Network

We generate a network in the same manner as Chapter 2, crosslinked only by ACP^C that have a filamin-like V-shape and form orthogonal crosslinks between filaments during the polymerization process, meaning that the term "ACP" from now on refers to ACP^C. After growing the network, the same coarse-graining procedure using cylindrical segments is applied to increase length and time scales of subsequent simulations. Filament length (L_f) is 1.5±0.65 μm (average ± standard deviation), and the actin concentration (C_A) is 12.1 μM. The width of a cubical computation domain is 2.8 μm. A geometrically identical network was employed for most measurements to systematically control and isolate the effects of a given parameter. The measurement of viscoelastic moduli of the networks is performed only via bulk rheology in which oscillatory shear strain is applied to the top surface of the simulation box with the bottom surface fixed.

3.2.2. Dynamics and Mechanics

As described in Chapter 2, displacements of actin filaments and ACPs are governed by the Langevin equation, and most of their mechanical properties are characterized by the same bending and extensional stiffnesses, and thermal fluctuations are included. Main differences from the previous model are: 1) the altered extensional behaviors of ACPs to reflect unbinding and unfolding events and 2) steric interactions acting only between actin filaments.

3.2.3. Unfolding Event of ACP

Experimentally, the force-extension curve of filamin A exhibits a saw-tooth behavior with peak values of 100-200 pN at intervals of ~30 nm in response to a pulling force [46]. When the pulling force is released, it relaxes as a single worm-like chain. To describe such behaviors of filamin A, each arm of ACP is described by a series of worm-like chains and can unfold up to N_{uf} times following Bell's equation. Denoting the equilibrium and the current length of one ACP arm respectively by r_0 and r_{12}, the force $F_s(r_{12})$ and unfolding rate k_{uf} are:

$$F_s(r_{12}) = \begin{cases} \dfrac{k_B T}{p}\left[\dfrac{(2l_{0,i} - r_{12} - r_0)(r_{12} - r_0)}{4l_{0,i}^2 (1 - r_{12}/l_{0,i})^2 (1 - r_0/l_{0,i})^2} + \dfrac{r_{12} - r_0}{l_{0,i}}\right] & \text{if } r_{12} \geq r_0 \\ \kappa_{s,ACP}(r_{12} - r_0) & \text{if } r_{12} < r_0 \end{cases} \tag{3.1}$$

$$k_{uf} = \begin{cases} k_{uf}^0 \exp\left(\dfrac{\lambda_{uf} F_s}{k_B T}\right) & \text{if } r_{12} \geq r_0 \\ 0 & \text{if } r_{12} < r_0 \end{cases} \tag{3.2}$$

where p = 0.33 nm is the persistence length, $l_{0,i}$ = (140 + 30×i) nm (i = 0 - N_{uf}) is the maximum extension for the i^{th} unfolding, r_0 = 105 nm, and $\kappa_{s,ACP}$ is the stiffness of ACP

against compression below the equilibrium length r_0. k_{uf}^0 is the zero-force unfolding rate coefficient, and $\lambda_{uf} = 6\times10^{-10}$ m is the mechanical compliance. To study the long-time behavior (see below), in different simulations, we rescale k_{uf}^0 with respect to the reference value, $k_{uf,r}^0 = 3.0\times10^{-5}$ s^{-1}. Values of $k_{uf,r}^0$ and λ_{uf} are set based on previous experiments and Monte Carlo simulations [46]. Each unfolding event increases i by 1 while keeping track of the values of r_{12} where the i^{th} unfolding occurred, $r_{uf,i}$. When r_{12} decreases below $r_{uf,i}$, refolding occurs; i remains fixed during the relaxation phase but decreases by 1 during extension phase. The periods of relaxation and extension are determined by changes in the ACP length during the previous 10 time steps (= 61.7 ns), where a reduction in length for $\geq$ 8 out of 10 steps is considered relaxation. Once relaxation begins, $l_{0,i}$ remains constant. When re-extension begins, $l_{0,i}$ instantly changes to a value corresponding to i satisfying $r_{uf,i-1} \leq r_{12} \leq r_{uf,i}$. This is to capture the behavior observed in AFM experiments

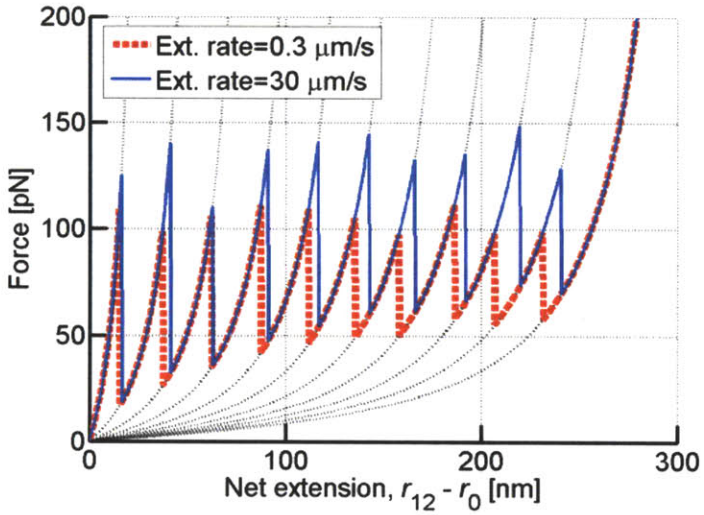

Figure 3.1 Sample force-extension curves of one arm of an ACP with N_{uf} =10. Two extension rates are used: 0.3 μm/s (thick red dashed line) and 30 μm/s (solid blue line). Dotted lines: worm-like chains following Equation 3.1.

[46,85]. Simulations conducted with a single ACP at two extension rates are qualitatively similar to results of AFM measurements (Figure 3.1).

3.2.4. Unbinding Event of ACP

ACP unbinds in a similar manner but with different parameter values:

$$k_{\mathrm{ub}} = \begin{cases} k_{\mathrm{ub}}^{0} \exp\left(\dfrac{\lambda_{\mathrm{ub}} F_{\mathrm{s}}}{k_{\mathrm{B}} T}\right) & \text{if } r_{12} \geq r_{0} \\ k_{\mathrm{ub}}^{0} & \text{if } r_{12} < r_{0} \end{cases} \tag{3.3}$$

where k_{ub}^{0} is the zero-force unbinding rate coefficient, and $\lambda_{\mathrm{ub}} = 1.04\times10^{-10}$ m is the mechanical compliance of the bond for unbinding. The reference value of $k_{\mathrm{ub,r}}^{0} = 0.115\ \mathrm{s}^{-1}$ is taken from experiment [45]. In our model, simultaneous unbinding of both ACP arms is prohibited to preclude extensive calculations for diffusion of cylindrical arms of free ACPs. We also assume that if an unbinding event occurs on an ACP arm, it completely refolds, and r_{12} immediately restores to its equilibrium value, $r_0\,(i = 0)$. Once unbound, the arm of an ACP thermally fluctuates until it rebinds.

3.2.5. Mimicry of Long-time Rheology

In typical experiments, stress relaxation occurs over a time scale longer than seconds [4] which we address in our simulation by employing the following scaling argument. Based on the expectation that network dynamics is governed mainly by the rates of unfolding and unbinding of ACPs, longer-time behaviors may be captured by adjusting the zero-force rate coefficients, k_{ub}^{0} and k_{uf}^{0} that we collectively denote as k^{0}. By scaling time by $(k^{0})^{-1}$, certain types of time-dependent behaviors could be reduced to a single universal curve. This allows us to predict behaviors at much longer times simply

by increasing k_{ub}^0 and k_{uf}^0 and scaling time accordingly. We examined this hypothesis by either increasing shear strain linearly with time (Figure 3.2a), or monitoring stress relaxation under constant strain (Figure 3.2b). Denoting the time over which the shear strain is applied in the first case and that during which stress relaxation is measured in the second as τ, all cases with the same values of $k^0\tau$ exhibit similar rheological behaviors.

3.2.6. Simulation of a Micro-bead Experiment

To verify the roles of unbinding event of ACPs, we performed a simulation mimicking experiments where a micro-bead is pulled in unidirection by an optical tweezer. For using a micro-bead with the size comparable to the experiments, we prepared a larger network whose domain is 5 μm with C_A = 12 μM , $< L_f >$ ~1.5 μm, and R_{ACP} = 0.017. After polymerization, all actin filaments are severed and clamped at the upper and lower

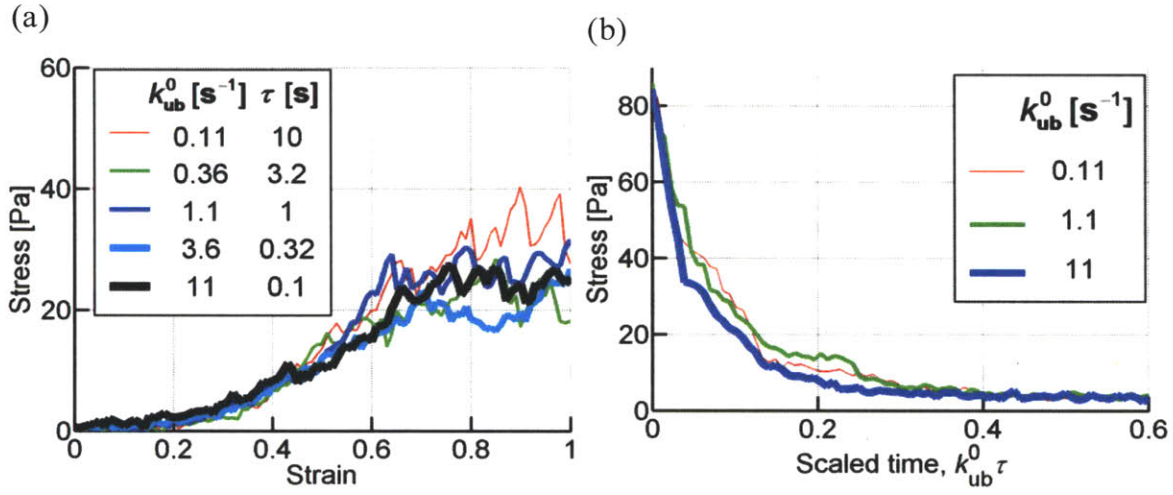

Figure 3.2 Invariance of rheological behaviors with $k_{ub}^0\,\tau$ fixed, which enables to mimic long-time rheology. (a) Five curves representing strain-stiffening of actin networks correspond to each other well despite different strain rates. (b) Three curves representing stress relaxation also show a dramatic match.

boundaries (z-surfaces), and periodic boundary conditions are imposed on all other boundaries (x- and y-surfaces). A micro-bead whose diameter is 1.2 μm is then inserted into the actin network by replacing all filaments within a central spherical region with a rigid sphere. To simulate the network experiments, the microbead is forced to move in +x direction with the constant rate of 20 μm/s. Only interaction acting between actin networks and the micro-bead is a volume-exclusion effect. During the simulation, only unbinding of ACP is allowed. Both the sum of forces acting on the microbead in x-direction and the state of each ACP (bound or unbound) are recorded as functions of bead displacement.

3.2.7. Parallelization of Computational Codes

From this study, the computational codes are parallelized using the Message Passing Interface (MPI) in order to reach larger length and time scales. Since our computational model has no long-range interaction such as electrostatic force, the best strategy for parallelization is spatial domain decomposition with subdomain load balancing (Figure 3.3a); in calculation using P processors, a whole domain is initially divided to P equal-sized subdomains, followed by the distribution of particles based on their location. At every time step, all information of particles located within 200 nm from boundaries is transferred to adjacent subdomains for synchronization required for calculation of forces. Each CPU performs computations for only particles belonging to its own subdomain. Also, at every certain time steps, location of boundaries sectioning subdomains is adjusted, so that each CPU bears as similar loads as possible. We have evaluated the increase in computational efficiency of simulations containing about 9,000 particles, depending on the

number of CPUs (Figure 3.3b). The computational time required for a 0.1 s simulation was determined for seven cases, each with a different number of CPUs assigned. Relative efficiency, the ratio of time with 1 CPU to time with P CPUs, appears to be a power function of P:

$$\text{Relative efficiency} \sim P^{0.715} \tag{3.4}$$

A primary reason preventing the efficiency from increasing linearly with P is that with the domain of the same size, using more CPUs leads to smaller subdomains, with the consequence that the fraction of particles transferred to neighboring subdomains for synchronization grows. Intrinsically, communication between CPUs is a time-consuming

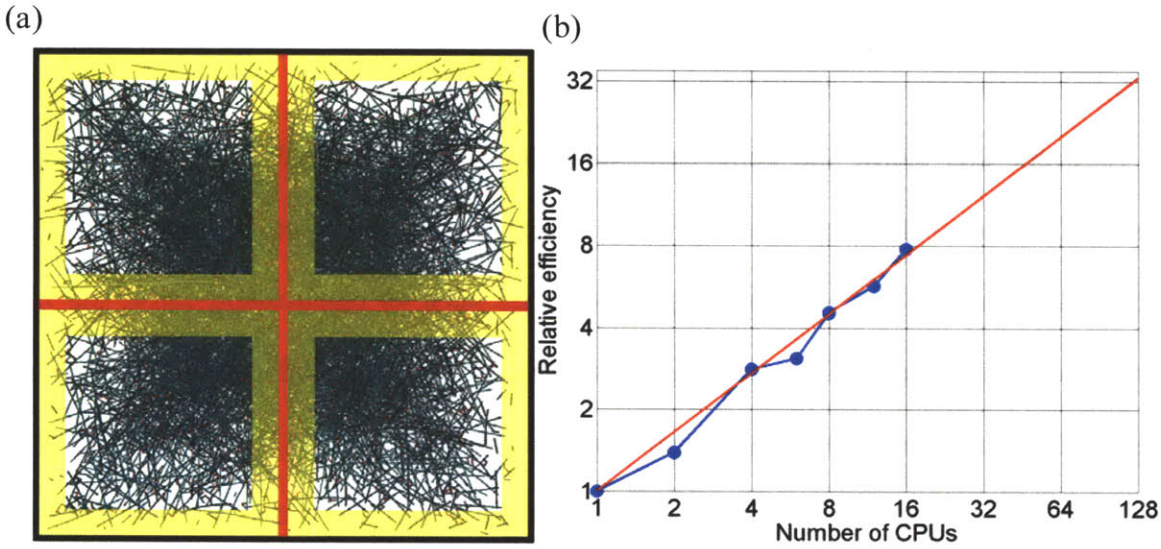

Figure 3.3 Parallelization of computational codes. (a) A schematic diagram showing spatial domain decomposition with subdomain load balancing. In this example, the domain with periodic boundary condition is initially divided into four subdomains by red lines. Information of particles located in yellow regions whose thickness is 200 nm is transferred to neighboring subdomains for synchronization every time step. Positions of red lines are adjusted at a certain time interval to maintain the number of particles in each subdomain at similar levels. (b) Relative efficiency depending on the number of assigned CPUs. Blue indicates measurements in seven cases, and red corresponds to $\sim P^{0.715}$.

process, and therefore the increased amount of communication impairs the efficiency. It was confirmed that with a larger computational domain, the exponent of 0.715 became greater, indicating that the parallelization is more efficient for larger domains.

3.3. Results

3.3.1. Strain-stiffening

With this model, we first investigated strain-stiffening. A constant shear strain rate is applied to the actin network ($\dot{\gamma}$=10 s^{-1}) with both unbinding and unfolding of ACPs, and the corresponding shear stress is computed. Five different values for the zero-force rates coefficients are used ($k_{ub}^0 / k_{ub,r}^0 = k_{uf}^0 / k_{uf,r}^0 = n$; n=1-100), each leading to a different effective shear strain rate $\dot{\gamma}_{eff} = \dot{\gamma} / n$ based on scaling arguments above. The frequencies of unbinding and unfolding events strongly depend on $\dot{\gamma}_{eff}$ (Figure 3.4a): at small $\dot{\gamma}_{eff}$ (< 1 s^{-1}), unbinding events dominate, whereas at large $\dot{\gamma}_{eff}$ (> 1 s^{-1}), unfolding does. Importantly, under typical physiological and experimental conditions ($\dot{\gamma}_{eff}$ < 1 s^{-1}), unbinding/rebinding dominates with negligible effects due to unfolding/refolding. The overall shape of the stress-strain curves (Figure 3.4b) is consistent with experiments [26,27]. When unfolding prevails at the highest $\dot{\gamma}_{eff}$, the stress level steadily increases. In contrast, when unbinding dominates, stress collapses at a level similar to experimental values. Critical stress at which stress begins to deviate from the control case appears to be proportional to $\dot{\gamma}_{eff}$, $\tau_c \sim \dot{\gamma}_{eff}^{0.7}$ (Figure 3.4c). From the measurement of forces acting on ACPs, we found that unfolding leads to relatively uniform distribution of external load on

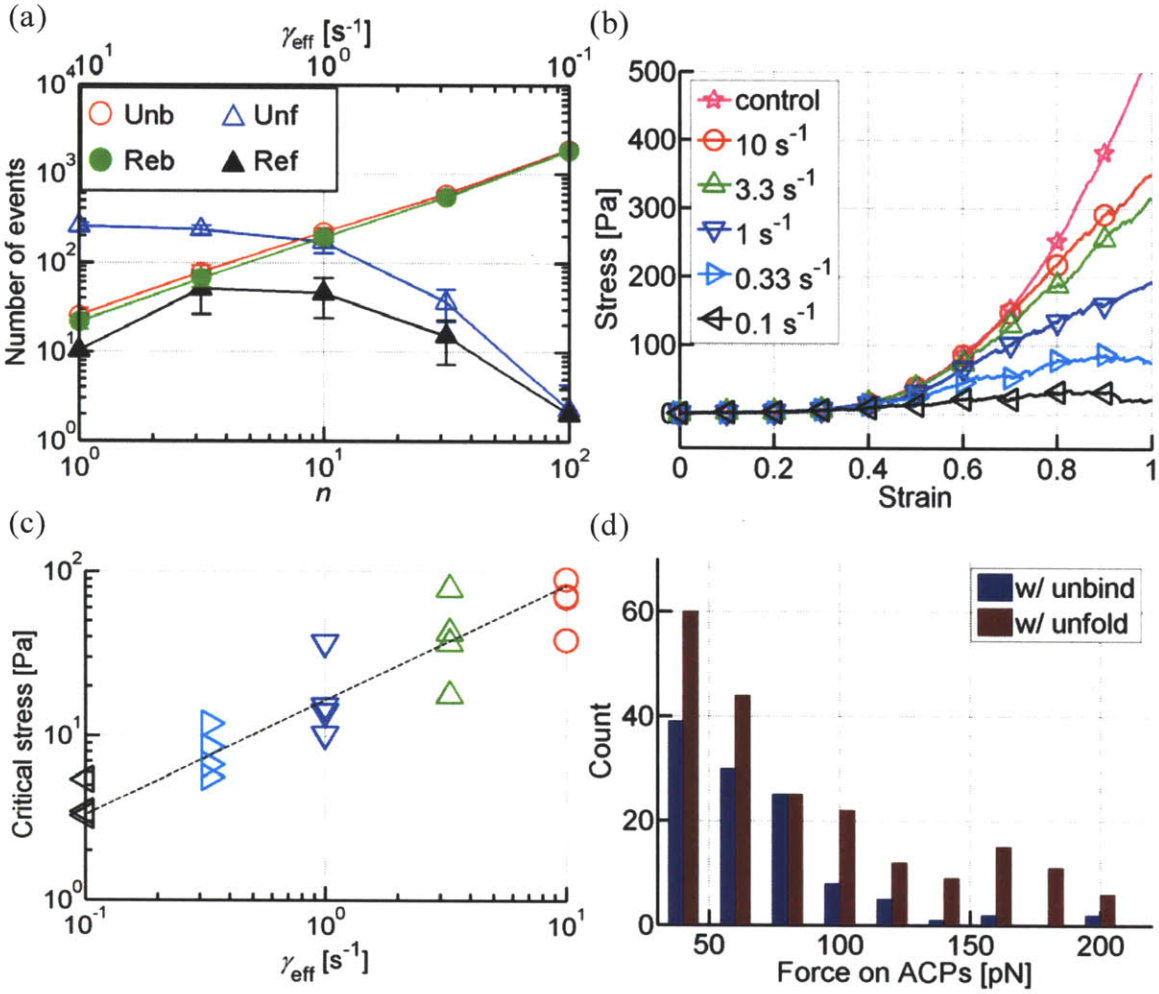

Figure 3.4 Strain-stiffening behaviors with unbinding and unfolding. (a) The frequency of four events depending on n ($=k_{ub}^0/k_{ub,r}^0=k_{uf}^0/k_{uf,r}^0$) with $\dot{\gamma}=10$ s^{-1}. $\dot{\gamma}_{eff}=\dot{\gamma}/n$ on the top horizontal axis indicates the effective shear strain rate (see text). With small n, unfolding events are predominant with a noticeable difference between the frequencies of unfolding and refolding, whereas with large n, unbinding and rebinding dominate to similar extent. (b) Stress-strain behaviors with different $\dot{\gamma}_{eff}$. When unfolding is prevalent, stress is merely delayed without manifest drop. By contrast, the dominance of unbinding leads to the catastrophic reduction of stress to a level observed in experiments, ~10 Pa. (c) Critical stress (τ_c) at which stress starts deviating from the control case in Figure 3.4b, depending on $\dot{\gamma}_{eff}$. For each $\dot{\gamma}_{eff}$, τ_c from four simulations are plotted using the same colors and symbols as Figure 3.4b. A black dashed line indicates $\tau_c \sim \dot{\gamma}_{eff}^{0.7}$. (d) Distributions of forces acting on ACPs with either unbinding (blue) or unfolding (dark brown) at $\gamma=1$.

an entire network, enabling the network to bear high external load with relatively low load on each component (Figure 3.4d). On the other hand, unbinding appears to substantially decrease the fraction of the network with high load, resulting in the dissipation of high load. However, even after a large number of unbinding events, the highest load is still supported by a small portion of the network. These different force distributions that unbinding and unfolding events induce are consistent in a previous computational study [60] and can explain both the steady increase of the shear stress in unfolding-dominant cases and the marked reduction in unbinding-dominant cases. Considering that strain rates are hardly larger than 1 s^{-1} in biological systems, rheological behaviors seen in typical *in vivo* and *in vitro* conditions are likely governed by ACP unbinding although unfolding may occur [46].

To further examine how unbinding and subsequent rebinding of ACPs reduce stress, we quantified the displacement between unbinding and rebinding of ACPs (Figure 3.5a). The amount of displacement resulting from a change in linear shear strain in +x-direction applied while the ACP remains in a free state was subtracted to compute net displacement. ACPs unbound with larger forces tend to be displaced more. We also traced whether or not unbound ACPs rebind to the same filament (Figure 3.5a). We assign a turnover value of 1 for ACPs that reattach to a different filament, and 0 for those rebinding to the same filament. Above 20 pN, nearly all unbound ACPs rebind to different actin filaments. In addition, the displacement or turnover of ACPs is measured depending on prestrain level (Figure 3.5b,c). In Figure 3.5b, ACPs unbound at higher prestrain have tendency to experience larger displacement and rebind to a different filament. Figure 3.5c shows that trivial unbinding with negligible displacement occurs at all prestrain, but significant one accompanied by large displacement happens more often at greater prestrain. Large

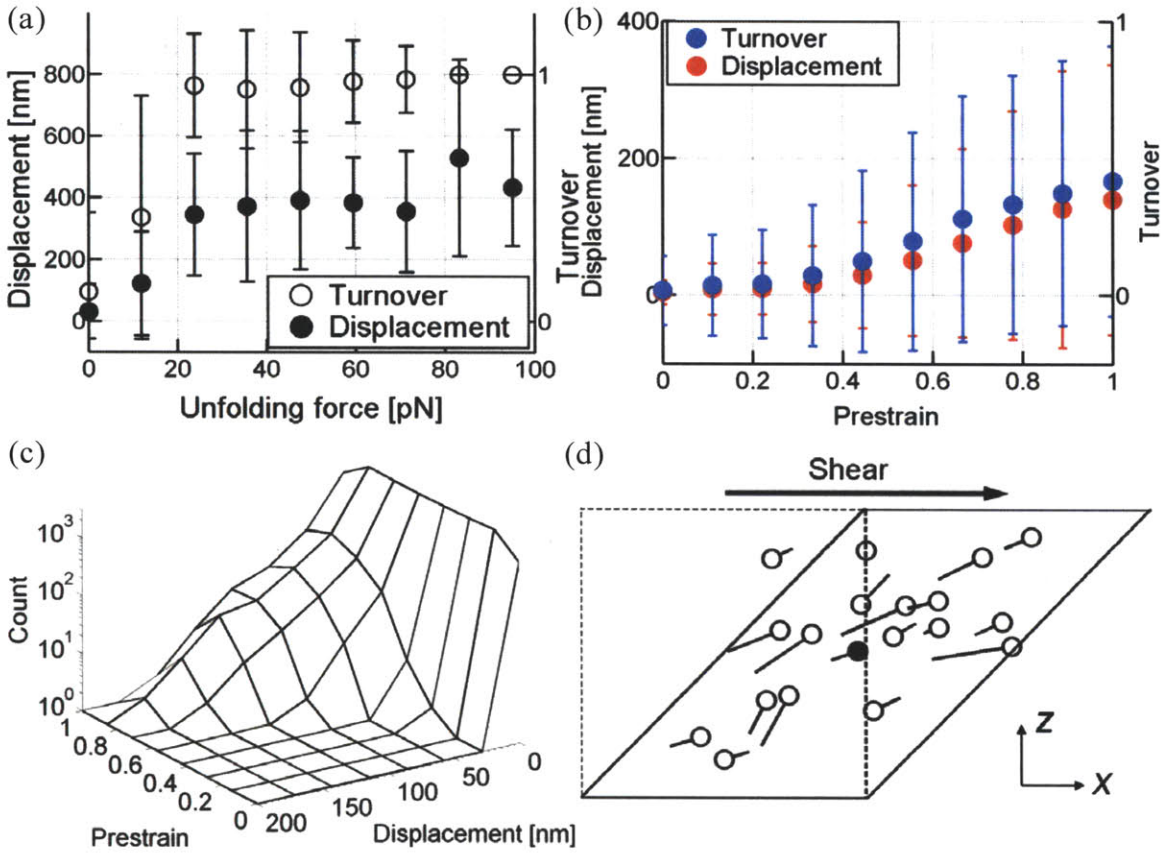

Figure 3.5 Displacement and turnover of ACPs during strain-stiffening with unbinding. (a) Displacement of ACP between unbinding and rebinding (solid circles), and the average turnover indicating whether or not unbound ACP rebinds to the same filament after unbinding (open circles). The turnover value of one or zero respectively indicates rebinding to a different or the same filament. ACPs unbound with larger forces tend to rebind to different filaments after large displacements. (b) Averaged displacement (red) and turnover (blue) of ACPs depending on prestrain at which ACPs unbind. ACPs unbound at higher prestrain level tend to be displaced more and rebind to a different filament. (c) Detailed distribution of ACP displacements at each prestrain. Unlike trivial unbinding with negligible displacement, significant one occurs more often at higher prestrain. (d) An example showing displacement and turnover of ACPs unbound with more than 20 pN during shearing of the domain from $\gamma = 0$ (dashed line) to $\gamma = 1$ (solid line). On the x-z plane, lines are drawn between unbinding and rebinding locations, with the latter indicated by symbols: Open (solid) circles denote rebinding to different (same) filaments.

unbinding force should be associated with high prestrain, and thus the tendency in Figure 3.5b,c is consistent with that in Figure 3.5a. Figure 3.5d shows one example of the displacement and turnover of ACPs unbound with ≥ 20 pN, demonstrating that ACPs tend to rebind to a different filament following a diagonal displacement. In fact, highly loaded ACPs unbind mostly from a small fraction of the actin network termed the 'supportive framework' that bears most of the load in Chapter 2. We found that ~85% of all ACPs that ruptured with ≥ 20 pN belong to the supportive framework which constitutes only 25% of the entire network. Immediately after unbinding of such stretched ACPs, the filaments where the ACPs were originally attached undergo rapid reconfiguration to relieve the load, and thus they are unlikely to remain close to the original ACPs. A cascade of such events will lead to reconfiguration of the network and reduction in stress to levels observed in experiments, ~10 Pa.

3.3.2 Stress Relaxation

We next studied stress relaxation. A steady shear strain was first applied to γ = 0.6 with neither unbinding nor unfolding, followed by holding γ constant for 5 s with either unbinding ($10k^0_{\mathrm{ub,r}}$) or unfolding ($10k^0_{\mathrm{uf,r}}$) (Figure 3.6a). Unfolding induces little stress relaxation regardless of refolding, whereas unbinding results in substantial stress relaxation. In the case when both ACP unbinding and rebinding are allowed, stress tends to relax to a finite nonzero value. Without rebinding, while stress relaxation until ~1 s is similar to the case with rebinding, later it continues to decrease. When stress relaxation curves are fitted to a local power law (Figure 3.6a),

$$\tau(t) \sim t^{-x} \tag{3.5}$$

the exponent x varies between 1 and 4 in the case without rebinding, and between 0.5 and 1 with rebinding. Thus, unbinding primarily governs stress relaxation at high stress levels, but rebinding becomes significant at low stresses by reconfiguring the network so that it can resist low levels of stress and slow down stress relaxation. Compared to an experiment [4] where stress relaxation of reconstituted actin networks crosslinked by filamin was evaluated, our value of x is too high. However, the initial stress in this relaxation experiment was less than 5 Pa, suggesting that the system is in a regime where rebinding is more significant. To test this, we measured stress relaxation of the network sheared to $\gamma = 0.12$ with rebinding (data not shown). Stress relaxed from ~1 Pa with $x <$ 0.2, which is more consistent with [4]. A similar behavior would be observed if we initially shear the system with unbinding of ACPs allowed.

It is apparent that stress in the case with rebinding would eventually drop close to zero after long time since the network has no external energy input. However, for *in vivo* cells, molecular motors will supply the energy that can maintain stress at a relatively constant level, which explains why stress in cells does not converge to zero during relaxation and has a quite large relaxation time in a long-time regime, ~20 s, in [86].

In addition, we picked network structures at t = 0, 0.1, 0.2, and 0.3 from a case with both unbinding and rebinding, measuring their G' and G'' with no unbinding for studying a change in viscoelastic moduli induced by stress relaxation. As seen in Figure 3.6b, with more stress relaxation, the magnitude of G' significantly decreases, but its power law exponent slightly increases. The change in G' with relaxation explains a discrepancy between G' of prestrained networks in the previous study [66] and that in experiments [84]. Also, it implies that the weak power-law behavior of G' despite quite high magnitude in

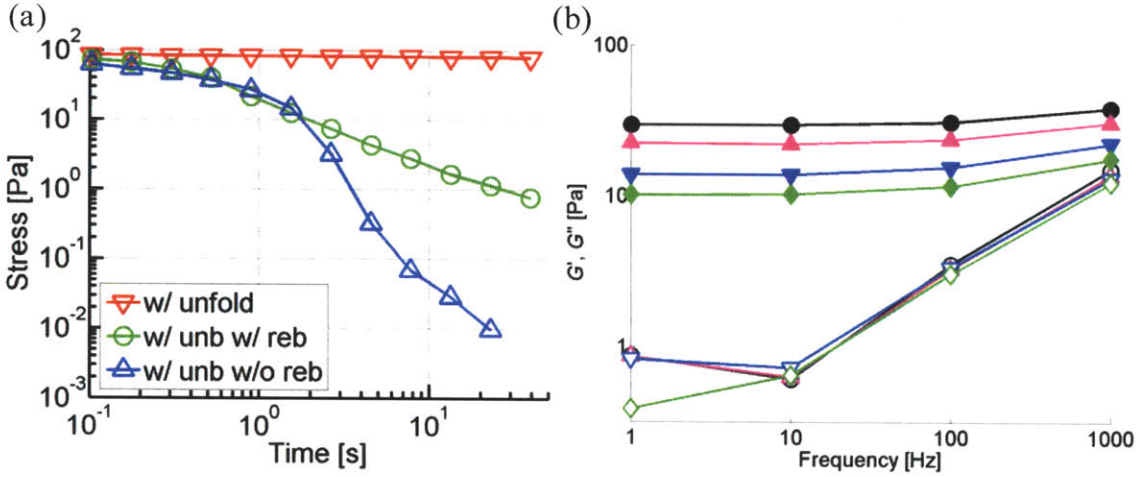

Figure 3.6 Stress relaxation due to unbinding or unfolding. (a) Stress relaxation caused by unbinding with (green) and without rebinding (blue) and by unfolding (red). Time is multiplied by 10, to be consistent with scaling of unbinding/unfolding rates. Regardless of rebinding, green and blue curves are similar at $t < \sim 1$ s. However, rebinding event plays a significant role by preventing the stress from quickly converging to zero. By contrast, the stress with unfolding remains at a relatively constant value, meaning negligible stress relaxation. (b) G' (solid symbols) and G'' (open symbols) of networks that were extracted at $t = 0$ (black circles), 0.1 (magenta triangles), 0.2 (blue inverted triangles), and 0.3 (green diamonds) from stress relaxation measurement with both unbinding and rebinding. The moduli were measured with neither unbinding nor rebinding. With more stress relaxation, G' has lower magnitude and slightly greater slope, corresponding well to observations in experiments [84].

cells [44] might be attributable to the dynamic properties of ACPs. In addition, an interesting behavior that G'' increases at low frequency that we found in the previous study disappears after substantial stress relaxation, meaning that the behavior is somewhat artificial due to the absence of unbinding.

3.3.3 Plastic Deformation

To study plastic deformation of the network, we applied a constant shear strain rate ($\dot{\gamma}_{eff}$ = 10, 1, or 0.1 s^{-1}) up to γ = 1.0 with unbinding/rebinding or unfolding/refolding. The top boundary was then allowed to freely relax (Figure 3.7a). With unbinding and high $\dot{\gamma}_{eff}$, γ returns close to its initial value (γ = 0). However, with unbinding and low $\dot{\gamma}_{eff}$, γ decays more slowly until 0.01 s, and later the rate of relaxation decreases to a level similar to high $\dot{\gamma}_{eff}$, implying that γ may asymptote to a nonzero value. By contrast, in all cases with unfolding, γ rapidly returns close to zero. The difference between unbinding and unfolding can also be seen from displacements of ACPs between their original positions and those at t = 2 s (Figure 3.7b). In cases with unfolding only, averaged displacements of ACPs are similar to the control case with neither unbinding nor unfolding while unbinding with lower $\dot{\gamma}_{eff}$ results in larger average displacements, indicating a higher degree of network reorganization. It is useful to compare the local power exponent in $\gamma \sim t^{-x}$ to experimental data. Cases with unbinding events have relatively consistent values, x=0-0.4. Especially, the case with $\dot{\gamma}_{eff}$ = 0.1 s^{-1} corresponds to typical experimental conditions in terms of $\dot{\gamma}_{eff}$ and τ (t = 0) = 20 Pa. Its exponent is less than 0.2, in good agreement with the *in vitro* value, ~0.17 [27]. The amount of plastic deformation in [27], where γ falls from the initial value of 0.08 to about 0.02, might have been greater if the reconstituted actin network had been sheared to a greater strain. These observations in the simulations implicate that although the power-law exponent could be greater than 0.2, the unbinding event with physiologically and experimentally reasonable shear rates prevents stress from increasing to very high level, keeping the power-law exponent lower than 0.2. Therefore, irreversible deformation

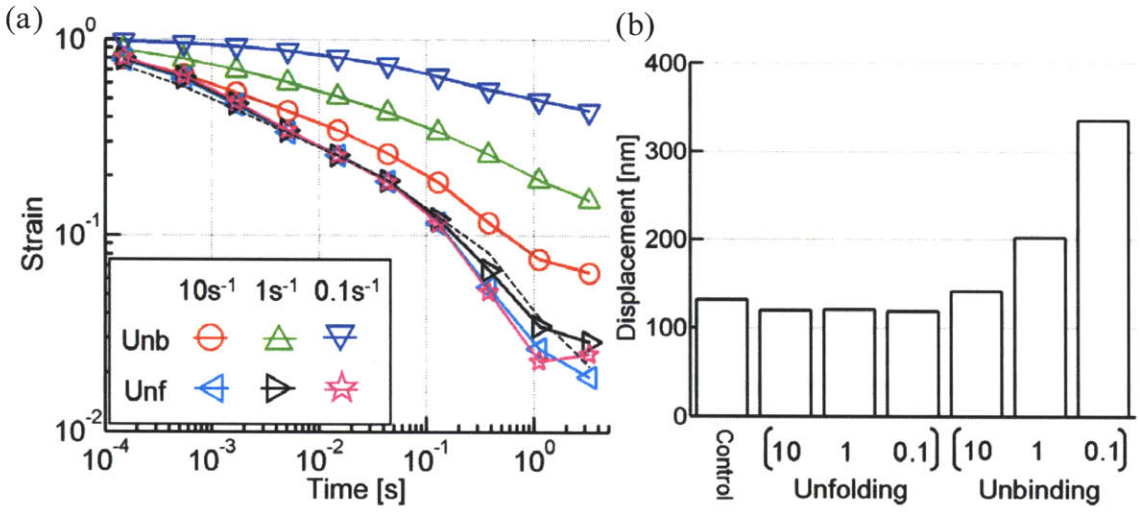

Figure 3.7 Irreversible deformation of actin networks with unbinding or unfolding. (a) Log-log plot of shear strain (γ) profiles. The top surface of the computational domain was sheared up to γ = 1.0 with different $\dot{\gamma}_{\text{eff}}$ (legend), and was released. The dashed line indicates the control case with neither unbinding nor unfolding. A case with unbinding and $\dot{\gamma}_{\text{eff}}$ = 10 (red) exhibits instantaneous retreat near to an initial location, γ = 0, contrasting to other cases with unbinding where γ reduces much slower at the initial stage. Unlike unbinding, all cases with unfolding show an identical behavior that γ rapidly decreases close to zero, which is quite analogous to the behavior of a case with neither unbinding nor unfolding. (b) Average displacements of ACPs between the original network and the network at t = 2 s in (a). The numbers on the x-axis represent $\dot{\gamma}_{\text{eff}}$ in each case. Unfolding causes few differences in comparison to the control case. By contrast, with more unbinding events, the averaged differences become larger, meaning substantial network reorganization.

observed in experiments is attributable to unbinding rather than unfolding, supporting that the unbinding event is of more importance than unfolding in physiological and experimental phenomena.

3.3.4 Micro-bead Rheology

(with the help of Dr. Hyungsuk Lee. Most contents in this section are adapted from one of my publications [87].)

To substantiate the importance of unbinding of ACPs in the mechanical response of actin networks, we also simulate a micro-bead experiment (Figure 3.8a). As can be seen in Figure 3.8b, the response measured in the simulation is qualitatively similar to those in Figure 3.8c: an increase in the force and the existence of multiple transitions when the force drops abruptly. During bead displacement, a number of ACP unbinding events occur (red circles on the curve), but most appear to be insignificant in that they are not reflected by any noticeable change in the force curve, except for two cases. In order to isolate the critical unbinding events, we apply two criteria: (1) the distance between the ACP and the surface of the microbead at the moment of unbinding must be < 500 nm, and (2) the ACP must lie within a cone centered on the +x-axis with an included angle of $2\pi / 3$. Only three rupture events meet these criteria (blue circles). Two of these correspond to the sudden transitions of the mechanical response though one occurs early in the simulations and seems irrelevant. This implies that the multiple transitions observed in the experiment can be attributable to the unbinding of ACPs in close proximity to the microbead.

3.4. Discussion

In this study, we evaluated the relative significance of unbinding and unfolding events of ACPs by simulating three rheological behaviors – strain-stiffening, stress relaxation, and plastic deformation – with unbinding and unfolding. In all cases, the

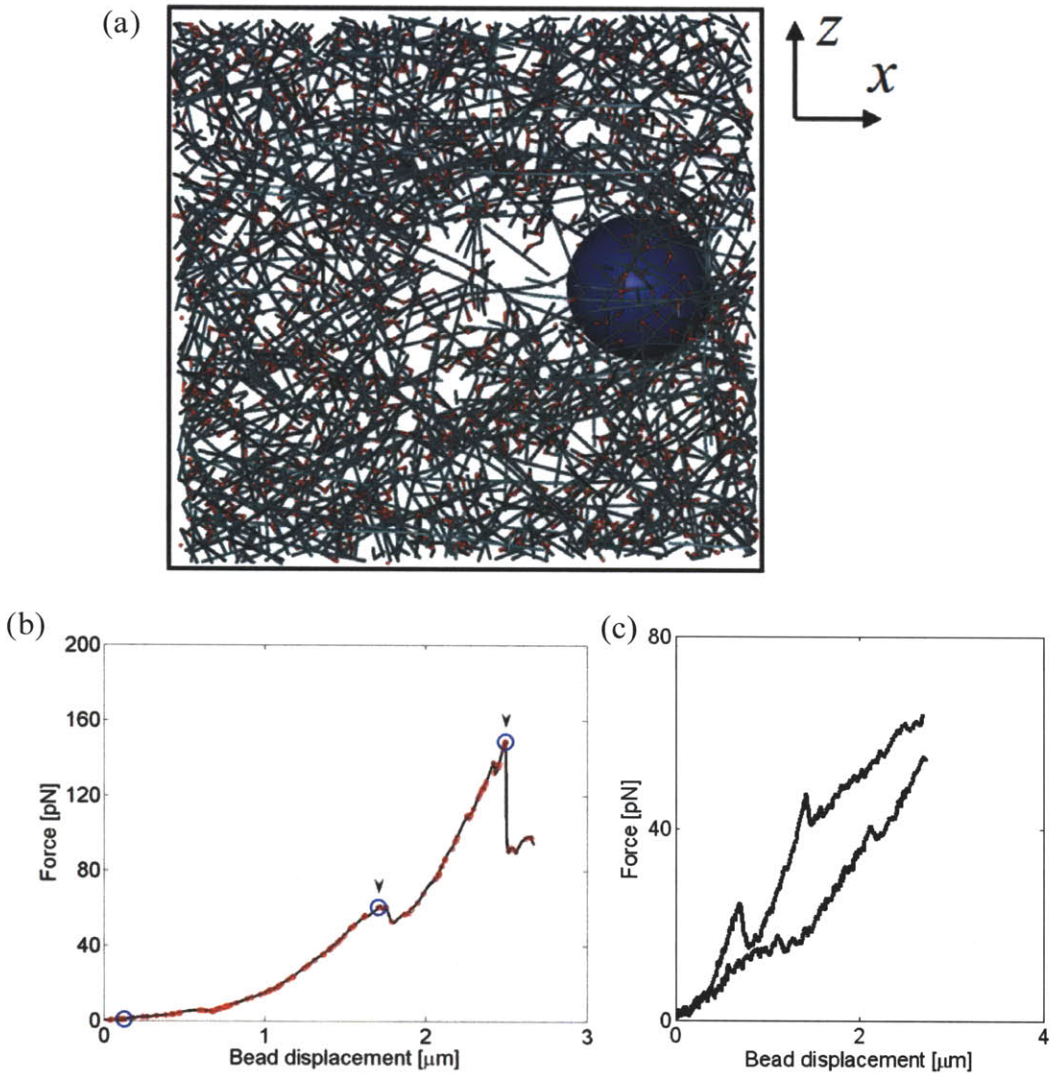

Figure 3.8 Simulation of a micro-bead experiment. (a) The network consisting of actin filaments (cyan) and ACPs (red) with a microbead (blue) at a bead displacement of 2 μm. (b) Mechanical response of an actin network with a micro-bead, simulated by a computational model. Red circles show all ACP unbinding events, and blue circles show only those satisfying the two criteria described in the text. The force acting on the microbead rises with increased bead displacement, and two abrupt drops (arrow heads) in the force are evident. (c) The same type of data from a micro-bead experiment with C_A = 10 μM, $< L_f > = 5$ μm, and $R_{ACP} = 0.01$ [87].

behaviors observed in *in vivo* and *in vitro* experiments appeared only with unbinding of ACPs, implying that the unbinding event is a predominant mechanism governing the rheological behaviors of actin networks under physiological and experimental conditions. With unfolding only, the topology of the network does not change, so the system is unable to adapt to the changes in the loading condition. Unbinding of ACPs allows reconfiguration of the supportive framework, the main core of the network responsible for the elastic response [65]. Nevertheless, the functional importance of ACP unfolding cannot be ignored. It may assist transient deformation of the actin network, and unfolding of an ACP domain may also have a signaling role. Experiments with, *e.g.,* mutant filamin where domain unfolding is prevented by disulfide bridges may help to clarify our present results.

We have shown the predominance of unbinding using a computational model incorporating filamin-like ACPs with both unbinding and unfolding events. Including the effects of motor proteins and cell membranes in the present type simulations would help to better understand the rich diversity of cellular phenomena.

Chapter 4

Investigating Roles of Molecular Motors in the Morphology and Rheology of Active Actin Networks

4.1. Introduction

Self-organization of biopolymer filaments (e.g. actin filaments and microtubules) and molecular motors (e.g. myosin and kinesin) has been highlighted since they are crucial components for cellular life [63]. Several experiments showed that they can be organized into a wide range of distinct structures via the contractile actions of motors [88,89]. One of the most interesting structures is a stress fiber, which is a contractile actomyosin bundle consisting of relatively short actin filaments crosslinked by various proteins, e.g., α-actinin and myosin [90]. Stress fibers play a significant role in determining the viscoelastic properties of cells and vary in their prevalence and orientation as a function of the stresses experienced by a cell and the nature of the substrate to which the cell is attached. Despite previous theoretical [91] and computational studies [63,64], a clear understanding of the morphology of active networks and the assembly mechanisms of stress fibers is still lacking.

In *in vitro* experiments using reconstituted gels composed of actin and passive actin binding proteins such as filamin, the gels exhibited G' comparable to cells only when they were prestrained or prestressed [27]. However, cells are capable of exhibiting high stiffness without such external stimuli, and this has been attributed to contractile action of

molecular motors [18]. Recently, it was shown that reconstituted solutions with actin, filamin, and myosin II could exhibit a stiffness similar to that of cells [18]. Thus, it has been believed to truly capture the rheological properties of the cytoskeleton, it would be necessary to include active molecular motors.

Our previous computational study in Chapter 3, while it allows for dynamic crosslinks, lacks active motors. Here, we extend our previous model by including a motor mimicking myosin minifilaments consisting of many myosin II molecules in order to investigate the morphology and rheology of active actin networks. Motors transformed the actin networks, increasing their stiffness to a degree depending on the concentration and processivity of motors, and resulting in a more heterogeneous distribution of actin filaments. ACPs help the motors to enhance the elasticity by increasing percolation but also obstruct the motors by occupying binding sites of actin segments. In contrast to motors, ACPs prevent networks from becoming heterogeneous. The effects of kinetic parameters of motor walking and ACP unbinding on viscoelastic moduli appear to be negligible in comparison with that of motor unbinding. Network morphology is also highly dependent on boundary conditions, with the formation of sheets or fibers under various conditions.

4.2. Methods

4.2.1. Preparation and Rheological Measurement of an Active Actin Network

An active actin network with motors is generated in a similar manner used in Chapters 2 and 3. After generating the network orthogonally crosslinked by ACPs, a portion of ACPs are transformed to motors based on the concentrations of ACPs (C_{ACP}) and

motors (C_M). Consequently, the specific dimensions of the motors is not mimicked, only the general behavior of a network with active, contractile crosslinkers. In all networks, the average filament length, $<L_f>$, is about 1.5 μm, and C_A is 12 μM, and we prepared both small and large networks in cubical domains whose width is 2.8 μm and 5.0 μm respectively. Rheological properties of the active networks including G' and G'' are measured via the bulk rheology technique described in Section 3.2.1.

4.2.2. Mechanics of Actin Filaments, ACPs, and Motors

Mechanics of actin filaments, ACPs, and motors is governed by extension and bending potentials, denoted by subscripts "s" and "b" respectively:

$$U_s(r) = \begin{cases} \dfrac{k_B T}{p}\left[\dfrac{l_0}{4(1-r/l_0)} - \dfrac{r}{4(1-r_0/l_0)^2} + \dfrac{(r-r_0)^2}{2l_0}\right] & \text{if ACP and } r \geq r_0 \\ \dfrac{1}{2}\kappa_s (r-r_0)^2 & \text{else} \end{cases} \tag{4.1}$$

$$U_b(\theta) = \frac{1}{2}\kappa_b (\theta - \theta_0)^2 \tag{4.2}$$

where $p = 3.3\times10^{-10}$ m is taken to be the persistence length of an ACP, $l_0 = 1.4\times10^{-7}$ m is the maximum extension of ACP, r is bond length, κ_s is extensional stiffness, θ is bending angle, κ_b is bending stiffness, and the subscript 0 denotes an equilibrium value. Note that only the extension of the filamin-like ACPs beyond r_0 follows a shifted worm-like chain model [46]. Arms of ACPs do not unfold as modeled in Chapter 3 since we demonstrated there that only unbinding of ACPs plays a dominant role under physiological and experimental conditions. All other extensional behaviors are governed by a linear spring model. As in our previous studies in Chapters 2 and 3, bending stiffnesses are introduced to restrict actin

filament bending ($\kappa_{b,A}$), maintain the equilibrium angle between two arms of an ACP ($\kappa_{b,ACP,1}$) or motor ($\kappa_{b,M,1}$), and sustain the right angle between the axis of a filament and the arm of an ACP ($\kappa_{b,ACP,2}$) or motor ($\kappa_{b,M,2}$). Values of r_0, κ_s, θ_0, and κ_b for actin and ACP are as specified in Chapter 2 and 3. $r_{0,M}$ and $\theta_{0,M}$ are the same as those of ACP due to geometric correspondence mentioned above. $\kappa_{s,M} = 4.5\times10^{-4}$ pN/nm is based on a previous experiment [92], whereas $\kappa_{b,M,1} = 1.0\times10^{-18}$ Nm and $\kappa_{s,M,2} = 4.1\times10^{-20}$ Nm are arbitrarily determined due to lack of experimental data. In addition, as in previous models, actin filaments experience thermal fluctuation and volume-exclusion effects.

4.2.3. Dynamic Behaviors of Motors

Motors walk on actin filaments toward a barbed end at a rate, k_w, that depends on a extensional force, $\vec{F}_s = \nabla U_s$, acting on their arms (Figure 4.1a):

$$k_w\left(\vec{F}_s\right) = \begin{cases} \dfrac{3.6\times10^{-8}/r_{0,A}}{d_{w,D}\exp\left[\dfrac{\left(\vec{F}_s\cdot\vec{t}\right)\lambda_{w,D}}{k_BT}\right] + d_{w,C} + d_{w,i}\exp\left[\dfrac{\left(\vec{F}_s\cdot\vec{t}\right)\lambda_{w,i}}{k_BT}\right]} & \text{if } r \ge r_0 \text{ and } \vec{F}_s\cdot\vec{t} \ge 0 \\ \dfrac{3.6\times10^{-8}/r_{0,A}}{d_{w,D} + d_{w,C} + d_{w,i}\exp} & \text{else} \end{cases} \quad [s^{-1}] \qquad (4.3)$$

where $d_{w,D}$= 1.1×10^{-3} s, $d_{w,C}$= 8.0×10^{-2} s, $d_{w,i}$= 5.9×10^{-3} s, $\lambda_{w,D}$= 1.3×10^{-8} m, $\lambda_{w,i}$= 2.2×10^{-9} m [93], $r_{0,A}$ = 70 nm, and $\vec{t}$ is a unit vector tangential to an actin segment toward a pointed end. Although motors in this study mimic a myosin minifilament consisting of numerous myosin II molecules, Equation 4.3 and the values of d_w's and λ_w's are adopted from a single-molecule experiment examining myosin V under 1 mM ATP [93] since a precise analytical model for describing the walking rate of a minifilament is not well-known due to both difficulty in measurements and the dependence of the walking rate on

the number of myosin heads involved with walking action [94]. Nevertheless, the load-dependent walking rate of the minifilament measured in [95] is still qualitatively similar to that of myosin V, justifying the use of Equation 4.3 for roughly mimicking myosin minifilament. Although a motor is assumed in this model to be composed of two arms (Figure 4.1a), we take this to correspond to a single myosin minifilament consisting of many myosin II molecules since the minifilament still walks between only two actin filaments. As seen in Equation 4.3 and Figure 4.1b, only tension ($r \geq r_0$) directed to a pointed end ($\vec{F}_s \cdot \vec{t} \geq 0$) affects k_w, resulting in a stall force, ~4 pN, beyond which motors cease walking. Each point connecting two adjacent actin segments on a filament has two

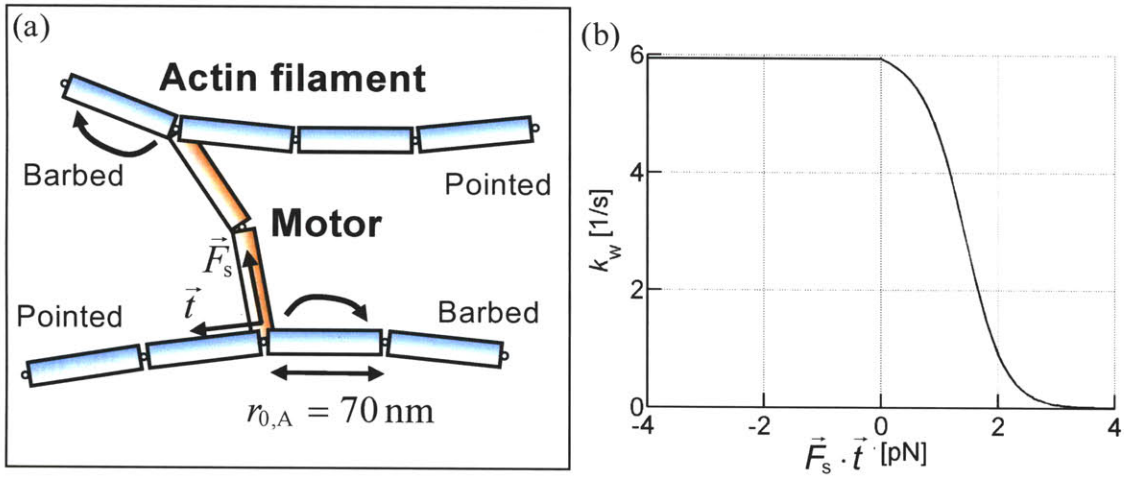

Figure 4.1 Walking of motors in our model. (a) A schematic diagram showing the walking event of a motor on actin filaments. $\vec{F}_s = \nabla U_s$ is a force acting on the arm of a motor, $\vec{t}$ is a unit tangential vector to an actin segment toward a pointed end, and $r_{0,A}$ is the equilibrium length of a single actin segment. Bent arrows represent a walking process that the motor arm jumps from a current binding point to a next one located toward a barbed end. (b) A walking rate, k_w, depending on $\vec{F}_s \cdot \vec{t}$. While $\vec{F}_s$ tilted to a pointed end significantly decreases k_w ($\vec{F}_s \cdot \vec{t} > 0$), $\vec{F}_s$ directed to a barbed end has no effect on k_w ($\vec{F}_s \cdot \vec{t} < 0$).

binding sites for either motor or ACP; a motor is capable of walking only when a next point located toward a barbed end has at least one available site. At each walking event, the end point of a motor arm instantly jumps from a current point to the next one, leading to a displacement of about $r_{0,A}$. If the arm reaches the last point on a filament, it remains there until it unbinds.

As with ACPs, motor proteins also unbind following Bell's equation as ACPs [47]:

$$k_{\mathrm{ub,M}}\left(\vec{F}_{\mathrm{s}}\right)=\begin{cases} k_{\mathrm{ub,M}}^{0}\exp\left(\dfrac{\lambda_{\mathrm{ub,M}}\left|\vec{F}_{\mathrm{s}}\right|}{k_{\mathrm{B}}T}\right) & \text{if } r\geq r_0 \\ k_{\mathrm{ub,M}}^{0} & \text{if } r<r_0 \end{cases} \quad [\mathrm{s}^{-1}] \tag{4.4}$$

where $k_{\mathrm{ub,M}}^{0}=0.02\ \mathrm{s}^{-1}$ is the zero-force unbinding rate coefficient, and $\lambda_{\mathrm{ub,M}}=2.6\times10^{-9}$ m is the mechanical compliance of the bond for unbinding [96]. These parameter values correspond to a single heavy meromyosin (HMM) in the ADP state, not a minifilament consisting of many myosin II molecules. Since time that the minifilament spends in a bound state is highly dependent upon how many myosin heads are bound, the measurement and modeling of minifilament unbinding are both quite difficult. Note that by comparing $k_{\mathrm{ub,M}}$ and $\lambda_{\mathrm{ub,M}}$ with $k_{\mathrm{ub,ACP}}$ and $\lambda_{\mathrm{ub,ACP}}$, it can be seen that a motor unbinds less readily than a crosslink at zero force but becomes proportionately more likely to unbind as force increases. Although unbinding of motors is also one of the phases of walking, these two events are considered separable for systematic analysis. For simplicity, simultaneous unbinding of both motor arms is prohibited as ACPs.

4.2.4. Boundary Conditions of the Computational Domain

As described in Chapter 2, for bulk rheology measurements, filaments passing through boundaries were severed and irreversibly clamped to the boundaries. However, in some of the morphological studies here, actin filaments are attached to boundaries via breakable bonds mimicking focal adhesions between a cell membrane and the cytoskeleton; detachment from boundaries is permitted following Bell's equation whose k_{ub}^{0} and λ_{ub} can be set differently on the six boundaries. Since focal adhesions are known to be facilitated by filamin A [97], we set the values of k_{ub}^{0} and λ_{ub} based on those of ACP. Rebinding of filaments to boundaries is not allowed.

In addition, for morphological studies, the boundaries are allowed to move as a result of the normal stress acting on them. The domain is assumed to be surrounded by an elastic medium with different Young's modulus, E, on six boundaries of the domain. The boundary (assumed to remain planar) experiences a normal stress of τ_n is displaced to a location corresponding to a strain of τ_n / E. This crudely simulates a cell located in extracellular matrix with uneven stiffnesses such as endothelial cells although many fundamental aspects are ignored such as hydrodynamics and poroelastic effects.

4.3. Results

4.3.1. Effects of Concentrations of Motors and ACPs

First, we investigated the effects of concentration of motors and ACPs on viscoelastic moduli using a rather small network in a cubical domain whose width is 2.8 μm

for computational efficiency.

4.3.1.1. Motor Concentration (R_M)

At three different R_{ACP} (0, 0.005, and 0.010), G' at 10 Hz is measured with varied R_M (Figure 4.2a). Note that in our model, motors do not self-assemble into motor minifilaments, so that R_M in the simulation corresponds to R for the minifilament in experiments. G' appears to exhibit a power-law behavior:

$$G' \sim R_M^x \tag{4.5}$$

although x ranges between 0.9 and 1.3 and tends to decrease slightly with higher R_{ACP} since ACPs can suppress motor walking by occupying the binding sites on actin segments although ACPs are capable of increasing G' via crosslinking. At $R_{ACP} = 0$, motors markedly stiffen a network with G' enhanced about 100-fold since greater contractile forces are generated by a larger number of motors. This tendency has been observed in an experiments [18] although the existence of a threshold myosin concentration above which networks begin to stiffen in the experiment is not observed in our study. Considering multimerization of myosin II molecules, a certain amount of myosin II would be necessary for the minifilament to be processive. In our model where motors do not self-assemble, it is not surprising that the threshold of R_M does not appear.

Plots of G' (Figure 4.2b) and G'' (Figure 4.2c) versus frequency with four different R_M at $R_{ACP} = 0.005$ show that, with higher R_M, the magnitude of G' steadily increases with a fairly consistent slope, whereas in the experiment [18], concentration of myosin II affects both magnitude and slope of G'. G'' tends to increase at lower frequencies with greater

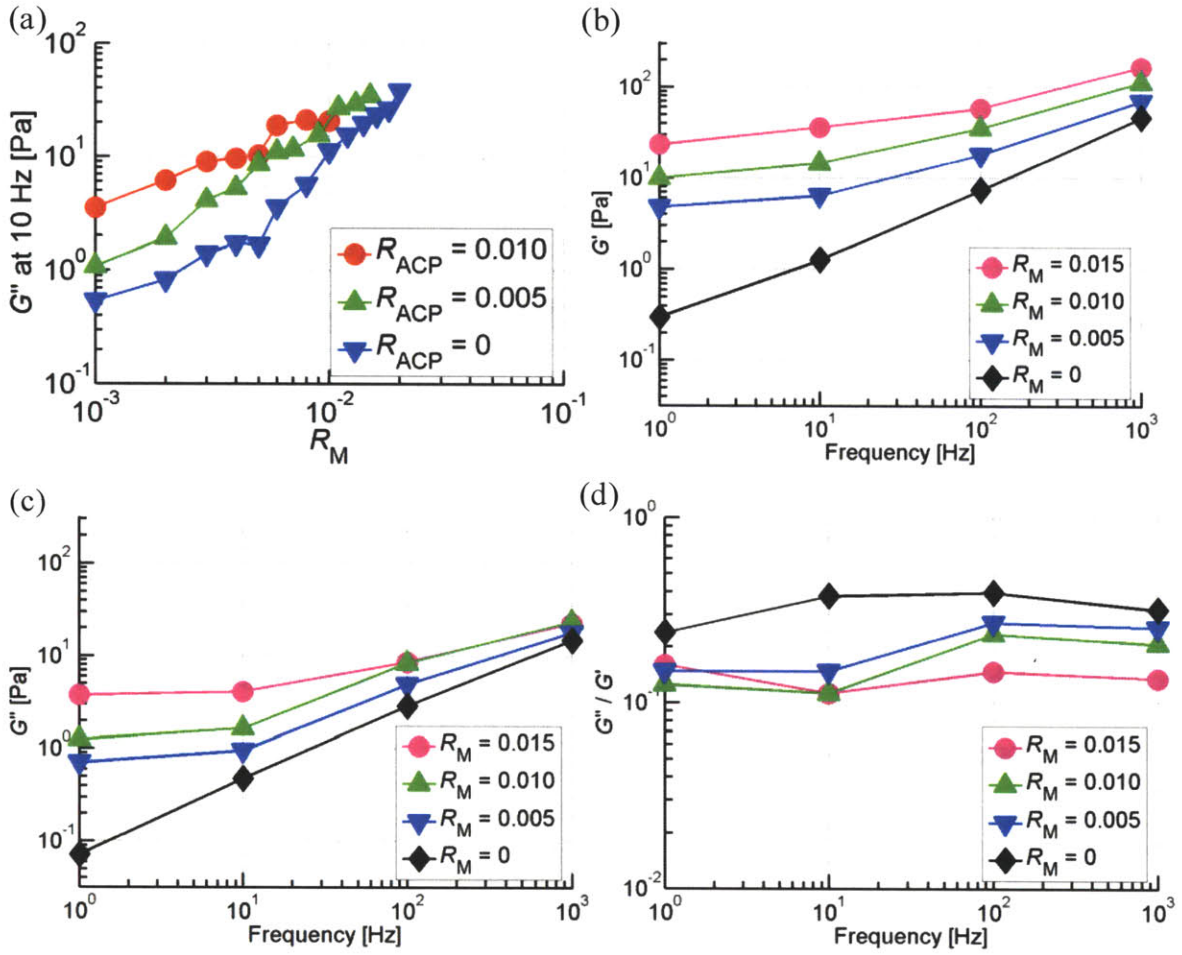

Figure 4.2 G' and G" with different motor concentrations. (a) G' versus R_M at 10 Hz with R_{ACP} = 0.010 (red circles), 0.005 (green triangle), and 0 (blue inverted triangles). In all cases, G' increases with higher R_M following the power-law behavior, $G' \sim R_M^x$, where x ranges between 0.9 and 1.3. (b) G' versus frequency at R_M = 0.015 (magenta circles), 0.010 (green triangles), 0.005 (blue inverted triangles), and 0 (black diamonds). R_{ACP} is fixed at 0.005. With higher R_M, G' has greater magnitude with relatively consistent slope. (c) G" versus frequency. Motors increase G" due to more motor unbinding events. (d) The ratio of G" to G' versus frequency. Despite increasing G", the ratio falling with higher R_M indicates that motors enhance the elasticity of networks.

R_M primarily due to more unbinding events of motors. Despite increasing G", the ratio of G" to G' in Figure 4.2d indicates elasticity of networks is enhanced by motors.

4.3.1.2. ACP Concentration (R_{ACP})

G' at 10 Hz is also measured at three different R_M (0, 0.005, and 0.010) with various R_{ACP} (Figure 4.3a). ACPs crosslink filaments more stably than motors against forces due to the lower sensitivity of ACP unbinding ($\lambda_{ub,ACP} < \lambda_{ub,M}$), which sustains percolation of networks and prevents a network from severely aggregating as shown later. This nature of ACPs contributes to the increase of G' as seen in the case with $R_M = 0.005$. However, at $R_M = 0.010$, addition of ACPs results in only a minor change in G' because the occupancy of binding sites on actin segments by ACPs can reduce the average walking distance per motor as shown in Figure 4.3b.

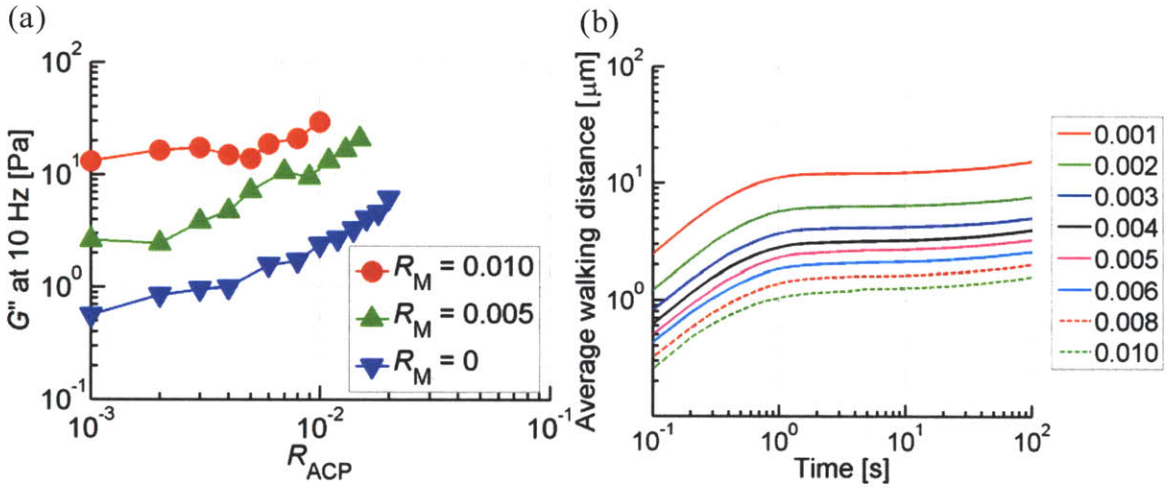

Figure 4.3 G' with different ACP concentrations. (a) G' versus R_{ACP} at 10 Hz with R_M = 0.010 (red circles), 0.005 (green triangle), and 0.0 (blue inverted triangles). While the influences of R_{ACP} are significant at R_M = 0.005 and 0, G' increase slightly at R_M = 0.010. (b) At R_M = 0.010, average walking distance per motor decreases with higher R_{ACP} (numbers in the legend), indicating that ACPs hinder motors from walking.

4.3.2. Significance of Kinetic Parameters

To evaluate the relative importance of three rate processes in our simulation – the unbinding and walking of motors and the unbinding of ACPs – we examined G' at 10 Hz with mechanical sensitivity (λ) of each process varied with other parameters held fixed. In Figure 4.4a, the effects of a change in $\lambda_{ub,M}$ on G' are impressive; processive motors that are capable of walking for a long time without unbinding due to a low $\lambda_{ub,M}$ lead to very high G', whereas the increase of G' induced by non-processive motors with high $\lambda_{ub,M}$ is significantly smaller. By contrast, the influence of $\lambda_{ub,ACP}$ and λ_w on G' is small regardless of the existence of motor unbinding. It might seem surprising at first, that λ_w (that determines the stall force beyond which motors cease walking) plays such an insignificant role. However, even stalled motors are able to bear a force larger than the stall level if other motors indirectly connected to them continue walking, inducing additional contractile stress transmitted through the network. Figure 4.4b representing the distribution of longitudinal forces, $\vec{F}_s \cdot \vec{t}$, acting on motors with three different $\lambda_{ub,M}$ demonstrates the interesting result that the forces can be significantly higher than the stall level, ~4 pN.

These observations imply that the amount of force that a motor can support before it unbinds is the most significant determinant of G'. To verify this hypothesis, G' (Figure 4.4c) and G'' (Figure 4.4d) are calculated as functions of frequency with $\lambda_{ub,M}$ varied from one-tenth to ten-fold the standard value. $\lambda_{ub,M}$ affects G' to a vastly greater extent than R_M; G' with low $\lambda_{ub,M}$ exhibits frequency-independent behavior, whereas G' with the highest $\lambda_{ub,M}$ is hardly different from that without any motors at all (Figure 4.2b). Of

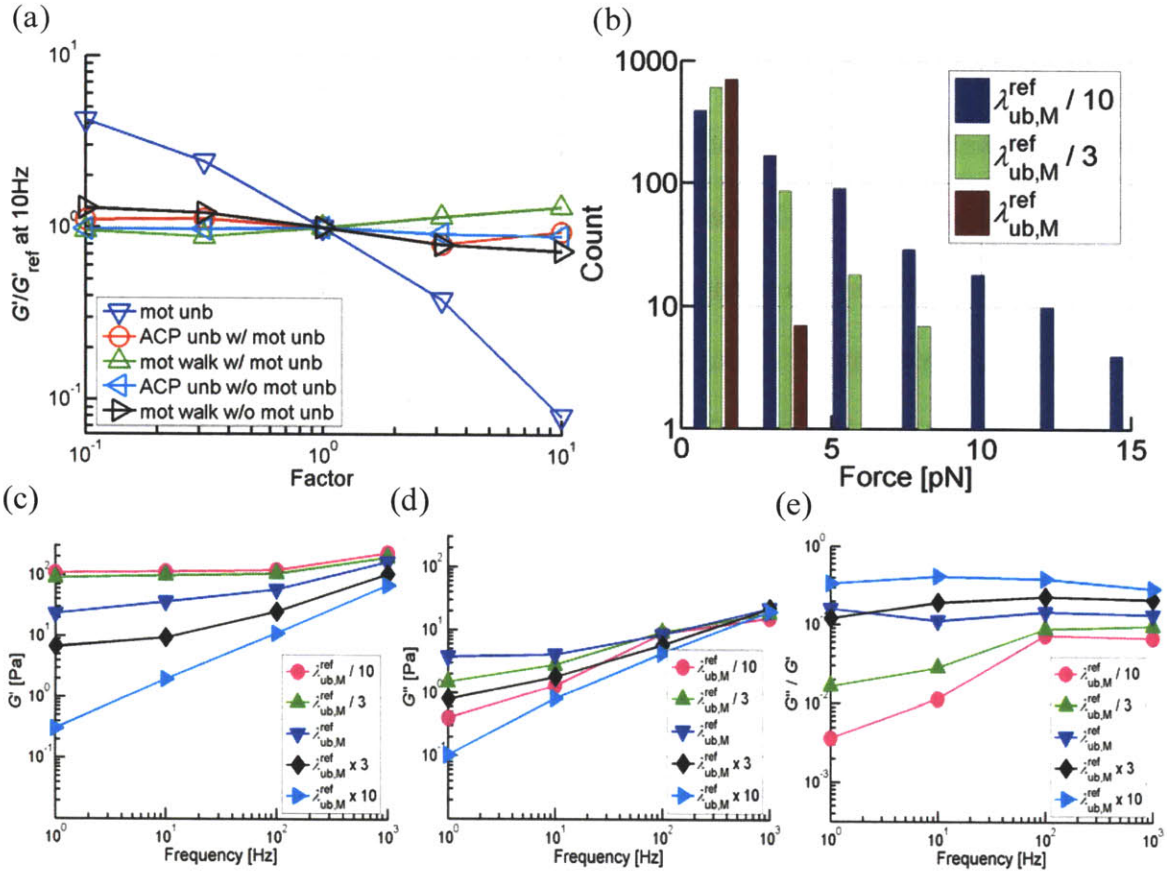

Figure 4.4 Effects of kinetic parameters and the importance of motor unbinding. A single network with $R_{ACP} = 0.005$ and $R_M = 0.015$ is used for these simulations. (a) Ratio of G' with varied λ (= factor $\times \lambda^{ref}$) to reference G' with λ^{ref}. Blue inverted triangles: $\lambda_{ub,M}$, red circles and green triangles: $\lambda_{ub,ACP}$ and λ_w with motor unbinding, and cyan left-pointed triangles and black right-pointed triangles: $\lambda_{ub,ACP}$ and λ_w without motor unbinding. $\lambda_{ub,M}$ highly affects G' while other λ's have negligible effects regardless of the existence of motor unbinding. (b) Distribution of longitudinal forces acting on motors depending on $\lambda_{ub,M}$ with a stall force of ~4 pN. Forces distributions are highly governed by $\lambda_{ub,M}$ and can be greater than the stall level. (c) G' versus frequency at five different $\lambda_{ub,M}$. $\lambda_{ub,M}$ significantly affects both the magnitude and slopes of G' unlike R_M. (d) G'' versus frequency. G'' has the maximum values at $\lambda_{ub,M} = \lambda^{ref}_{ub,M}$. (e) Ratio of G'' to G'. Lower $\lambda_{ub,M}$ induces very elastic networks.

particular note, is that $\lambda_{ub,M}$ significantly changes the slope of G' unlike R_M. This tendency is strikingly similar to [48] where the processivity of myosin II was adjusted by changing the concentration of ATP using creatine phosphokinase. This implies that the slope of G' is governed mainly by motor processivity, and thus the variations in G' due to different concentrations of myosin II in [18] might originate from changes in both concentration and processivity of myosin minifilament. G'' also exhibits quite interesting behaviors (Figure 4.4d); G'' increases from $\lambda_{ub,M}^{ref}/10$ to $\lambda_{ub,M}^{ref}$ since unbinding events of motors occur by smaller forces, inducing greater energy dissipation. However, when $\lambda_{ub,M}^{ref}$ is increased further, to $\lambda_{ub,M}^{ref} \times 10$, it falls; this is because the number of bound motors significantly decreases as motors become quite sensitive to even very small forces. Despite the non-monotonic behavior of G'', the ratio of G'' to G' indicates that networks with lower $\lambda_{ub,M}$ are much more elastic (Figure 4.4e).

4.3.3. Governing Factors of Network Morphology

We investigated the morphology of either small (2.8 μm) or large active network (5.0 μm), and preliminary results will be discussed here.

4.3.3.1. Effects of ACPs

We probed the roles of ACPs in morphology of networks by comparing two cases with motors (R_M = 0.010), one of which has ACPs (R_{ACP} = 0.003, Figure 4.5a,c,e,g) while the other does not (R_{ACP} = 0, Figure 4.5b,d,f,h). Periodic boundary conditions are applied in all directions. In Figure 4.5f,h, most parts of the network form a large aster, which has

(a) At t = 1 s with ACP

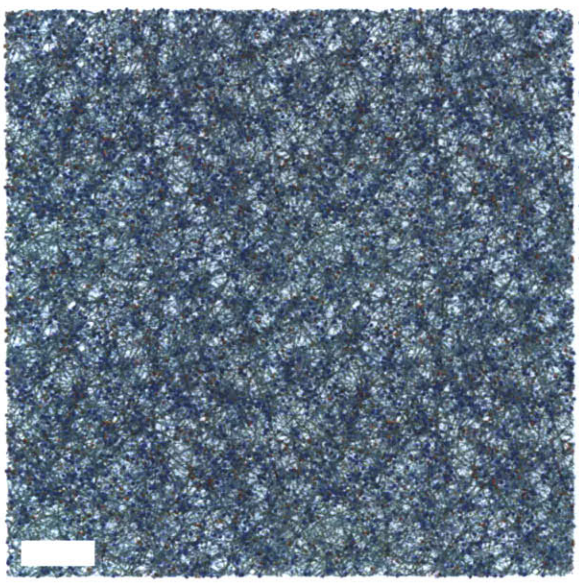

(b) At t = 1 s without ACP

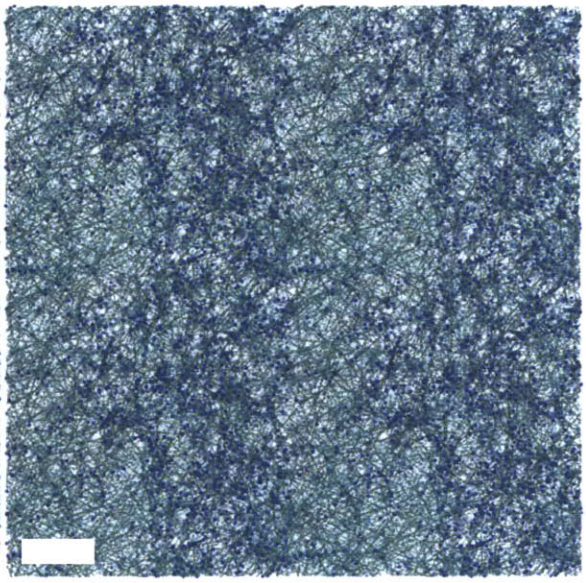

(c) At t = 2 s with ACP

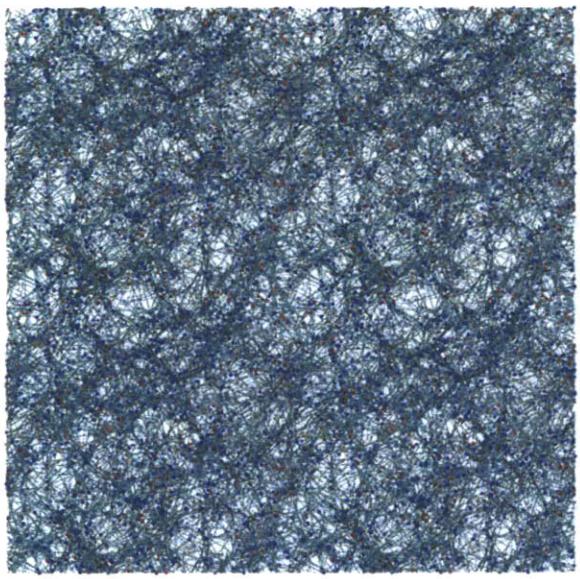

(d) At t = 2 s without ACP

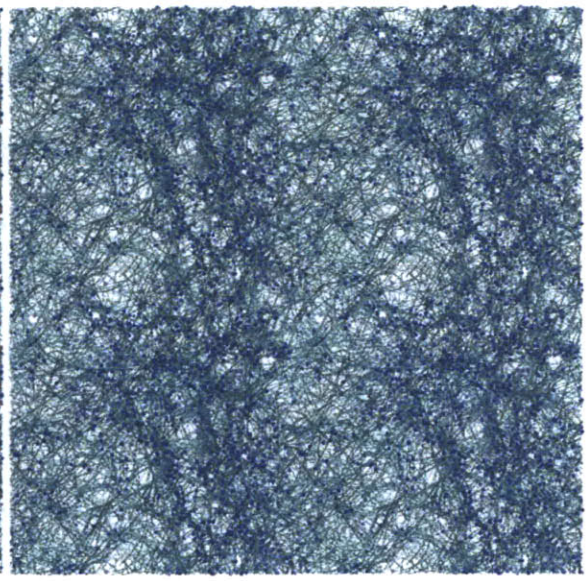

(e) At t = 3 s with ACP

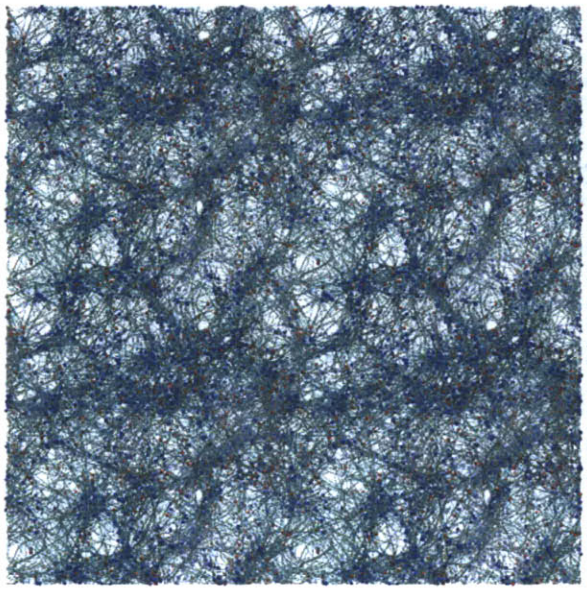

(f) At t = 3 s without ACP

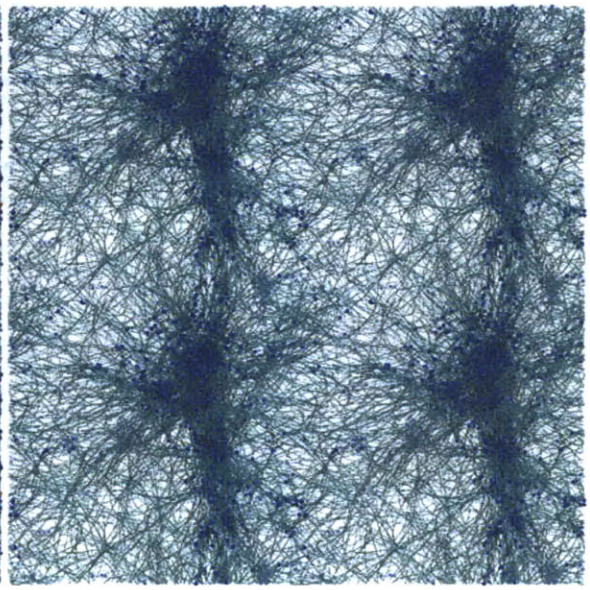

(g) At t = 4 s with ACP

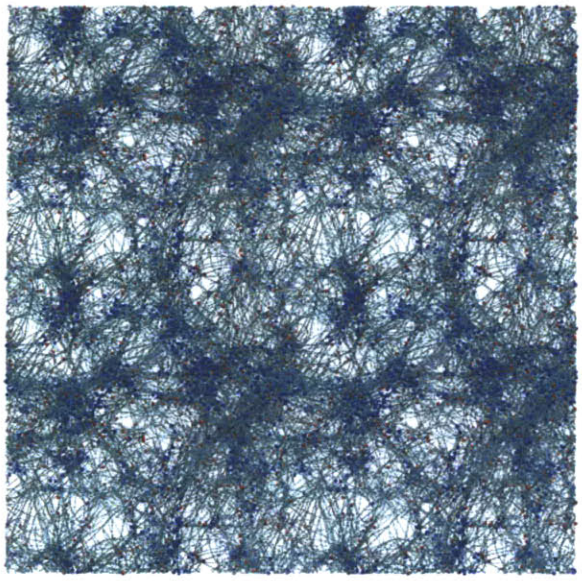

(h) At t = 4 s without ACP

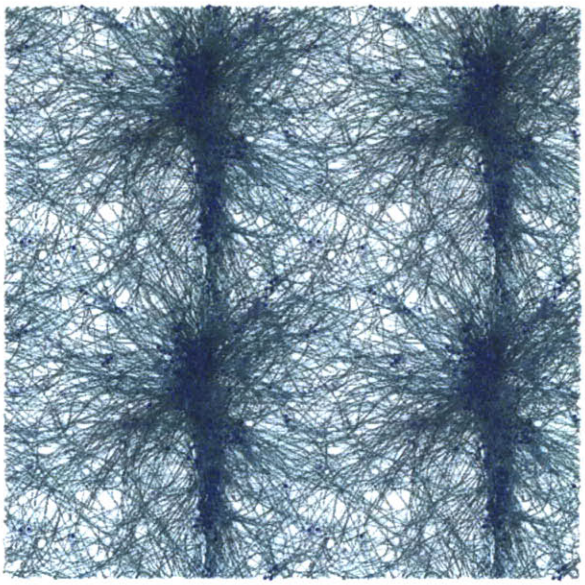

(i) (j)

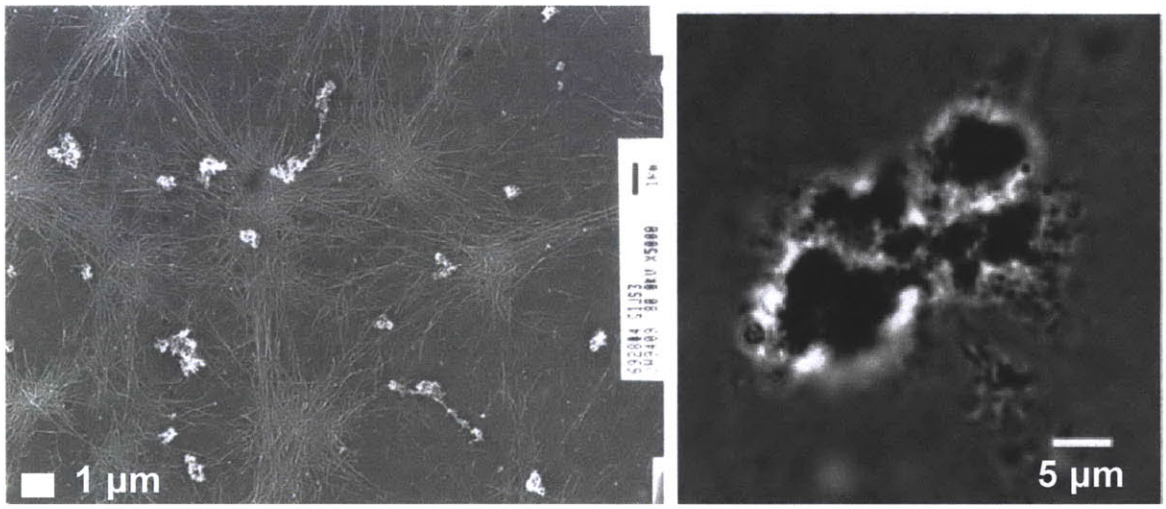

Figure 4.5 Morphology of networks consisting of actin filaments (cyan, C_A=12 μM) and motors (blue, R_M = 0.010) (a,c,e,g) with or (b,d,f,h) without ACPs (red, R_{ACP} = 0.003) at (a,b) t = 1 s, (c,d) 2 s , (e,f) 3 s , and (g,h) 4 s. Periodic boundary conditions are applied in all directions. For clearer visualization of the aggregates, each network is duplicated twice in each direction. Scale bars in (a,b) equal 1 μm. Networks without ACPs (b,d,f,h) are more heterogeneous than those with ACPs (a,c,e,g). (i, j) Morphology of reconstituted actin networks with only myosin II adapted from (i) [18] and (j) [48]. Due to the contractile actions of myosin II, they tend to form many asters, in a process referred to as superprecipitation.

been observed in experiments and termed "super-precipitation" [98], and the aster has been observed in several experiments with reconstituted actin solutions only in the presence of myosin II (Figure 4.5i,j) [18,48]. The aster does not appear when unbinding of motors is prohibited (data not shown), meaning that the aggregation process must be associated with the subsequent unbinding events in conjunction with walking. By contrast, in Figure 4.5e,g, despite the formation of a few small aggregates, the overall distribution of actin filaments and motors is still relatively homogenous. This morphology is quite similar to that illustrated in a movie from [48] showing nonthermal fluctuations of the actin network

crosslinked by biotin and neutravidin with myosin and also to the reconstituted actin network crosslinked by filamin with myosin II in [18].

Figure 4.6 represents the morphology of active networks used to investigate the rheological effects of R_{ACP} in Section 4.3.1.2. Periodic boundary conditions are applied except in the z-direction, which was required due to the bulk rheology measurement. Without ACPs, most actin filaments either agglomerate near z-boundaries or form asters, causing very poor percolation. On the contrary, networks with higher R_{ACP} tend to exhibit more homogeneous distributions of actin filaments and motors, consistent with Figure 4.5, and their high connectivity between the upper and lower boundaries in z-direction contributes to greater G' as mentioned earlier.

ACPs that are less sensitive to forces can behave as a stabilizer that prevents a network from aggregating or forming asters, and also they hinder motors from walking by

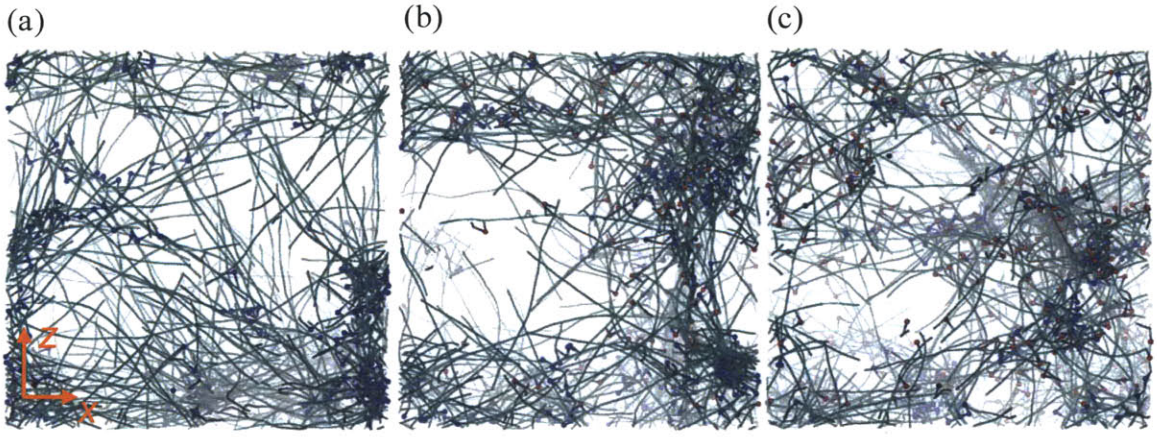

Figure 4.6 Morphology of networks employed for investigation of rheological effects of R_{ACP} in Section 4.3.1.2, composed of actins (cyan, C_A = 12 μM), motors (blue, R_M = 0.010), and ACPs (red). Periodic boundary conditions are applied except in the z-direction, and the width of the cubical domain is 2.8 μm. (a) R_{ACP} = 0. (b) R_{ACP} = 0.005. (c) R_{ACP} = 0.010.

occupying binding sites on actin segments. All of these actions lead to a rather uniform distribution of components.

4.3.3.2. Effects of Motors

In Sections 4.3.1.1 and 4.3.2, we showed that the activities of motors increasing the elasticity of networks can be enhanced via a larger number of motors (higher R_M) or greater processivity (lower $\lambda_{ub,M}$). Here, to investigate how the motor activities affect morphologies, we examined networks with different R_M and $\lambda_{ub,M}$. Figure 4.7 represents morphology of networks that were employed to study the effects of R_M on rheology in the Section 4.3.1.1. As expected, at the same R_{ACP}, a greater number of motors leads to more heterogeneous distributions with many aggregates. In Figure 4.8, a network with the highest $\lambda_{ub,M}$ exhibits a more uniform distribution since few motors remain in a bound state. However, as $\lambda_{ub,M}$ decreases, the stable walking motions of motors induce a highly

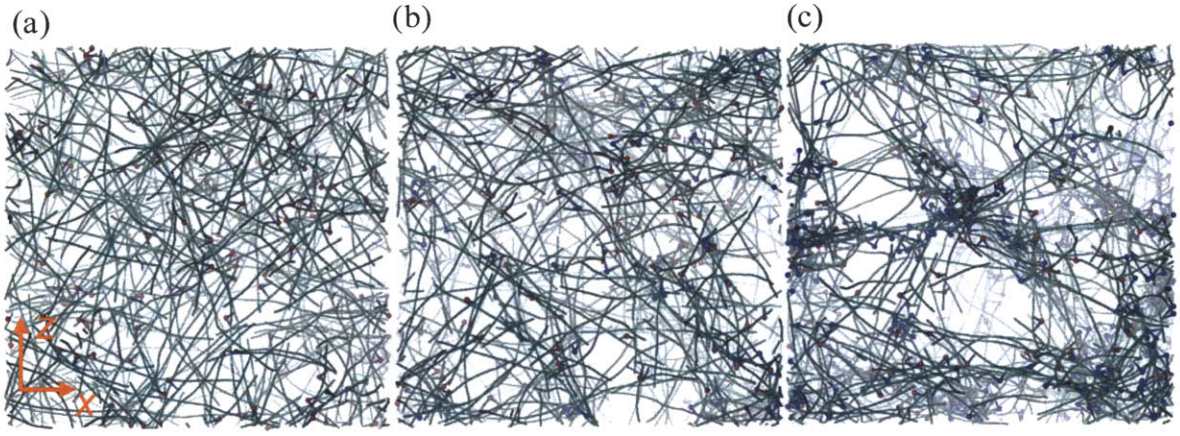

Figure 4.7 Morphology of networks used to estimate the influences of R_M on rheology in the Section 4.3.1.1, comprising actin (cyan, C_A = 12 μM), motors (blue), and ACPs (red, R_{ACP} = 0.005). Periodic boundary conditions are imposed in x- and y-direction on a cubical domain whose width is 2.8 μm. (a) R_M = 0. (b) R_M = 0.007. (c) R_M = 0.015.

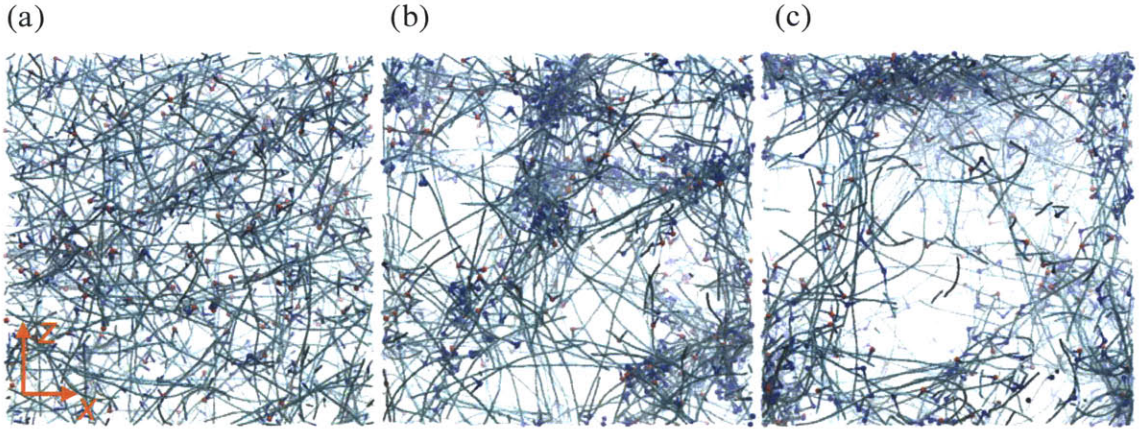

Figure 4.8 Morphology of networks whose G' was measured to probe the effects of $\lambda_{ub,M}$, consisting of actin (cyan, C_A = 12 μM), motors (blue, R_M = 0.015), and ACPs (red, R_{ACP} = 0.005). The domain whose width is 2.8 μm has periodic boundary conditions on the x and y boundaries. (a) $\lambda_{ub,M} = \lambda_{M,ub}^{ref} \times 10$. (b) $\lambda_{ub,M} = \lambda_{ub,M}^{ref} \times 3$. (c) $\lambda_{ub,M} = \lambda_{ub,M}^{ref}$. Lower $\lambda_{ub,M}$ results in highly processive motors, leading to the heterogeneous distributions of constituents with many piles of actin filaments.

heterogeneous morphology. From these observations, it is implied that motor activities tend to aggregate networks by contractile forces, resulting in non-uniform distributions.

4.3.3.3. Effects of Adhesions to Boundaries and External Medium Stiffness

We also studied the influences of the adhesions of networks to boundaries and the medium stiffness on network morphology. Based on our previous observations that only those actin networks with motors tend to aggregate with poor percolation, we added a small amount of ACPs (R_{ACP} = 0.003) with motors (R_M = 0.010) to stabilize the networks. Filaments crossing boundaries are severed, then clamped on the boundaries in all directions, followed by the deactivation of periodic boundary conditions.

First, we allow the clamped filaments to unbind from boundaries following Bell's

equation with $k^0_{ub,ACP}$ and $\lambda_{ub,ACP}$ as explained in the Section 4.2.4, which is intended to mimic some aspects of the behavior in focal adhesions. $k^0_{ub,ACP}$ is identical on all six boundaries, whereas different values for $\lambda_{ub,ACP}$ are imposed on a pair of boundaries in each direction. With $\lambda_{ub,ACP}$ 10 times greater on two boundaries in x-direction than those on other four boundaries in y- and z-directions ($\lambda_{ub,ACP,x} = 10\lambda_{ub,ACP,y} = 10\lambda_{ub,ACP,z} = 10\,\lambda^{ref}_{ub,ACP}$), a 2-D sheet-like structure with multiple contractile foci is formed (Figure 4.9b,d,f) as observed in a computational study where clamped boundary condition is applied in two directions with a free condition imposed in the other direction [63]. By contrast, with $\lambda_{ub,ACP,x} = \lambda_{ub,ACP,y} = 10\lambda_{ub,ACP,z} = 10\,\lambda^{ref}_{ub,ACP}$, a 1-D stress-fiber-like structure is generated (Figure 4.9a,c,e) as in the other computational study where a bundle appears in response to the stretching of a computational domain with dynamic crosslinking points [62]. Also, in experiments [99], formation of stress fibers in the direction of cyclic stretching was observed, attributable to changes in focal adhesion sites due to the stimulus. It would be

(a) At t = 5 s with $\lambda_x = \lambda_y = 10\lambda_z$

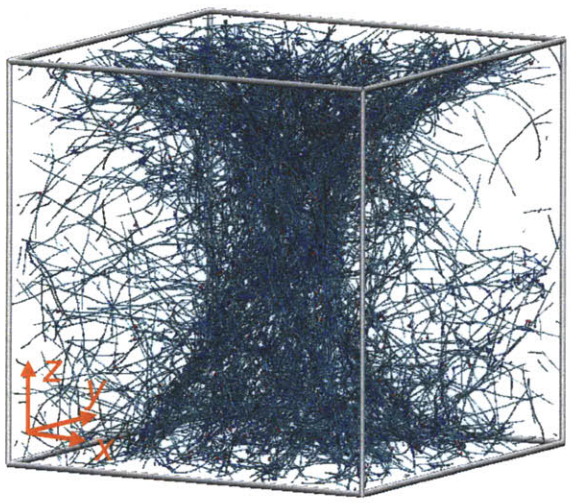

(b) At t = 5 s with $\lambda_x = 10\lambda_y = 10\lambda_z$

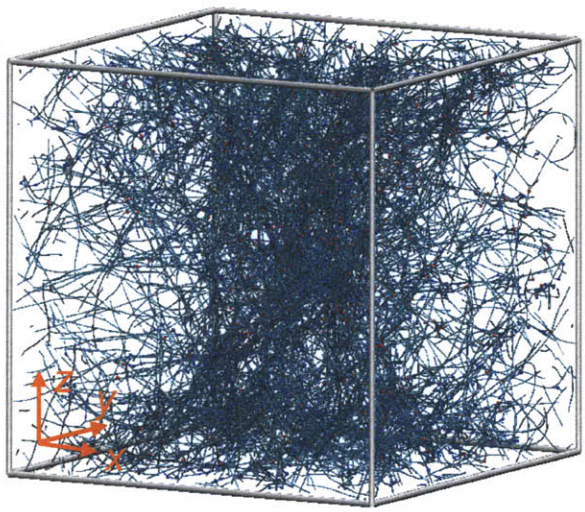

(c) At t = 50 s with $\lambda_x = \lambda_y = 10\lambda_z$

(d) At t = 50 s with $\lambda_x = 10\lambda_y = 10\lambda_z$

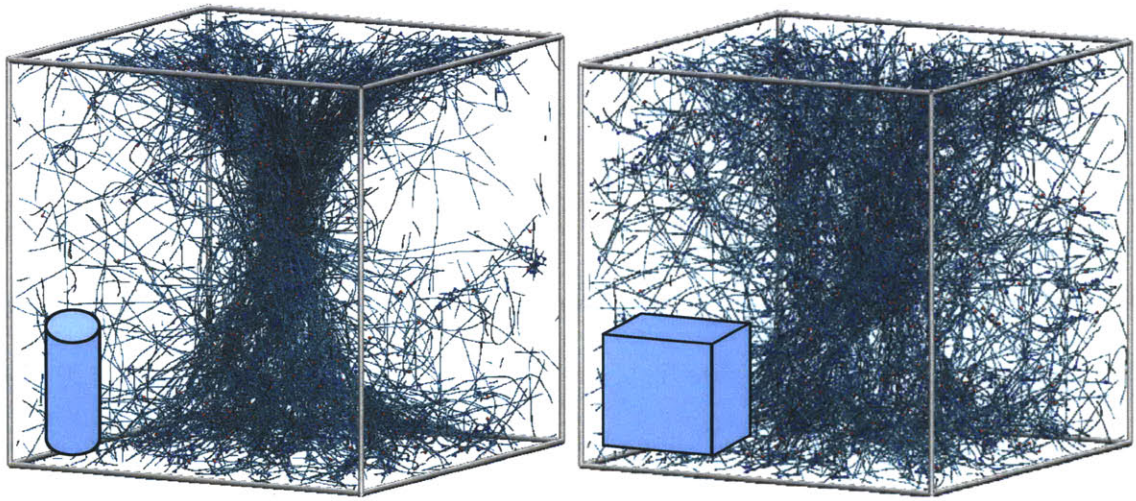

(e) At t = 50 s with $\lambda_x = \lambda_y = 10\lambda_z$

(f) At t = 50 s with $\lambda_x = 10\lambda_y = 10\lambda_z$

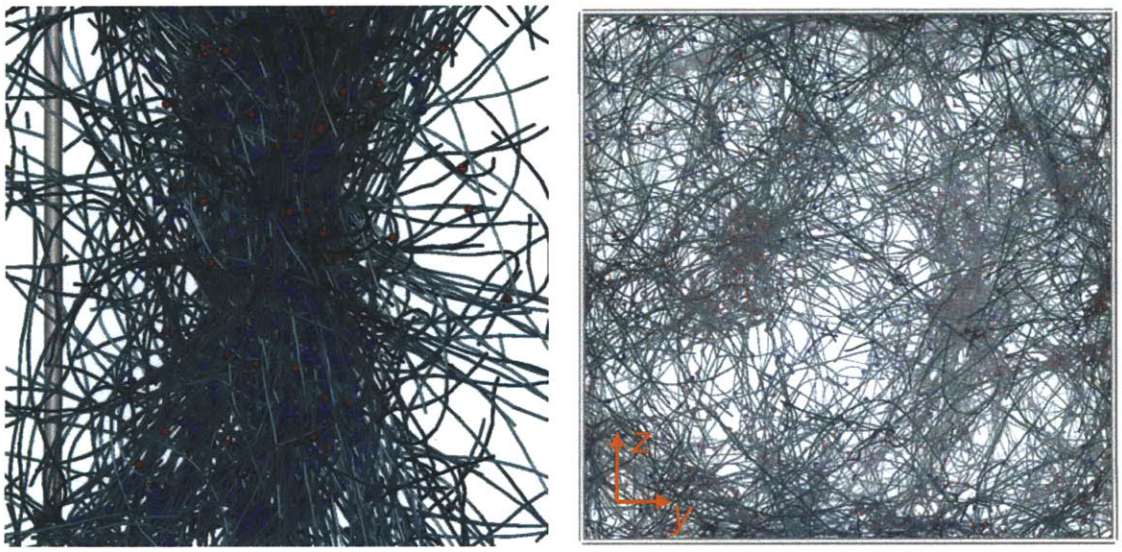

Figure 4.9 Network morphology under clamped boundary conditions with detachable filaments. Different values of $\lambda_{ub,ACP}$ are applied in each direction; outer gray lines represent the edges of the domain. (a,c,e) With $\lambda_{ub,ACP,x} = \lambda_{ub,ACP,y} = 10\lambda_{ub,ACP,z} = 10\,\lambda_{ub,ACP}^{ref}$, a structure similar to stress fibers gradually emerges at (a) t = 5 s and (c) t = 50 s. (e) Most filaments located at mid of the 1-D structure are aligned in z-direction with multiple motors and ACPs. (b,d,f) With $\lambda_{ub,ACP,x} = 10\lambda_{ub,ACP,y} = 10\lambda_{ub,ACP,z} = 10\,\lambda_{ub,ACP}^{ref}$, a 2-D sheet-like structure is formed at (b) t = 5 s and (d) t = 50 s. (f) View from a different perspective clearly shows the flat structure with several agglomerates.

interesting to allow reattachment of filaments to boundaries or to impose various distributions of $\lambda_{ub,ACP}$ even on one boundary (e.g. lower $\lambda_{ub,ACP}$ on several lines oriented in x-direction on z-boundary).

Second, while boundaries of the domain have been stationary in previous cases, they are allowed to move in the direction normal to them following the stress-strain relationship explained in Section 4.2.4, which crudely simulates the effect of a surrounding elastic medium. Using a small value for E on the x- and y- boundaries ($E_x = E_y = 20$ Pa) and large E on the two remaining (z) boundaries ($E_z = 10^4$ Pa), the initial cubical domain shown in Figure 4.10a deforms into long rectangular one with $C_A = 177$ μM due to normal stress induced by the contractile forces of motors, leading to the nematic orientation of actin filaments (Figure 4.10b) similar to [100]. Using $E_x = E_y = E_z = 20$ Pa, the domain becomes a small cubic with $C_A = 1$ mM, containing highly bent filaments (Figure 4.10c). Although these results with movable boundaries are interesting, caution must be exercised in applying these results to real systems because of the idealized conditions imposed (e.g., planarity of boundary surfaces).

4.4. Discussion

In this study we sought to elucidate roles of molecular motors in actin morphology and rheology using a 3-D Brownian dynamics simulation. It was found that the concentration and unbinding event of motors as well as ACP concentration exert large effects on the elasticity of networks; the networks become more stiff with more ACPs and processive motors, consistent with recent experiments [18]. Morphology of the active

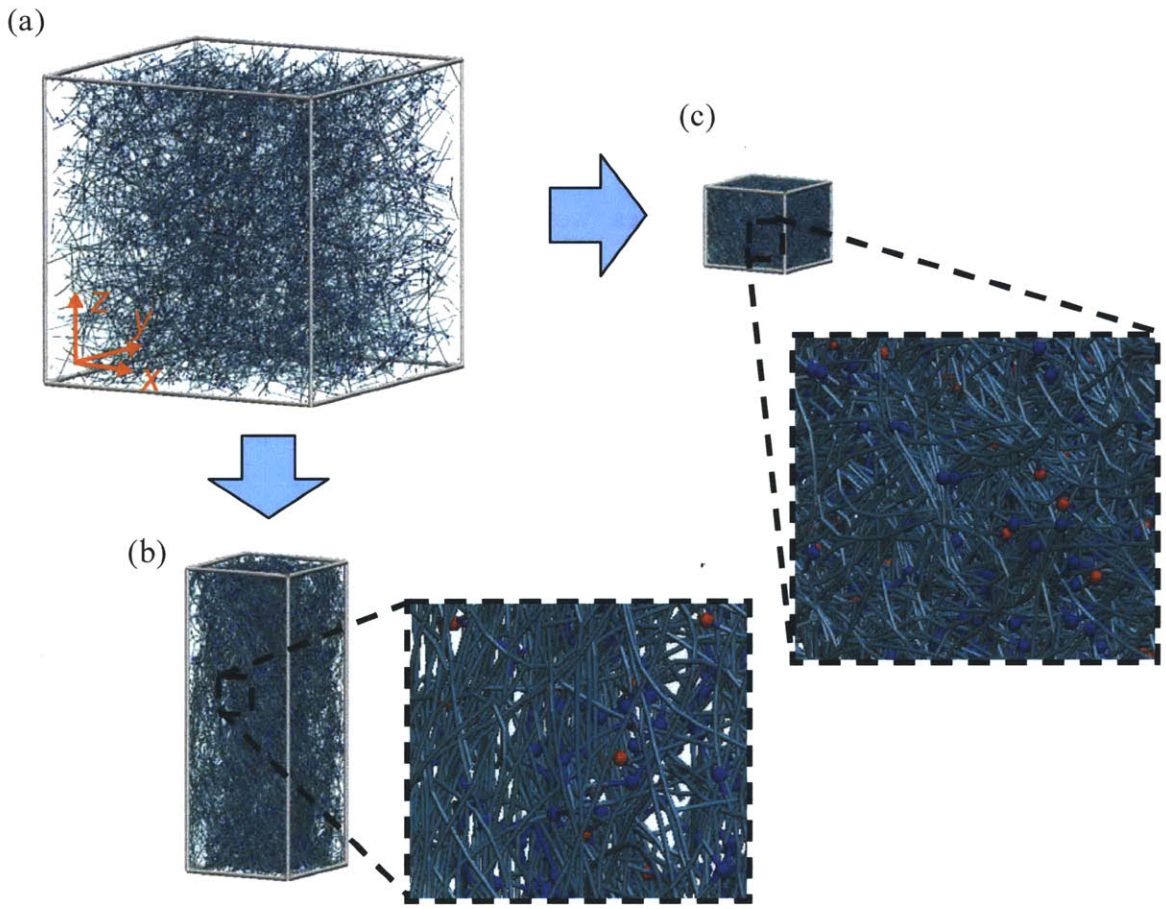

Figure 4.10 Morphology of networks with moving boundaries following stress-strain relationship. (a) An initial network showing the original size of the domain. (b) With $E_x = E_y = 20$ Pa and $E_z = 10^4$ Pa, the domain quickly shrinks in x- and y-directions due to normal stress, inducing the nematic orientation of actin filaments with $C_A = 177$ μM. (c) With $E_x = E_y = E_z = 20$ Pa, the domain reduces to a small cube with $C_A = 1$ mM containing highly bent filaments.

networks tends to be more heterogeneous with a greater number of highly processive motors, forming aggregates and asters. In contrast, ACPs help the networks to maintain a homogeneous distribution by acting to stabilize the initial homogenous morphology. These influences of ACPs and motors on the morphology are qualitatively quite similar to

in vitro experiments [18,48]. We also found that adhesions of networks to boundaries and stiffness of surrounded elastic medium are also important factors governing the morphology of the networks. Interestingly, a stress-fiber-like structure was formed when the adhesions of filaments to boundaries were strengthened only in the z-direction. Considering the importance of stress fibers in cells, it would be useful to pursue this approach further to elucidate the assembly mechanism of stress fibers.

As mentioned earlier, myosin II tends to multimerize to a thick myosin minifilament unlike other types of myosin, but the role of multimerization is not quite clear. In [18], it was presumed that a constant number of myosin II molecules would always multimerize to form a single myosin minifilament based on the observation that reconstituted myosin II solutions generate myosin minifilaments of about 1 μm in length corresponding to 300 myosins. However, it might not be the case if myosin II exists in conjunction with actin filaments since myosin II can either form a myosin minifilament or bind to actin filaments. It is likely that a change in concentration of myosin II in the experiments might have affected the concentration of myosin minifilaments; since this would affect processivity, this might have contributed to the increase in G' observed in [18]. Speculating further, cells might possess a mechanism that controls the extent of multimerization, which would enable them to regulate their stiffness even with the same number of myosin II molecules. For example, it was found that phosphorylation of only three threonine residues of myosin II can significantly change the self-assembly state to minifilament [101].

We computed the G' of networks with seven different values of R_M and six values of $\lambda_{ub,M}$. Again, note that motors in our study do not multimerize, indicating that motor

concentration (R_M) in the simulation corresponds directly to the concentration of myosin minifilaments in experiments [18]. G' tends to increase with higher R_M and lower $\lambda_{ub,M}$ (Figure 4.11), consistent with the previous findings in the Section 4.3.1.1 and 4.3.2. On the naïve assumption that $\lambda_{ub,M}$ of a motor consisting of n individual myosins is n-fold smaller than that of a single myosin, cases on each line in Figure 4.11 have the same number of myosins. As indicated by arrows, most of the lines have an optimal condition leading to maximum G'. It would be interesting to experimentally investigate whether the degree of multimerization does indeed vary and to search for such a mechanism.

In sum, our model including molecular motors mimicking behaviors of myosin minifilaments provided insights into underlying mechanisms of morphology and rheology of active actin networks. At the same time, the results suggest new experiments that

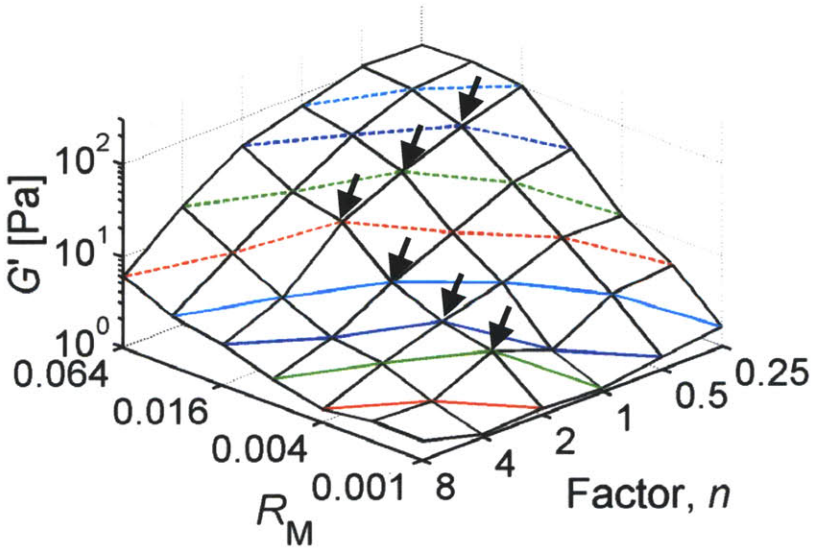

Figure 4.11 G' with seven R_M and six $\lambda_{ub,M}$ (= factor × $\lambda_{ub,M}^{ref}$). Consistent with our previous findings, G' increases with higher R_M and lower $\lambda_{ub,M}$. Colored lines indicate cases having the same number of myosins, and arrows show optimal conditions leading to maximum G'.

might be conducted both to further validate of the model but also to further elucidate the roles of motors in cytoskeletal rheology and morphology. Since the presented results are still preliminary, the improvement of the model and various analyses will be performed as a next step.

Chapter 5

Conclusions and Future Work

This thesis has studied the morphological and rheological properties of actin-like networks using a 3-D computational model via Brownian dynamics. In Chapter 2, viscoelastic properties of actin networks irreversibly crosslinked by ACPs were investigated. We tested the effects of prestrain, the mechanical stiffnesses of actin filaments and ACPs, the thermal fluctuation of actin filaments, and the kind and concentration of ACPs on viscoelastic moduli of networks. In Chapter 3, we focused on the roles of unbinding and unfolding events of ACPs on rheological behaviors of actin networks. By simulating strain-stiffening, stress relaxation, and plastic deformation, it was found that unbinding is a predominant factor governing the rheology of actin networks. In Chapter 4, the influences of molecular motors on the morphology and rheology of actin networks were studied. Processive motors have an abilitiy to enhance the elasticity of networks and tend to increase the heterogeneity of network morphology. These studies provide insight into understanding the morphology and rheology of passive and active actin networks.

Further studies incorporating membranes will be interesting in that the new model will be able to simulate reconstituted cell-like structures that have recently been employed in various experiments [102]. As a first step, the simplest membrane model will be employed where a membrane is considered an elastic shell whose surface is represented by

a triangulated mesh. Spring and bending forces are applied between the adjacent vertices of the components, yielding realistic mechanical stiffnesses of cellular membranes. Also, actin filaments could be allowed to reversibly bind to the vertices to simulate focal adhesions. If the simplest membrane model appears not to be sufficient, the implementation of more rigorous membrane models [103] would be required. Although the implicit hydrodynamics described in the Section 2.2.7 is valid in the current studies (except cases with moving boundaries) due to the unchanging size of the computational domain and the low volumetric percentage of networks (< 1%), a more rigorous hydrodynamics model [104,105] might be required to simulate the cell-like structure since the extensive deformation of membranes would cause the significant flow of internal medium, and give rise to poroelastic effects. In addition, the model can further be improved by adding other cellular components such as microtubules, intermediate filaments, and the nucleus. Most of the current computational approaches simulating a whole cell use FEM or very crude modeling. As mentioned in many references, such homogenized descriptions of cells are not sufficient to elucidate the underlying mechanism of cellular phenomena such as mechanotransduction and to find the distinct roles of different cellular constituents. On the contrary, the rigorous discrete-particle computational model including the membranes will be able to shed light to provide insights into many fundamental aspects of cells. Some of these would include (i) the changes in cell shape that occur during adhesion to a rigid surface, (ii) the rounding up of a cell upon release from the surface, (iii) the formation of different cytoskeletal structures internally, (iv) the deformations of a cell under various loading conditions, and (v) a number of different biological processes that occur during cell migration or mitosis. These are only a few

examples of how these models could be extended, but many more could be envisioned in a variety of applications.

Bibliography

1. H. Lodish, A. Berk, P. Matsudaira, C. A. Kaiser, M. Krieger, M. P. Scott, S. L. Zipursky, J. Darnell, *Molecular Cell Biology* (W. H. Freeman and Company, New York, 2004).
2. X. Trepat, L. H. Deng, S. S. An, D. Navajas, D. J. Tschumperlin, W. T. Gerthoffer, J. P. Butler, J. J. Fredberg, "Universal physical responses to stretch in the living cell," Nature **447**: 592-596 (2007).
3. B. D. Matthews, D. R. Overby, R. Mannix, D. E. Ingber, "Cellular adaptation to mechanical stress: role of integrins, Rho, cytoskeletal tension and mechanosensitive ion channels," J Cell Sci **119**: 508-518 (2006).
4. Y. Tseng, K. M. An, O. Esue, D. Wirtz, "The bimodal role of filamin in controlling the architecture and mechanics of F-actin networks," J Biol Chem **279**: 1819-1826 (2004).
5. M. R. K. Mofrad, R. D. Kamm, *Cytoskeletal Mechanics* (Cambridge University Press, New York, NY, 2006).
6. C. E. Schutt, J. C. Myslik, M. D. Rozycki, N. C. W. Goonesekere, U. Lindberg, "The Structure of Crystalline Profilin Beta-Actin," Nature **365**: 810-816 (1993).
7. K. C. Holmes, D. Popp, W. Gebhard, W. Kabsch, "Atomic Model of the Actin Filament," Nature **347**: 44-49 (1990).
8. F. Gittes, B. Mickey, J. Nettleton, J. Howard, "Flexural Rigidity of Microtubules and Actin-Filaments Measured from Thermal Fluctuations in Shape," J Cell Biol **120**: 923-934 (1993).
9. A. Ott, M. Magnasco, A. Simon, A. Libchaber, "Measurement of the Persistence Length of Polymerized Actin Using Fluorescence Microscopy," Phys Rev E **48**: R1642-R1645 (1993).
10. D. Sept, J. A. McCammon, "Thermodynamics and kinetics of actin filament nucleation," Biophys J **81**: 667-674 (2001).
11. J. A. Cooper, E. L. Buhle, S. B. Walker, T. Y. Tsong, T. D. Pollard, "Kinetic Evidence for a Monomer Activation Step in Actin Polymerization," Biochemistry-US **22**: 2193-2202 (1983).
12. J. Howard, *Mechanics of Motor Proteins and the Cytoskeleton* (Sinauer Associates, Sunderland, MA, 2001).
13. J. M. Neuhaus, M. Wanger, T. Keiser, A. Wegner, "Treadmilling of Actin," J Muscle Res Cell M **4**: 507-527 (1983).
14. T. Kreis, R. Vale, *Guidebook to the Cytoskeletal and Motor Proteins* (Oxford University Press, New York, NY, 1999).
15. Y. Le, D. Sept, A. E. Carlsson, "Energetics and dynamics of constrained actin filament bundling," Biophys

J **90**: 4295-4304 (2006).

16. A. D. Mehta, R. S. Rock, M. Rief, J. A. Spudich, M. S. Mooseker, R. E. Cheney, "Myosin V is a processive actin-based motor," Biophys J **78**: 272a-272a (2000).
17. M. Stewart, R. W. Kensler, "Arrangement of myosin heads in relaxed thick filaments from frog skeletal muscle," J Mol Biol **192**: 831-851 (1986).
18. G. H. Koenderink, Z. Dogic, F. Nakamura, P. M. Bendix, F. C. MacKintosh, J. H. Hartwig, T. P. Stossel, D. A. Weitz, "An active biopolymer network controlled by molecular motors," P Natl Acad Sci USA **106**: 15192-15197 (2009).
19. R. D. Kamm, T. Kim, W. Hwang, *Analysis of the Models for Cytoskeletal Rheology, in Tributes to Yuan-Cheng Fung on His 90th Birthday* (World Scientific Publishing Company, New Jersey, 2009).
20. R. L. Satcher, C. F. Dewey, "Theoretical estimates of mechanical properties of the endothelial cell cytoskeleton," Biophys J **71**: 109-118 (1996).
21. L. J. Gibson, M. F. Ashby, K. E. Easterling, "Structure and Mechanics of the Iris Leaf," J Mater Sci **23**: 3041-3048 (1988).
22. S. Kumar, I. Z. Maxwell, A. Heisterkamp, T. R. Polte, T. P. Lele, M. Salanga, E. Mazur, D. E. Ingber, "Viscoelastic retraction of single living stress fibers and its impact on cell shape, cytoskeletal organization, and extracellular matrix mechanics," Biophys J **90**: 3762-3773 (2006).
23. F. C. MacKintosh, J. Kas, P. A. Janmey, "Elasticity of Semiflexible Biopolymer Networks," Phys Rev Lett **75**: 4425-4428 (1995).
24. B. Fabry, J. J. Fredberg, "Remodeling of the airway smooth muscle cell: are we built of glass?," Resp Physiol Neurobi **137**: 109-124 (2003).
25. B. D. Hoffman, G. Massiera, K. M. Van Citters, J. C. Crocker, "The consensus mechanics of cultured mammalian cells," P Natl Acad Sci USA **103**: 10259-10264 (2006).
26. B. Wagner, R. Tharmann, I. Haase, M. Fischer, A. R. Bausch, "Cytoskeletal polymer networks: The molecular structure of cross-linkers determines macroscopic properties," P Natl Acad Sci USA **103**: 13974-13978 (2006).
27. M. L. Gardel, F. Nakamura, J. H. Hartwig, J. C. Crocker, T. P. Stossel, D. A. Weitz, "Prestressed F-actin networks cross-linked by hinged filamins replicate mechanical properties of cells," P Natl Acad Sci USA **103**: 1762-1767 (2006).
28. J. Liu, M. L. Gardel, K. Kroy, E. Frey, B. D. Hoffman, J. C. Crocker, A. R. Bausch, D. A. Weitz, "Microrheology probes length scale dependent rheology," Phys Rev Lett **96**: 118104 (2006).
29. J. Alcaraz, L. Buscemi, M. Grabulosa, X. Trepat, B. Fabry, R. Farre, D. Navajas, "Microrheology of human lung epithelial cells measured by atomic force microscopy," Biophys J **84**: 2071-2079 (2003).
30. L. Deng, X. Trepat, J. P. Butler, E. Millet, K. G. Morgan, D. A. Weitz, J. J. Fredberg, "Fast and slow

dynamics of the cytoskeleton," Nat Mater **5**: 636-640 (2006).

31. K. M. Van Citters, B. D. Hoffman, G. Massiera, J. C. Crocker, "The role of F-actin and myosin in epithelial cell rheology," Biophys J **91**: 3946-3956 (2006).
32. D. Stamenovic, B. Suki, B. Fabry, N. Wang, J. J. Fredberg, "Rheology of airway smooth muscle cells is associated with cytoskeletal contractile stress," J Appl Physiol **96**: 1600-1605 (2004).
33. M. L. Gardel, M. T. Valentine, J. C. Crocker, A. R. Bausch, D. A. Weitz, "Microrheology of entangled F-actin solutions," Phys Rev Lett **91**: 158302 (2003).
34. B. Schnurr, F. Gittes, F. C. MacKintosh, C. F. Schmidt, "Determining microscopic viscoelasticity in flexible and semiflexible polymer networks from thermal fluctuations," Macromolecules **30**: 7781-7792 (1997).
35. M. L. Gardel, J. H. Shin, F. C. MacKintosh, L. Mahadevan, P. Matsudaira, D. A. Weitz, "Elastic behavior of cross-linked and bundled actin networks," Science **304**: 1301-1305 (2004).
36. M. L. Gardel, J. H. Shin, F. C. MacKintosh, L. Mahadevan, P. A. Matsudaira, D. A. Weitz, "Scaling of F-actin network rheology to probe single filament elasticity and dynamics," Phys Rev Lett **93**: 188102 (2004).
37. G. H. Koenderink, M. Atakhorrami, F. C. MacKintosh, C. F. Schmidt, "High-frequency stress relaxation in semiflexible polymer solutions and networks," Phys Rev Lett **96**: 138307 (2006).
38. R. Tharmann, M. M. Claessens, A. R. Bausch, "Viscoelasticity of isotropically cross-linked actin networks," Phys Rev Lett **98**: 088103 (2007).
39. O. Chaudhuri, S. H. Parekh, D. A. Fletcher, "Reversible stress softening of actin networks," Nature **445**: 295-298 (2007).
40. Y. Tseng, B. W. Schafer, S. C. Almo, D. Wirtz, "Functional synergy of actin filament cross-linking proteins," J Biol Chem **277**: 25609-25616 (2002).
41. J. Y. Xu, Y. Tseng, D. Wirtz, "Strain hardening of actin filament networks. Regulation by the dynamic cross-linking protein alpha-actinin," J Biol Chem **275**: 35886-35892 (2000).
42. K. E. Kasza, A. C. Rowat, J. Liu, T. E. Angelini, C. P. Brangwynne, G. H. Koenderink, D. A. Weitz, "The cell as a material," Curr Opin Cell Biol **19**: 101-107 (2007).
43. J. H. Shin, M. L. Gardel, L. Mahadevan, P. Matsudaira, D. A. Weitz, "Relating microstructure to rheology of a bundled and cross-linked F-actin network in vitro," P Natl Acad Sci USA **101**: 9636-9641 (2004).
44. B. Fabry, G. N. Maksym, J. P. Butler, M. Glogauer, D. Navajas, J. J. Fredberg, "Scaling the microrheology of living cells," Phys Rev Lett **87**: 148102 (2001).
45. J. M. Ferrer, H. Lee, J. Chen, B. Pelz, F. Nakamura, R. D. Kamm, M. J. Lang, "Measuring molecular rupture forces between single actin filaments and actin-binding proteins," P Natl Acad Sci USA **105**: 9221-9226 (2008).

46. S. Furuike, T. Ito, M. Yamazaki, "Mechanical unfolding of single filamin A (ABP-280) molecules detected by atomic force microscopy," Febs Lett **498**: 72-75 (2001).

47. G. I. Bell, "Models for Specific Adhesion of Cells to Cells," Science **200**: 618-627 (1978).

48. D. Mizuno, C. Tardin, C. F. Schmidt, F. C. Mackintosh, "Nonequilibrium mechanics of active cytoskeletal networks," Science **315**: 370-373 (2007).

49. D. A. Head, A. J. Levine, F. C. MacKintosh, "Distinct regimes of elastic response and deformation modes of cross-linked cytoskeletal and semiflexible polymer networks," Phys Rev E **68**: 061907 (2003).

50. P. R. Onck, T. Koeman, T. van Dillen, E. van der Giessen, "Alternative explanation of stiffening in cross-linked semiflexible networks," Phys Rev Lett **95**: 178102 (2005).

51. E. M. Huisman, T. van Dillen, P. R. Onck, E. Van der Giessen, "Three-dimensional cross-linked F-actin networks: relation between network architecture and mechanical behavior," Phys Rev Lett **99**: 208103 (2007).

52. J. S. Palmer, M. C. Boyce, "Constitutive modeling of the stress-strain behavior of F-actin filament networks," Acta Biomater **4**: 597-612 (2008).

53. N. Ter-Oganessian, B. Quinn, D. A. Pink, A. Boulbitch, "Active microrheology of networks composed of semiflexible polymers: Computer simulation of magnetic tweezers," Phys Rev E **72**: 041510 (2005).

54. N. Ter-Oganessian, D. A. Pink, A. Boulbitch, "Active microrheology of networks composed of semiflexible polymers: theory and comparison with simulations," Phys Rev E **72**: 041511 (2005).

55. F. Gittes, F. C. MacKintosh, "Dynamic shear modulus of a semiflexible polymer network," Phys Rev E **58**: R1241-R1244 (1998).

56. H. Isambert, A. C. Maggs, "Dynamics and rheology of actin solutions," Macromolecules **29**: 1036-1040 (1996).

57. B. A. DiDonna, A. J. Levine, "Unfolding cross-linkers as rheology regulators in F-actin networks," Phys Rev E **75**: 041909 (2007).

58. D. C. Morse, "Viscoelasticity of tightly entangled solutions of semiflexible polymers," Phys Rev E **58**: R1237-R1240 (1998).

59. A. Prasad, Y. Hori, J. Kondev, "Elasticity of semiflexible polymers in two dimensions," Phys Rev E **72**: 041918 (2005).

60. B. D. Hoffman, G. Massiera, J. C. Crocker, "Fragility and mechanosensing in a thermalized cytoskeleton model with forced protein unfolding," Phys Rev E **76**: 051906 (2007).

61. B. A. DiDonna, A. J. Levine, "Filamin cross-linked semiflexible networks: fragility under strain," Phys Rev Lett **97**: 068104 (2006).

62. J. A. Astrom, P. B. Sunil Kumar, I. Vattulainen, M. Karttunen, "Strain hardening, avalanches, and strain softening in dense cross-linked actin networks," Phys Rev E **77**: 051913 (2008).

63. J. A. Astrom, P. B. S. Kumar, M. Karttunen, "Aster formation and rupture transition in semi-flexible fiber networks with mobile cross-linkers," Soft Matter **5**: 2869-2874 (2009).

64. F. Ziebert, I. S. Aranson, "Rheological and structural properties of dilute active filament solutions," Phys Rev E **77**: 011918 (2008).

65. T. Kim, W. Hwang, H. Lee, R. D. Kamm, "Computational Analysis of Viscoelastic Properties of Crosslinked Actin Networks," PLoS Comp Biol **5**: e1000439 (2009).

66. T. Kim, W. Hwang, R. D. Kamm, "Computational Analysis of a Cross-linked Actin-like Network," Exp Mech **49**: 91-104 (2009).

67. J. R. Kuhn, T. D. Pollard, "Real-time measurements of actin filament polymerization by total internal reflection fluorescence microscopy," Biophys J **88**: 1387-1402 (2005).

68. W. Humphrey, A. Dalke, K. Schulten, "VMD: visual molecular dynamics," J Mol Graph **14**: 33-38 (1996).

69. R. Clift, J. R. Grace, M. E. Weber, *Bubbles, drops, and particles* (Dover Publications, Mineola, 2005).

70. J. K. G. Dhont, W. J. Briels, "Inhomogeneous suspensions of rigid rods in flow," J Chem Phys **118**: 1466-1478 (2003).

71. J. Y. Xu, W. H. Schwarz, J. A. Kas, T. P. Stossel, P. A. Janmey, T. D. Pollard, "Mechanical properties of actin filament networks depend on preparation, polymerization conditions, and storage of actin monomers," Biophys J **74**: 2731-2740 (1998).

72. T. G. Mason, K. Ganesan, J. H. vanZantèn, D. Wirtz, S. C. Kuo, "Particle tracking microrheology of complex fluids," Phys Rev Lett **79**: 3282-3285 (1997).

73. F. Gittes, B. Schnurr, P. D. Olmsted, F. C. MacKintosh, C. F. Schmidt, "Microscopic viscoelasticity: Shear moduli of soft materials determined from thermal fluctuations," Phys Rev Lett **79**: 3286-3289 (1997).

74. S. Yamada, D. Wirtz, S. C. Kuo, "Mechanics of living cells measured by laser tracking microrheology," Biophys J **78**: 1736-1747 (2000).

75. A. Palmer, J. Y. Xu, D. Wirtz, "High-frequency viscoelasticity of crosslinked actin filament networks measured by diffusing wave spectroscopy," Rheologica Acta **37**: 97-106 (1998).

76. J. Y. Xu, A. Palmer, D. Wirtz, "Rheology and microrheology of semiflexible polymer solutions: Actin filament networks," Macromolecules **31**: 6486-6492 (1998).

77. Y. Luan, O. Lieleg, B. Wagner, A. R. Bausch, "Micro- and macrorheological properties of isotropically cross-linked actin networks," Biophys J **94**: 688-693 (2008).

78. S. Köhler, O. Lieleg, A. R. Bausch, "Rheological characterization of the bundling transition in F-actin solutions induced by methylcellulose," PLoS ONE **3**: e2736 (2008).

79. J. Liu, G. H. Koenderink, K. E. Kasza, F. C. MacKintosh, D. A. Weitz, "Visualizing the strain field in semiflexible polymer networks: Strain fluctuations and nonlinear rheology of F-actin gels," Phys Rev Lett **98**: 198304 (2007).

80. N. Wang, I. M. Tolic-Norrelykke, J. Chen, S. M. Mijailovich, J. P. Butler, J. J. Fredberg, D. Stamenovic, "Cell prestress. I. Stiffness and prestress are closely associated in adherent contractile cells," Am J Physiol Cell Physiol **282**: C606-C616 (2002).

81. D. Stamenovic, D. E. Ingber, "Models of cytoskeletal mechanics of adherent cells," Biomech Model Mechan **1**: 95-108 (2002).

82. D. H. Wachsstock, W. H. Schwarz, T. D. Pollard, "Cross-linker dynamics determine the mechanical properties of actin gels," Biophys J **66**: 801-809 (1994).

83. J. Y. Xu, D. Wirtz, T. D. Pollard, "Dynamic cross-linking by alpha-actinin determines the mechanical properties of actin filament networks," J Biol Chem **273**: 9570-9576 (1998).

84. M. L. Gardel, F. Nakamura, J. Hartwig, J. C. Crocker, T. P. Stossel, D. A. Weitz, "Stress-dependent elasticity of composite actin networks as a model for cell behavior," Phys Rev Lett **96**: 088102 (2006).

85. I. Schwaiger, A. Kardinal, M. Schleicher, A. A. Noegel, M. Rief, "A mechanical unfolding intermediate in an actin-crosslinking protein," Nat Struct Mol Biol **11**: 81-85 (2004).

86. G. Forgacs, R. A. Foty, Y. Shafrir, M. S. Steinberg, "Viscoelastic properties of living embryonic tissues: a quantitative study," Biophys J **74**: 2227-2234 (1998).

87. H. Lee, B. Pelz, J. M. Ferrer, T. Kim, M. J. Lang, R. D. Kamm, "Cytoskeletal Deformation at High Strains and the Role of Cross-link Unfolding or Unbinding," Cell Mol Bioeng **2**: 28-38 (2009).

88. F. J. Nedelec, T. Surrey, A. C. Maggs, S. Leibler, "Self-organization of microtubules and motors," Nature **389**: 305-308 (1997).

89. F. Backouche, L. Haviv, D. Groswasser, A. Bernheim-Groswasser, "Active gels: dynamics of patterning and self-organization," Phys Biol **3**: 264-273 (2006).

90. P. Hotulainen, P. Lappalainen, "Stress fibers are generated by two distinct actin assembly mechanisms in motile cells," J Cell Biol **173**: 383-394 (2006).

91. T. Surrey, F. Nedelec, S. Leibler, E. Karsenti, "Physical properties determining self-organization of motors and microtubules," Science **292**: 1167-1171 (2001).

92. C. Veigel, J. E. Molloy, S. Schmitz, J. Kendrick-Jones, "Load-dependent kinetics of force production by smooth muscle myosin measured with optical tweezers," Nat Cell Biol **5**: 980-986 (2003).

93. S. Uemura, H. Higuchi, A. O. Olivares, E. M. De La Cruz, S. Ishiwata, "Mechanochemical coupling of two substeps in a single myosin V motor," Nat Struct Mol Biol **11**: 877-83 (2004).

94. M. Kaya, H. Higuchi, "Nonlinear elasticity and an 8-nm working stroke of single myosin molecules in myofilaments," Science **329**: 686-689 (2010).

95. G. Piazzesi, M. Reconditi, M. Linari, L. Lucii, P. Bianco, E. Brunello, V. Decostre, A. Stewart, D. B. Gore, T. C. Irving, M. Irving, V. Lombardi, "Skeletal muscle performance determined by modulation of

number of myosin motors rather than motor force or stroke size," Cell **131**: 784-795 (2007).

96. B. Guo, W. H. Guilford, "Mechanics of actomyosin bonds in different nucleotide states are tuned to muscle contraction," Proc Natl Acad Sci U S A **103**: 9844-9 (2006).
97. T. P. Stossel, J. Condeelis, L. Cooley, J. H. Hartwig, A. Noegel, M. Schleicher, S. S. Shapiro, "Filamins as integrators of cell mechanics and signalling," Nat Rev Mol Cell Bio **2**: 138-145 (2001).
98. T. Hayashi, K. Maruyama, "Myosin aggregates as a requirement for contraction and a proposal to the mechanism of contraction of actomyosin systems," J Biochem **78**: 1031-8 (1975).
99. R. Kaunas, P. Nguyen, S. Usami, S. Chien, "Cooperative effects of Rho and mechanical stretch on stress fiber organization," P Natl Acad Sci USA **102**: 15895-15900 (2005).
100. P. Dalhaimer, D. E. Discher, T. C. Lubensky, "Crosslinked actin networks show liquid crystal elastomer behaviour, including soft-mode elasticity," Nat Phys **3**: 354-360 (2007).
101. D. Hostetter, S. Rice, S. Dean, D. Altman, P. M. McMahon, S. Sutton, A. Tripathy, J. A. Spudich, "Dictyostelium myosin bipolar thick filament formation: importance of charge and specific domains of the myosin rod," PLoS Biol **2**: e356 (2004).
102. J. C. Stachowiak, D. L. Richmond, T. H. Li, F. Brochard-Wyart, D. A. Fletcher, "Inkjet formation of unilamellar lipid vesicles for cell-like encapsulation," Lab Chip **9**: 2003-2009 (2009).
103. H. Y. Yuan, C. J. Huang, J. Li, G. Lykotrafitis, S. L. Zhang, "One-particle-thick, solvent-free, coarse-grained model for biological and biomimetic fluid membranes," Phys Rev E **82**: 011905 (2010).
104. P. J. Hoogerbrugge, J. M. V. A. Koelman, "Simulating Microscopic Hydrodynamic Phenomena with Dissipative Particle Dynamics," Europhys Lett **19**: 155-160 (1992).
105. P. L. Chandran, M. R. K. Mofrad, "Averaged implicit hydrodynamic model of semiflexible filaments," Phys Rev E **81**: 031920 (2010).